Une approche théorique et expérimentale pour l'étude des cellules solaires à colorants à base de pérovskites

Jun Su

PSL UNIVERSITÉ PARIS

THÈSE DE DOCTORAT
DE L'UNIVERSITÉ PSL

Préparée à Chimie ParisTech

Combined theoretical and experimental investigations of new perovskite compounds for solar cells applications
(Une approche théorique et expérimentale pour l'étude des cellules solaires à colorants à base de pérovskites)

Soutenue par
Jun SU
Le 14 Septembre 2020

Ecole doctorale n° 388
Chimie physique et chimie analytique de Paris Centre

Spécialité
Chimie Physique

Composition du jury :

Alexis, MARKOVITS Professeur, Sorbonne Université	*Président*
Pascal, BOULET Professeur, Université Aix-Marseille	*Rapporteur*
Tzonka, MINEVA Directrice de recherche, Institut Charles Gerhardt Montpellier	*Rapporteur*
Laurent, JOUBERT Professeur, Université de Rouen	*Examinateur*
Frédéric, LABAT Maître de conférences, Chimie ParisTech, Université PSL	*Examinateur*
Ilaria, CIOFINI Directrice de recherche, Chimie ParisTech, Université PSL	*Directeur de thèse*

Chimie Paris ParisTech | PSL

Acknowledgements

It has been three years since I arrived in Paris and I experienced an unforgettable time at ENSCP. I have seen many changes and growth of myself due to the study here, and there are many people and things to thank.

First of all, I am gratitude to my supervisors, Dr. Ilaria Ciofini, Dr. Frédéric Labat, and Dr. Thierry Pauporté for their patient guidance. Throughout the whole process of my PhD project, they taught me how to think and deal with the scientific problems, and cultivated my critical thinking and innovative consciousness. In particular, Dr. Frédéric Labat helped me to learn how to conduct theoretical calculations to do research step by step. Each time when I had a question, he can give timely help. I truly appreciate him. Furthermore, CTM group provide me with many opportunities for scientific communications, which expanded my horizons. These will be the cornerstones for me to achieve my life goals in the future. Sincerely, I thank my supervisors.

Second, I would like to express my appreciation to Prof. Carlo Adamo. He is full of wisdom and his achievements in the field of DFT are worth studying. I am also grateful to Dr. Alistar Ottochian and Dr. Aurélie Perrier for sharing research time together.

Third, I want to express the depth of my gratitude to Dr. Juan Sanz Garcia and Dr. Marco Campetella for their kindly help at the beginning time of my PhD. I also thank Dr. Francesco Muniz-Miranda, Bernardino Tirri, and Dario Vassetti, we not only shared the school time at ENSCP, but also shared memories of a trip to Alicante for a conference during which they helped me a lot. I am gratitude to Davide Luise and Tao Zhu for discussing the scientific problems together. I thank Dr. Elenonora Menicacci, Dr. Federica Maschietto, Dr. Laura Le Bras, Anna Perfetto, Carmela Morgillo, Gabrielly Miyazaki, Hanwei Li, Luca Brugnoli, Laure de Thieulloy, and Michele Turelli for sharing a happy time together in Paris. It is my honor to join CTM and I hope the life of all CTM members will be full of happiness.

I am grateful to my family who has always supported me. It is my family's selfless love, support, and encouragement that allowed me to pursue what I want. I give my deepest memory to my grandpa Mao-Ren Su. He was an optimistic old man who has given me a lot of care since I was a child.

Last but not the least, thanks for CSC for finance support.

Abstract

In this thesis, we aimed to contribute to a better understanding of the surfaces and interfaces involving perovskite compounds and governing the performances of PSCs, by using density-functional theory (DFT)-based computational protocols, with a comparison with experimental data, when available. More precisely, we first performed DFT calculations on TiO_2 anatase bulk and its (101) surface, and on the adsorption of four small organic ligands on the latter, aiming to select the best candidate for surface engineering of PSC. The benchmark calculations performed with different DFT models on bulk anatase indicated that hybrid functionals can both well reproduce the experimental lattice parameters with a small overestimation of the bandgap. For the adsorption calculations, a bidentate binding mode was found to be preferred for all ligands, in line with the vibrational frequencies investigation carried out which showed a general good agreement with available experimental data. From the properties computed, including density of states (DOS), dipole moments, and the work function obtained by experiments, it is derived that 4-Chlorobenzoate (CBA) and 4-Nitrobenzoate (NBA) are suitable candidates to improve the performance of PSC. We then simulated the heterointerface between the $CH_3NH_3PbI_3$ (MAPI) perovskite and TiO_2, in which the CBA ligand has been used to act as a bifunctional linker. Our calculation indicated that CBA can efficiently link the perovskite and the oxide moieties, ensuring stability of the interface through Ti-O and Pb-Cl interactions. Furthermore, CBA ligand can induce a favorable effect to improve band alignment and thus electron transfer from MAPI to TiO_2. Last, we reported preliminary calculations performed both on bulk α-$CH(NH_2)_2PbI_3$ (α-FAPI) as well as on two of its low-index surfaces, considering different terminations with both stoichiometric and non-stoichiometric slab models, which mainly revealed the structure-dependent properties. Overall, the obtained DFT results were in line with the experimental data. The DFT-based computational approach proposed in this thesis therefore allowed to better understand the basic mechanisms of PSCs, especially on the electron transfer from perovskite to TiO_2 (electron transfer layer). Moreover, general guidelines for the screening of molecules to be adopted as ligand to improve the performance of PSC could be drawn from the obtained results. The relationship between structure and perovskite properties could be established based on the DFT modeling carried out. Overall, the here proposed mixed theoretical/experimental approach could be extended to other semiconductor heterostructures in a wide variety of optoelectronic applications, where it could contribute to a better understanding of the working principles of these devices to improve their performances.

Résumé

Dans cette thèse, nous avons cherché à contribuer à une meilleure compréhension des surfaces, de l'interface et des composés de pérovskite régissant la performance des PSC, en utilisant des outils de modélisation basés sur la théorie de la fonctionnelle de la densité (DFT). Une comparaison avec des données expérimentales a été réalisée, lorsque ces dernières étaient disponibles. Plus précisément, nous avons tout d'abord effectué des calculs DFT sur TiO_2 anatase bulk, sa surface (101) ainsi que sur l'adsorption de quatre petits ligands organiques sur cette dernière, dans le but de sélectionner les candidats idéaux pour l'ingénierie de surfaces trouvées dans les PSC. Les modèles DFT hybrides reproduisent bien les paramètres expérimentaux du réseau de l'anatase bulk, tout en surestimant légèrement l'énergie de gap électronique. L'adsorption des ligands sur la surface anatase (101) a révélé qu'un mode de liaison de type bidentate était préféré pour tous les ligands envisagés, en accord avec les fréquences de vibration calculées qui étaient en bon accord général avec les données expérimentales disponibles. Sur la base des propriétés calculées dont la densité d'états (DOS), les moments dipolaires et la fonction de travail obtenue expérimentalement, le 4-chlorobenzoate (CBA) et le 4-nitrobenzoate (NBA) ont pu être suggérés comme candidats appropriés pour améliorer les performances des PSC. Ensuite, nous avons simulé l'hétéro-interface entre la pérovskite $CH_3NH_3PbI_3$ (MAPI) et TiO_2, dans laquelle le ligand CBA a été utilisé pour agir comme un ligand bifonctionnel. Nos calculs ont indiqué que le CBA peut lier efficacement la pérovskite et la surface de TiO_2, assurant la stabilité de l'interface par les interactions Ti-O et Pb-Cl. De plus, le ligand CBA peut induire un effet favorable pour améliorer l'alignement des bandes à l'interface et favoriser ainsi le transfert d'électrons de MAPI à TiO_2. Enfin, nous avons effectué des calculs préliminaires à la fois sur α-$CH(NH_2)_2PbI_3$ (α-FAPI) ainsi que sur deux de ses surfaces de faibles indices, en envisageant différentes terminaisons avec des modèles stoechiométriques ou non stoechiométriques, qui ont principalement révélé une dépendance des propriétés de ces systèmes en fonction de la structure des modèles. Ainsi, le protocole de calcul basé sur la DFT ici dévéloppé a permis de mieux comprendre le mécanisme de fonctionnement des PSC, en particulier le transfert d'électrons de la pérovskite à TiO_2 (couche de transfert d'électrons). En outre, des lignes directrices générales pour le criblage des molécules à adopter comme ligand pour améliorer les performances des PSC ont pu être élaborées à partir des résultats obtenus. L'approche mixte théorique/expérimentale ainsi proposée ici pourrait être étendue à d'autres hétérostructures semi-conductrices dans une grande variété d'applications optoélectroniques, contribuant alors à une meilleure compréhension du principe de fonctionnement de ces systèmes et à l'amélioration de leurs performances.

Table of Contents

Chapter 1: Research background

Section 1: Global energy trends and photovoltaic technology

Energy is the lifeline of human society and the requirement for energy is becoming even greater as civilization progresses, specifically in both quantity and quality, which means it is required to obtain or produce more energies in an environment-friendly and a sustainable way. According to the reports from BP company,[1] the world primary energy consumption was 13864.9 million tonnes oil equivalents. **Figure 1.1.1(a)** shows the contribution from various parts of the energy source, where we can see that the fossil energy sources oil, natural gas and coal take up most of the contributions (over 80%). Their use can however produce greenhouse gases (such as carbon dioxide, methane and nitrous oxide) and other harmful pollutants (ash, sulphur oxide etc.). For example, carbon dioxide emissions were of 33890.8 million tonnes in 2018 according to BP[1], which can lead to an increase of the atmospheric CO_2 concentration and a rise in global average temperature. But it should also be noted that low-carbon energy already owned a certain amount of market share. Among alternative technologies, renewable energies attract a lot of attention. In the *World Energy Outlook 2019* report released by International Energy Agency (IEA),[2] it is predicted that by 2040, low-carbon sources will provide more than half of total electricity generation and the solar photovoltaic (PV) will become the largest component of global installed capacity. This predication is based on the rapid development of PV. **Figure 1.1.1(b)** depicts the world renewable capacity growth between 2019 and 2024. The main case is the achievable goal under current technology and technological growth while the accelerated one is expected to achieve if the following issues can be resolved: i) policy and regulatory uncertainty; ii) high investment risks in developing countries; iii) system integration of wind and solar in some countries. It can be seen from this figure that solar PV is the single largest source of additional expansion potential, followed by onshore wind and hydropower. Therefore, solar PV is valuable for scientific research investment.

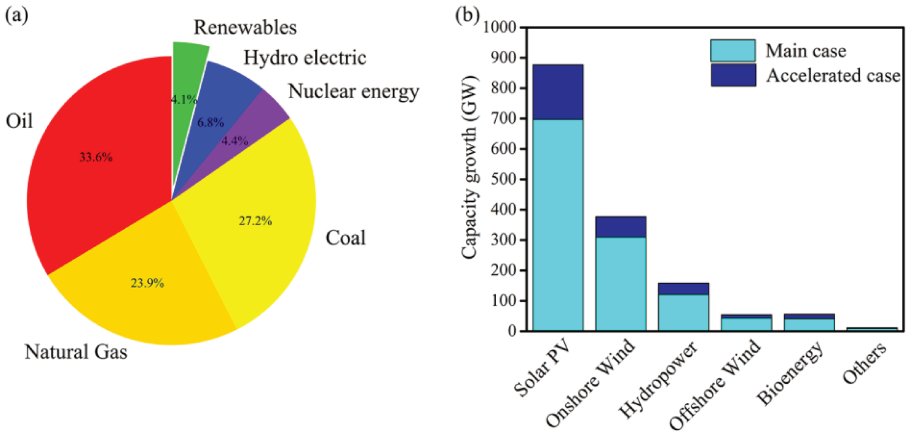

Figure 1.1.1: (a) World supply ratio of various energy technologies in 2018. Original data from BP company.[1] (b) Renewable capacity growth between 2019 and 2024 by technology. The main case is the achievable goal under current technology and technological growth while the accelerated one is expected to be achieved if some conditions are satisfied, as described in details in main text. Original data from from Ref. 2.

PV is the conversion of light into electricity using semiconductor materials that exhibit the photovoltaic effect. This is the creation of voltage and electric current upon exposure to light in an assembly of a p- and an n-type material in close contact, forming a p-n junction. By doping with the electron acceptors and donors, the p- and n-type materials can be fabricated. For instance, silicon can be made p-type (n-type) by doping with atoms that contain less (more) valence electrons than silicon, for example with aluminum (phosphor).

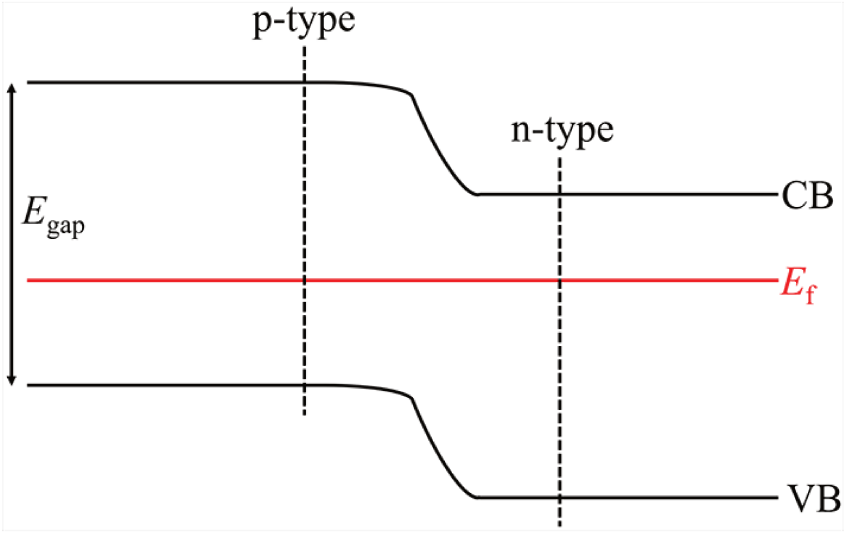

Figure 1.1.2: Band energy levels in the p-n junction. E_{gap} is the band gap. VB and CB correspond to valence band and conduction band, respectively. E_f is the fermi level.

Figure 1.1.2 defines two important semiconductor characteristics. E_{gap} is the minimal energy required to excite an electron from its bound state in VB into a free state in CB. E_F represents the chemical potential of the electrons. Usually, the E_F is in the middle of the band gap in an ideal intrinsic (non-doped) semiconductor. On the right part of the figure, E_F is closer to the bottom of CB, indicating that it is an n-type semiconductor. For p-type semiconductor, E_F is located closer to the top of VB, which corresponds to the situation depicted on the left part of the figure.

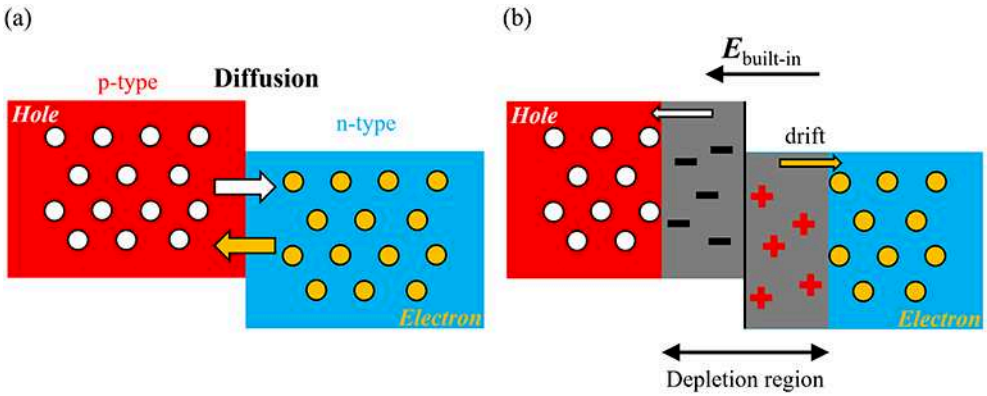

Figure 1.1.3: (a) Diffusion of free charge carriers between a p- and an n-type material. (b) Formation of a depletion region with a built-in electric field in a p-n junction.

In a p-n junction, the electrons and holes gather at the n- and p-type region, respectively. Therefore, as shown in **Figure 1.1.3(a)**, when the two semiconductors are put in contact, electrons from the n-type side diffuse freely to the p-type side. Similarly, holes diffuse from the p- to the n-type region. A diffusion current is thus obtained by such charge carriers' diffusion through the junction. As a result, there appears an area around the junction from where the free charge carriers are quickly swept out. **Figure 1.1.2(b)** depicts this region, called the depletion region. These displaced electrons and holes leave behind charged dopant atom sites fixed to the crystal lattice: positive ion cores are left behind in the n-type, and negative ion cores in the p-type material, forming an electric (built-in) field which works against the above described charge diffusion, and sweeps back the electrons and holes that are trying to cross the depletion region, causing a drift current. In equilibrium, the electron drift and diffusion current equal each other, which also applies to the hole drift and diffusion current, and the net current in the device is therefore zero. However, if a positive voltage is applied to the p-type, and

a negative voltage to the n-type region, an electric field opposing the built-in field of the depletion region is applied across the device, and the diffusion current is increased. This is called forward bias. In case of reverse bias, a voltage is applied across the device such that the built-in field increases, and the diffusion current decreases.

There are two major steps for a p-n semiconductor junction to convert sunlight energy into electricity. First, when irradiated by the sunlight, if the energy of the incident light is equal or superior to the band gap, electrons are promoted from the VB to the CB, leaving holes behind in the VB, and electron-hole pairs are thus created. The second step is the collection of charge carriers. The built-in field in the depletion region spatially separates the electrons and the holes and thus prevents recombination. Electrons and holes are driven towards different collectors, and if the terminals of the p- and n-type material are connected, the charge carriers can leave the device, and flow through the external circuit: a photogenerated current has been created.

Section 2: Solar cells

Characteristics

By taking advantages of the PV effect, one can collect the generated higher energy electron and control its movement toward an external circuit. Then, electron dissipates its energy in the external circuit and the sunlight energy to electric energy conversion process is achieved. The device used here is called solar cell. To evaluate a solar cell, its power conversion efficiency (PCE) is vital as a high efficiency leads to a better performance and wider range of practical applications. PCE refers to the portion of energy in the form of sunlight that can be converted via photovoltaics into electricity by the solar cell:

$$\mathrm{PCE} = \frac{E_{\mathrm{electricity}}}{E_{\mathrm{sunlight}}} \times 100\% \tag{1.2.1}$$

It is certain that PCE cannot be 100% because of reflectance, thermodynamic efficiency, charge carrier separation efficiency, charge carrier collection efficiency and conduction efficiency values. Theoretically, the maximum efficiency of a solar cell using a single p-n junction to collect power from the cell where the only loss mechanism is radiative

recombination in the solar cell is 33.7% for a solar cell with a bandgap of 1.34 eV.[3] The radiative recombination is the reverse process of photon absorption, where an electron drops back down to its equilibrium energy band and radiates a photon. This calculation was first done by William Shockley and Hans-Joachim Queisser at Shockley Semiconductor in 1961, giving a maximum efficiency of 30% at 1.1 eV, and this is the reason why this maximum efficiency is called Shockley–Queisser limit.[4] The difference here originates from the solar spectrum used. The calculation in 1961 used the 6000K blackbody spectrum while subsequent calculations have used measured global solar spectra (AM1.5G) and included a back-surface mirror. **Figure 1.2.1** gives the Shockley–Queisser limit for the efficiency of a solar cell, without concentration of solar radiation. It can be seen that a semiconductor with a bandgap around 1-1.5 eV is an ideal material for solar cell.

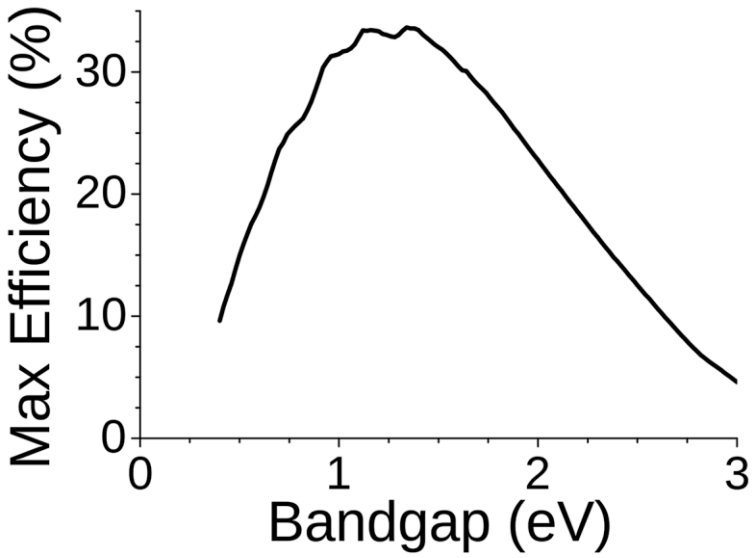

Figure 1.2.1: The Shockley–Queisser limit for the efficiency of a solar cell, assuming typical sunlight conditions (unconcentrated, AM 1.5 solar spectrum).

As the PCE is essential for solar cells, the factors that can affect a cell's PCE are thus of great research value. From the measurement of several parameters, including quantum efficiency, open-circuit voltage ratio (V_{OC}), and fill factor (FF), researchers can reveal the characteristics which influence the PCE of a solar cell.

Quantum efficiency is the percentage of photons that are converted to electric current when the cell is operated under short circuit conditions. When measuring the quantum efficiency, the effect of optical losses and recombination losses are both accounted for. The optical losses are the transmission and reflection of the light. The recombination losses are due to the failure collection of a carrier. As described above,

after the energy absorption from a photon, a solar cell can produce an electron-hole pair. One of the carriers may reach the p–n junction and contribute to the current produced by the solar cell; such a carrier is said to be collected. For other cases, the carriers' recombination occurs with no net contribution to cell current.

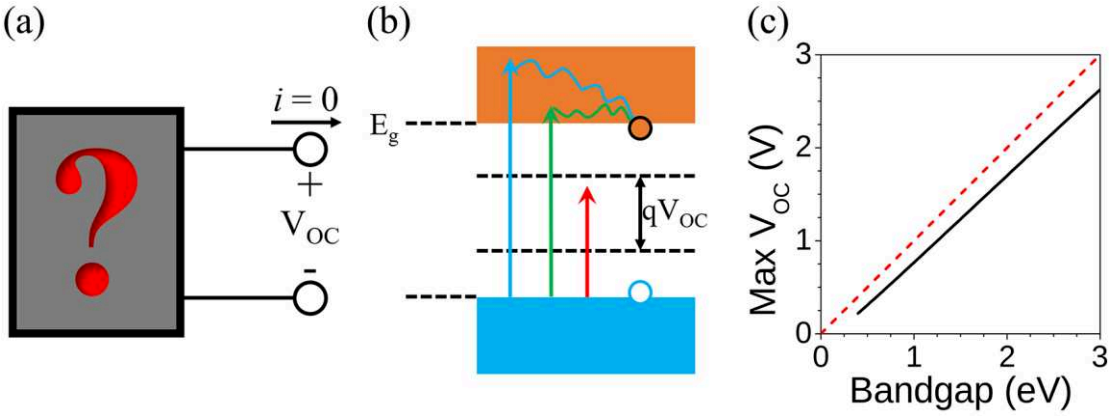

Figure 1.2.2: (a) Definition of open-circuit voltage (V_{OC}). (b) Electronic band structure with the seperation of the quasi-Fermi levels determining the V_{OC}. (c) Black curve: The highest possible open-circuit voltage of a solar cell in the Shockley-Queisser model under unconcentrated sunlight, as a function of the semiconductor bandgap. The red dotted line shows that this voltage is always smaller than the bandgap voltage.

V_{OC} refers to the difference of electrical potential between two terminals of a device when disconnected from any circuit, as depicted in **Figure 1.2.2(a)**. Even in an ideal case, however, the V_{OC} is always lower than the band gap energy. **Figure 1.2.2(b)** exemplifies related mechanisms. Photons with energies below the band gap E_g are not absorbed (red line), whereas photons with energies above the band gap are not fully converted to electrical energy because of thermalization of charge carriers (light blue line). Thus, the corresponding radiative carrier recombination represents a dark current that causes V_{OC} to be well below the band gap voltage E_g (**Figure 1.2.2(c)**).

FF is also a measure of quality of a solar cell and it can be calculated by the formula below:

$$FF = \frac{P_m}{V_{OC} \times I_{SC}} \tag{1.2.2}$$

where P_m is the power at the maximum power point, which is the point that maximizes V×I when increasing the resistive load on an irradiated cell continuously from zero (a short circuit) to a very high value (an open circuit), which can also be treated as the load for which the cell can deliver maximum electrical power at that level of irradiation; I_{SC} is the short circuit current. Typical fill factors range from 50% to 82%. The fill factor

for a normal silicon PV cell is 80% for instance.

When researchers investigate or develop solar cells, the characteristics mentioned above are key points to consider.

Classification

Different kinds of solar cells exist. Based on the cost-efficiency relationship, the single junction PV solar cells can be classified into three generations.[5] The first-generation solar cell has a high efficiency but also a relatively high production cost. The second-generation solar cell costs less during fabrication but cannot reach an efficiency as high as those of the first-generation. The third-generation solar cell is expected to obtain a high efficiency with low cost.

The first-generation solar cell is traditional silicon solar cell, which is made from the crystalline silicon materials. **Figure 1.2.3** depicts the working principle of silicon solar cell. Under sunlight irradiation, the photon energy is absorbed and the charge carriers are generated. Then, electrons and holes are transferred along n and p type silicon, respectively. Finally, the field current is obtained. For silicon solar cell, its PCE was over 26% in 2017[6] and it is actively commercialized. Although silicon solar cells have high PCE, this technology faces some problems in the actual industrial area, like: complicated production process, heavy weight, weak bending properties and performance degradation under high temperature. Therefore, it is very necessary to develop new generations of solar cells.

The second-generation solar cells are made from layers of semiconductor material with few micrometers thickness, referred to as thin film photovoltaics. It contains various types: cadmium telluride (CdTe), copper indium gallium selenide (CIGS), gallium arsenide (GaAs) thin film and silicon thin film. Compared with the first-generation solar cell, only CdTe can be competitive in terms of cost/watt. However, cadmium is highly toxic and tellurium supplies are limited. Therefore, second generation solar cells are not ideal solutions to replace silicon solar cell.

To improve cost, durability and viability aspects with easy and low-cost fabrication and construction, researchers paid much attention and developed various new types of solar cells, such as copper zinc tin sulfide (CZTS), organic/polymer, as well as solar cells sensitized with dyes, quantum dots and perovskites. These cells account for the majority of the third-generation solar cells.

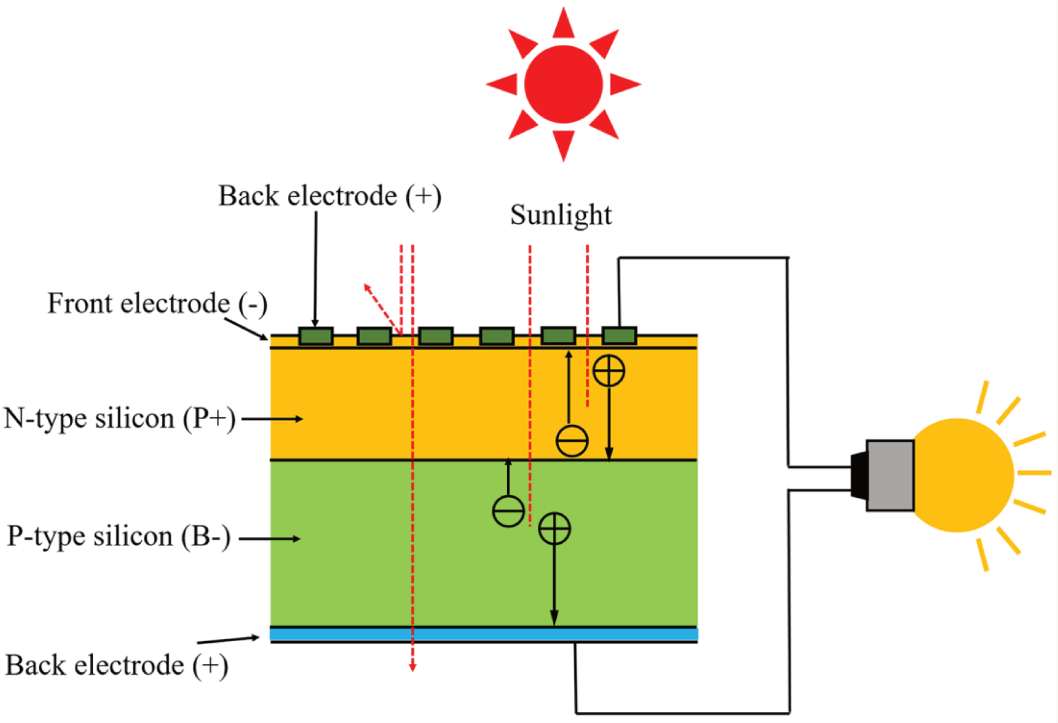

Figure 1.2.3: Scematic drawing of the main components of a silicon solar cell.

To compare various solar cells, **Table 1.2.1** is given. This table is referenced in table 1 of Sinke's paper,[7] with a rearrangement of the rows and a modification on cell efficiency by using the latest data from NREL.[8] From this table, it can be seen that despite various kinds of cell compounds, only perovskite solar cells have an efficiency comparable to silicon. This conclusion can be evidenced more intuitively from **Figure 1.2.4**. We can see that the PCE of perovskite increased rapidly in the last ten years, from 3.8% in 2009 to 25.2% in 2019. Therefore, perovskite solar cells have become a very hot issue in the scientific community, which is the topic of this work.

Table 1.2.1: Latest efficiency, technology strengths and key research opportunities for photovoltaic materials. Materials are grouped by generations.

Cell compounds	Latest efficiency*[1]	Status*[2]	Technology strengths and options	Selected research/technology opportunities
Monocrystalline Silicon	27.6%	iv	Earth-abundant material; >25-year track record	In combination with new metallization schemes; Shorten energy payback time (EPT), current ~2.5years; improve light management in thinner wafers; improve IBC and SHJ cell designs
Multicrystalline Silicon	22.8%	iv	Earth-abundant material; >25-year track record	Improve wafer quality (minimize or passivate defects) to reduce recombination losses
CdTe thin film	22.1%	iv	Flexible substrate; short EPT	Reduce combination losses; develop thinner cell designs using light management; Cd toxicity
CIGS thin film	23.4%	iv	Flexible substrates	Improve light management; increase efficiency for large band gaps (tandem cells); reduce recombination losses, solution processing
GaAs thin film	30.5%	ii	Very high efficiency; flexible modules	Improve light management; develop IBC geometry; develop thin-film multijunction cells by layer transfer; As toxicity
Thin film Silicon	14.0%	iii	Flexible modules	Reduce recombination losses; improve light management
Dye-sensitized	12.3%	iii	Tunable colors	Improve redox couple; reduce recombination losses; increase band gap; increase stability
Organic	17.4%	iii	Flexible modules, semitransparent modules	Improve light management; increase band gap; increase stability; reduce recombination losses
Quantum dots	16.6%	i	Solution processing; flexible modules	Reduce recombination losses; improve light management; avoid use of Pb
CZTS	12.6%	i	Flexible modules	Reduce recombination losses; improve light management
Perovskite	25.2%	i	Solution processing; flexible modules	Reduce recombination losses; improve cell stability; avoid use of Pb; increase efficiency for high-band gap materials (tandem cells); Si/perovskite tandems

*1: The efficiencies are based on the result from NREL.[8]

*2: Status stand for the technological development where i is the technologies shill under development in the laboratory research; ii is the technologies at the

manufacturing level; iii is emerging technologies deployer at smaller scale; iv is the mature technologies deployed at large scale.

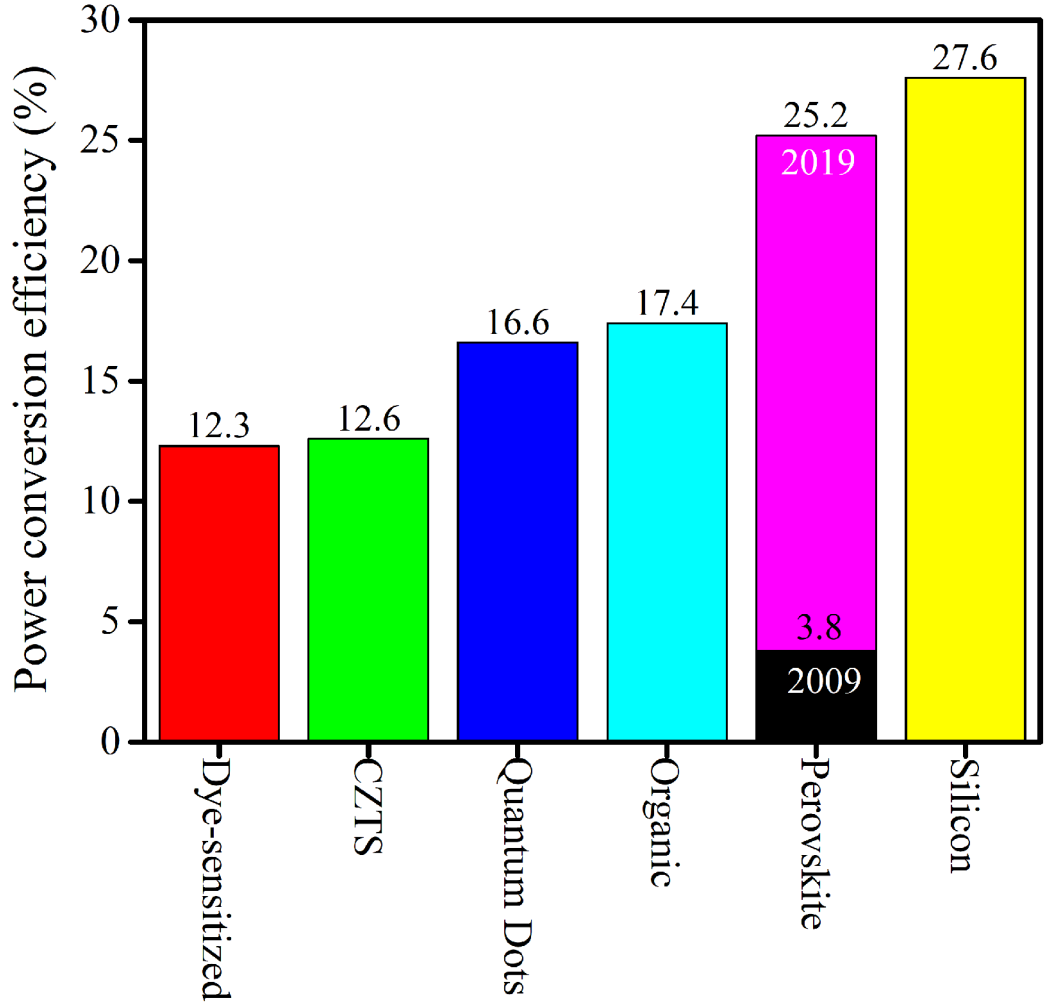

Figure 1.2.4: The PCE of third-generation solar cells. The PCE of silicon solar cell is also shown as a comparion. For perovkite, its efficency for 2009 and 2019 are both given in dark and fuchsia, respectively.

Section 3: Perovskite solar cells

A perovskite solar cell (PSC) consists of a perovskite layer as the light-harvesting active layer that is sandwiched between electron-transporting layer (ETL) and hole-transporting layer (HTL). The light goes through the ETL combined to a transparent conducting layer in front of the ETL. The cell is known as an n–i–p cell, where i stands for an intrinsic semiconductor. The opposite situation is a p–i–n cell, as shown in **Figure 1.3.1 (a)** and **(b)**. There are two basic structures for PSC: planar and mesoscopic. For planar structure PSC, two band configurations can exist: n-i-p planar and p-i-n planar,

as shown in **Figure 1.3.1 (c)** and **(d)**. Typically, mesoscopic structure only has an n–i–p configuration shown in **Figure 1.3.1 (e)**: compact ETL/mesoporous ETL/perovskite/HTL/Electrode.

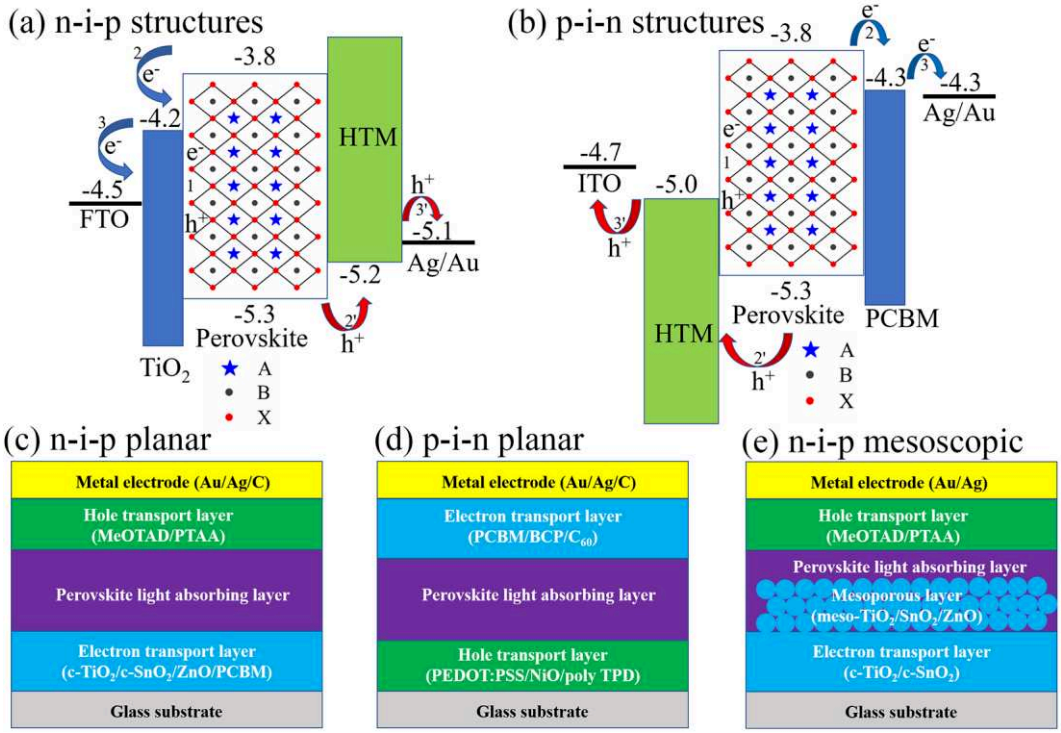

Figure 1.3.1: Energy band diagram of typical (a) n–i–p and (b) p–i–n structured PSCs; device structures of (c) n–i–p planar, (d) p–i–n planar, and (e) n–i–p mesoscopic PSCs.

For a PSC, when irradiated by sunlight, perovskite layers absorb energy from photons and generate electron-hole pairs. Due to the difference in exciton's binding energy of perovskite materials, these carriers either become free carriers or form excitons. Moreover, because of a lower carrier recombination probability and a higher carrier mobility, the diffusion distance and lifetime of the carriers are relatively longer. Then, these free carriers are collected by the electron transport layer (ETL) and hole transport layer (HTL), followed by the collection of electrons from ETL by the FTO and holes from HTL by an electrode, respectively. Finally, a photocurrent is generated by a circuit when connecting the FTO and a metal electrode. During this process, the loss of charge carriers is always happening due to many reasons, such as the reversible recombination of the electrons in the ETL with holes in the perovskite layer, the recombination of the electrons in the ETL with the holes in the HTL (the case where the perovskite layer is not dense), and the recombination of the electrons in the perovskite layer with the holes in the HTL. To improve the overall performance of the PSC, this kind of loss should be minimized. This is one of the research opportunities

for PSC and some other chances are gathered in **Table 1.2.1**. Among them, the improvement of cell stability and avoiding the use of Pb element are mainly for the PSC itself. To understand and to propose possible solutions toward the questions above, it is required to understand the construction parts of PSC. The subsequent sections will give a brief introduction to the perovskite compound and the composition materials for ETL.

Section 4: Perovskite compounds

The name of the perovskite originates from the mineral $CaTiO_3$, since the perovskite compound usually adopts the same ABX_3 three-dimensional (3-D) structural framework. As for the photovoltaic application, the perovskite used is organic-inorganic halide perovskite (OIHP). In this case, there is at least one organic ion at the "A", "B" or "X" site, as shown in **Figure 1.4.1**. Typically, the "A" cation is organic, for example the methylammonium and formamidinium "A" cations, while "B" is a metal and "X" is a halogen (Cl, Br, or I). The size limitation of space-filled ions determines whether certain "A", "B" or "X" ions can adopt a perovskite skeleton, which involves the corner-sharing network of BX_6 octahedron (i.e. BX_3), where "A" cations occupy 12-fold coordination holes within the structure and balance the charge of the BX_3 extended anion. The part below clarifies the concept of tolerance factor, which can determine the final structure of a perovskite compound. Followed by this part, different kinds of perovskite compounds will be introduced and especially the OIHP.

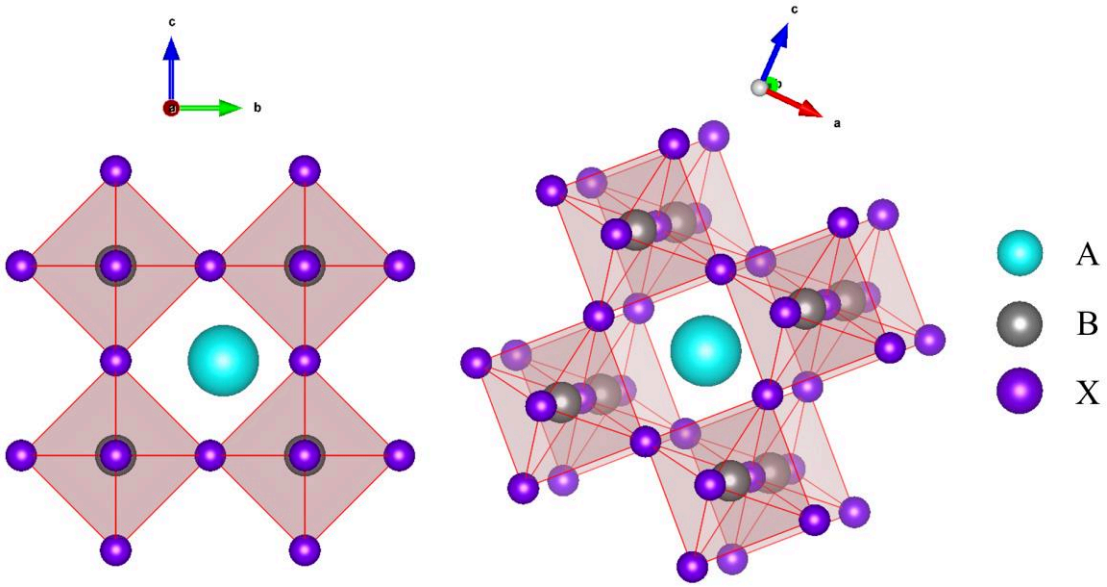

Figure 1.4.1: Schematic drawing of an organic-inorganic halide perovskite.

Tolerance factor

The tolerance factor (marked as α in this section) was introduced by V. M. Goldschmidt in 1926,[9] to evaluate ionic size mismatches that the perovskite structure will tolerate until a different structure-type is formed, according to:

$$\alpha = \frac{r_A + r_X}{\sqrt{2}(r_B + r_X)} \tag{1.4.1}$$

with r_i being the radii of ions in the perovskite ABX_3, and i = A, B and X, respectively. This equation is a semi-empirical relationship, which combines the idea of dense ionic packing with early estimates of ionic radii. The formula continues to be widely used as a guiding principle in the study of oxide perovskites.

However, for OIHP, its "A" site is occupied by organic and molecular ions. This is a challenge in determining tolerance factors because of the trouble in accurately estimating the ionic radii of "A" site. Many research works have been done toward this challenge. In 1949, Kapustinskii and Yatsimirskii proposed a set of thermochemical radii for molecular anions.[10] Due to hydrogen-bonding interactions, the molecular cations' bonds length varies in the case of OIHPs, which makes it difficult to define an ionic radius. By applying **Equation 1.4.1**, Mitzi obtained a maximum radius for the protonated amines of ~0.26 nm.[11] Based on this, Kieslich et al. extended the tolerance factor concept to the formate perovskites.[12] They assumed a rigid sphere model which is applicable to organic cations, by guessing free rotational freedom around the center of mass. Thus, a consistent set of effective ionic radii (r_{eff}) for different organic ions can be estimated, according to:

$$r_{eff} = r_{mass} + r_{ion} \tag{1.4.2}$$

with r_{mass} being the distance between the center of mass of the molecule and the atom with the largest distance to the center of mass, excluding hydrogen atoms; r_{ion} is the corresponding ionic radius of this atom. As for the molecular anions, we can therefore treat them as rigid cylinders, with effective radius r_{Xeff} and an effective height h_{Xeff}. In summary, **Equation 1.4.1** is then modified as:

$$\alpha = \frac{r_{eff} + r_{Xeff}}{\sqrt{2}(r_B + 0.5h_{Xeff})} \tag{1.4.3}$$

Table 1.4.1 gives the effective radii of molecular cations and anions. By using this method, the tolerance factor α can be obtained. For halide perovskites, generally 0.81

$< \alpha <$ 1.11. If α lies in the narrower range 0.89–1.0, the cubic structure of **Figure 1.4.1(a)** is likely, with lower α values giving less symmetric tetragonal or orthorhombic structures. Despite these constraints, transitions between such structures on heating are common for any given perovskite, with the high-temperature phase generally being cubic.

From the **Table 1.4.1**, it can be seen that there are many choices for OIHP. But it should be noted that most choices have been limited to methylammonium lead halide perovskite ($MAPbX_3$, X = I, Br or Cl, which is simplified as MAPX below) and formamidinium lead halide perovskite ($FAPbX_3$, X = I, Br or Cl, which is simplified as FAPX below). Furthermore, as the Pb element is toxic, lead-free halide perovskites are also under active investigation. However, this kind of PSC has a very low PCE so far, when compared to that of MAPX or FAPX.

Table 1.4.1: Effective radii of molecular cations and anions. Ionic radii of divalent metal ions were used according to reference.[13]

Cations		Effective radius r_{eff} (nm)
1	Ammouium $[NH_4]^+$	0.146
2	Hydroxylammonium $[H_3NOH]^+$	0.216
3	Methylammonium $[(CH_3)NH_3]^+$	0.217
4	Hydrazinium $[H_3N\text{-}NH_2]^+$	0.217
5	Azetidinium $[(CH_2)_3NH_2]^+$	0.250
6	Formamidinium $[NH_2(CH)NH_2]^+$	0.253
7	Imidazolium $[C_3N_2H_5]^+$	0.258
8	Dimethylammonium $[(CH_3)_2NH_2]^+$	0.272
9	Ethylammonium $[(C_2H_5)NH_3]^+$	0.274
10	Guanidinium $[C(NH_2)_3]^+$	0.278
11	Tetramethylammonium $[(CH_3)_4N]^+$	0.292
Anions		Effective radius (nm)
1	Iodide, I^-	r_{Xeff} = 0.220
2	Formate, $HCOO^-$	r_{Xeff} = 0.136
		h_{Xeff} = 0.136

MAPX

The semiconductor family MAPX were first synthesized during the 1970s[14] and met a renewal of interest during the 1990s,[15-18] because of the nonlinear optical phenomena that could result from the assumed large exciton binding energies. It was not until 2009 that MAPX regained research interest. By then, Miyasaka reported two

OIHPs, $CH_3NH_3PbBr_3$ (MAPBr) and $CH_3NH_3PbI_3$ (MAPI), suitable for efficiently sensitizing TiO_2 for visible-light conversion in photoelectrochemical cells. This discovery opened the way to PSC. Up to now, MAPX still has the best efficiencies in the semiconductor family for PSC application. Its "A" site, methylammonium molecule, is shown in **Figure 1.4.2**.

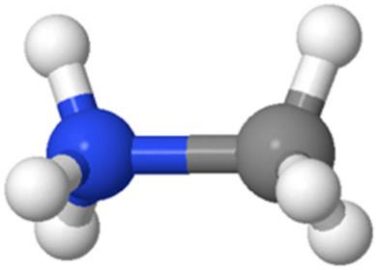

Figure 1.4.2: Ball and stick models of methylammonium cation. Blue, white and grey spheres represent N, H and C atoms, respectively.

The MAPX family has a temperature-dependent polymorphism, which is summarized in **Table 1.4.2**.

Table 1.4.2: Crystal structures of the MAPX family taken from Poglitsch et al.[19]

	Crystal system	Space group	Temperature/K
MAPCl	Cubic	Pm-3m	>179
	Tetragonal	P4/mmm	173-179
	Orthorhombic	$P222_1$	<173
MAPBr	Cubic	Pm-3m	>237
	Tetragonal	I4/mcm	155-237
	Tetragonal	P4/mmm	150-155
	Orthorhombic	$Pna2_1$	<144
MAPI	Cubic	Pm-3m	>327
	Tetragonal	I4/mcm	162-327
	Orthorhombic	$Pna2_1$	<162

As PSC are usually used at room temperature or even higher temperature environment, the cubic and tetragonal MAPI are preferred as they can be stable at working temperature. Up to now, there are many publications which focus on MAPX. These reports help understanding the PSC from various of aspects, with state-of-the-art efficiency. In particular, the high efficiency of PSCs may have various origins,

including long carrier-diffusion lengths that can ensure the collection of electrons,[20-21] low recombination rates that can improve the life of the carrier,[22-23] a sharp optical absorption edge that can enhance light absorption efficiency,[20, 24] and the possible existence of ferroelectric/polar domains.[25] Although these conclusions are mainly derived from experimental studies, a number of theoretical investigations have also been published and some of them are summarized below.

For example, the structural and electronic properties of bulk MAPX can be revealed by first principles calculations directly. Experimentally, the value of bandgap E_g decreases in the order Cl > Br > I, while the structure (cubic or tetragonal) only has a weak incidence on the bandgap. Only the MAPI material has a bandgap near the optimum for photovoltaic use which explains why this is the most used material in this family for this type of application (another reason is the temperature-dependent polymorphism, as mentioned above). The accurate calculation of E_g using DFT is not straightforward, Melissen et. al. reported large statistical dispersion in the values, as depicted in **Figure 1.4.3**.[26] It can be seen that spin-orbit coupling (SOC) has an important effect on E_g. In the MAPX family, where the chemical difference is only related to the halogen specie, the experimentally observed decrease in E_g in the Cl, Br, I series is well reproduced by the calculations with and without SOC, indicating that the main relativistic effects are associated with the lead atom. The bandgap reduction caused by SOC as computed using HSE is around 1.1 eV for all systems.[26] Furthermore, there is a noticeable reduction of the effective mass in some directions for which the minimum of the conduction shifts from the symmetric **k**-points compared to the calculation without SOC. Hence, in principle, when a quantitative description of the band gap is targeted, SOC should be taken into account. On the other hand, for structural parameters, SOC can be neglected to reduce calculation cost.

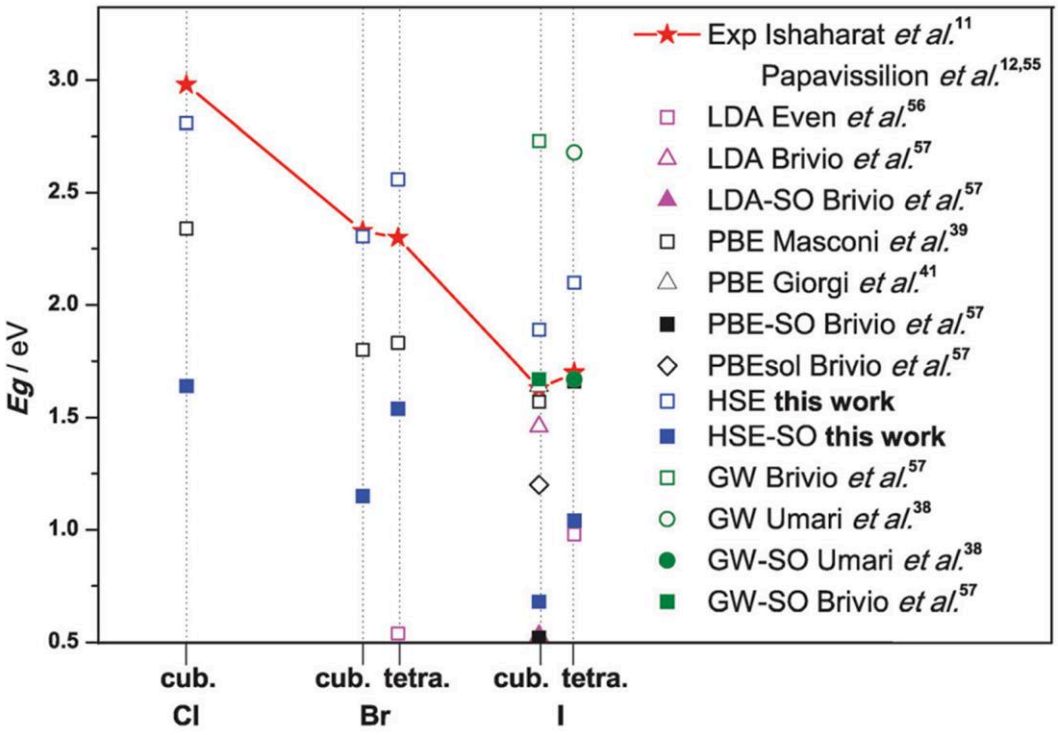

Figure 1.4.3: Experimental and theoretical direct bandgaps for MAPX (X = Cl, Br, I). ‘SO’’ refers to ‘‘spin–orbit coupling’’.[26]

Surface properties of the MAPX family should also be addressed. In PSC, the main reason that leads to the charge carriers’ loss is the back-charge transfer at the ETM/perovskite/HTM interface, where ETM means electron transfer material and HTM corresponds to hole transfer material, respectively. Thus, the understanding of surface properties of OIHP as building blocks of the interface is crucial, since it can influence the whole PSC performance. Tateyama et. al. investigated the termination dependence of tetragonal MAPI surfaces.[27] They put efforts on the structural stability and electronic states of the representative (110), (001), (100), and (101) surfaces of tetragonal MAPI, by using density functional theory (DFT) calculations. By examining various types of PbI_x polyhedron terminations, it was found that a vacant termination is more stable than flat termination on all of the surfaces, under thermodynamic equilibrium conditions of bulk MAPI. They also found that both terminations can coexist especially on the more probable (110) and (001) surfaces. The electronic structures of the stable vacant and PbI_2-rich flat terminations on these two surfaces largely maintain the characteristics of bulk MAPI without midgap states. Thus, these surfaces can contribute to the long carrier lifetime actually observed for the PSCs. Furthermore, the shallow surface states on the (110) and (001) flat terminations can be efficient intermediates of hole transfer. Consequently, the formation of the flat

terminations under the PbI_2-rich condition will be beneficial for the improvement of PSC performance. Liu et. al. investigated the effect of surface composition on electronic properties of MAPI, with special attention to (001) surface,[28] including both methylammonium iodide terminated (MAI-T) and PbI_2 terminated (PbI_2-T) surfaces. It was proposed that the MAI-T surface is thermodynamically more stable than the PbI_2-T one under equilibrium growth condition. The electronic properties of the two types of surfaces are also different. The band gap of PbI_2-T is smaller than that of MAI-T due to the surface Pb states. Band gaps of MAI-T decrease with increasing thickness, while band gaps of PbI_2-T are insensitive to the slab thickness. But both terminations are effective solar energy absorbers in the visible light spectrum from the computed optical absorption coefficients. Zhao et. al. identified the role of organic cations in hybrid halide perovskite MAPI surfaces.[29] It was demonstrated that the orientation of MA cations has profound consequences on the structural stability and electronic properties of the surfaces, in contrast to the bulk phases. The above studies on the surface of MAPI can help understand the characteristics of MAPI and propose a reference to the experiments by controlling the raw material consumption to obtain ideal surfaces. These calculations are thought to be of great benefit to the understanding of PSC and may help to improve the whole performances of PSC.

In addition to the specific cases discussed above, other aspects such as optical absorption, charge carriers diffusion, defects or degradation under humidity… are important, but won't be discussed in details here since this thesis mainly focuses on the structure, electronic, surface and interface properties of model interfaces found in PSC.

FAPX

Despite its advantages, MAPI has a poor near infrared absorption, implicating that it cannot collect solar energy at maximum efficiency. Furthermore, MAPI easily decomposes under humidity. To fix this problem, other perovskite candidates can be considered. Using formamidinium (model shown in **Figure 1.4.4**) to occupy the A site has been proved to be an ideal method as it has several advantages: (1) the larger organic FA cation can replace the MA cation and form a more symmetric crystal structure, (2) the smaller bandgap of FAPI allows for near infrared absorption, and (3) FAPI has an elevated decomposition temperature and thus potential to improve stability.[30-33] The synthesized FAPI usually has two structures, which are identified as α-FAPI and δ-FAPI.

The α-FAPI has black color and it has a direct bandgap around 1.45 eV, which is very suitable for PV application. However, in room temperature, it is easy to transform into δ-FAPI, which is yellow and has an indirect bandgap around 2.5 eV. This hexagonal structure cannot be used in PV. Due to the fast transition, in experiments, FA is always incorporated with other cations to stabilize it. However, from a theoretical point of view, pure α-FAPI can be investigated and serve as a reference to understand the effect of the stabilizing cations. To investigate pure α-FAPI, one must understand its structure first. From the high-resolution neutron powder diffraction data obtained by Weller et. al.,[34] the structure of α-FAPI is thought to be a cubic unit cell, with a = 6.36208Å. This is a highly symmetrical structure and this kind of structures are found to promote an enhanced SOC compared to octahedrally tilted tetragonal structures (typical of MAPI) because of the increased ionic character of Pb−I bonds, which enhances the Pb character in the materials conduction band thus amplifying the effect of SOC.[35] The structural properties of bulk FAPI can also be influenced by the orientations of organic cation FA, as proposed by S. Velumani et. al..[36]

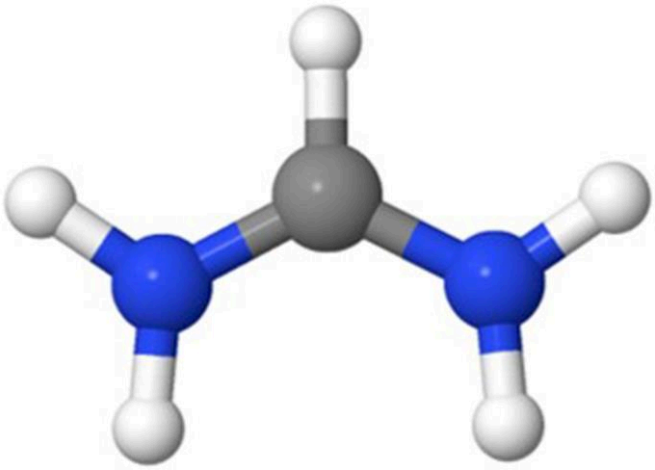

Figure 1.4.4: Ball and stick models of methylammonium cation. Blue, white and grey spheres represent N, H and C atoms, respectively.

Due to the fast transition of α-FAPI into δ-FAPI, a large amount of research was carried out using alkali cation (K, Cs, Rb, etc.) doped α-FAPI system.[37-38] Furthermore, there are also many research works focusing on the simulation on cation-doping FAPI system, as well as their surface properties. A. Suzuki et. al. investigated the electronic structures of alkali metals (Li, K, Na, and Rb)-incorporated FAPI.[39] They found that in this system, the conduction band were supplied with electrons from energy levels at 2s,

3s, 4s and 5s orbital of alkali metal to energy levels at 6p orbital of Pb atom in the perovskite crystal, which means that the alkali metals can influence the band structure. But this kind of doping would also bring some negative effects to the FAPI perovskite, as proved by R. Long et. al..[40] Using time domain density functional theory combined with nonadiabatic (NA) molecular dynamics, they showed that electron−hole recombination takes subnanoseconds in FAPI. Cs doping retards charge recombination by factors of 3.1 due to octahedral tilting. As for the surface slab model, Y. Guo et. al. did first principles study of Cs/Rb co-doped FAPI stability and degradation in the presence of water and oxygen, especially on the slab model.[41] Their results illustrate that the Cs terminated surface are energetically more favorable than others. The water and oxygen molecule tend to adsorb on the I-top site of the Cs-terminated surface and the Pb-top site of the PbI_2-terminated surface.

In this thesis, some preliminary calculation results on FAPI by using DFT will be given.

Section 5: ETL

Electron transport materials (ETMs) refer to materials that can accept negatively charged electron carriers and transport electron carriers. It can also help prevent the recombination of carriers at the interface, which is one of the decisive factors for improving the PCE of PSC. Generally, semiconductor materials with high electron affinity and ion potential (that is, n-type semiconductors) are used as electron transport materials. The common ETMs can be C_{60},[42-43] ZnO,[44-45] [6,6]-phenyl-C61-butyric acid methyl ester (PCBM),[46-47] indene-C60 bisadduct (ICBA),[48] and TiO_2.[49] Among them, titanium dioxide TiO_2 is one of the most widely used.

TiO_2 has three main crystal polymorphs, namely anatase, rutile, and brookite, as shown in **Figure 1.5.1**. In the natural environment, rutile should be the most stable phase. However, it has been reported that the stability of various TiO_2 phases is dependent on the particle size. When particle size is smaller than 11 nm, the most stable thermodynamic phase is anatase. If the size is larger than 35 nm, rutile is preferred. For the particle with size between 11 and 35 nm, brookite is the common phase.[50] Because of the contact between ETL and perovskite, higher specific surface area can improve the performances of PSC. For this reason, the surface properties of TiO_2, and especially those of anatase, are becoming a hot issue.

(a) Anatase (b) Rutile (c) Brookite

Figure 1.5.1: Structures of anatase, rutile, and brookite. Red and grey spheres correspond to O and Ti atoms, respectively.

The anatase crystal is formed by chains of distorted TiO_6 octahedra where each Ti atom is surrounded by 6 oxygen atoms. It has a tetragonal structure with space group $I4_1/amd$ as illustrated in both **Figure 1.5.1(a)** and **Figure 1.5.2**. In the anatase phase, the conventional unit cell contains four TiO_2 units, 12 atoms. O atom is coordinated to three Ti atoms, lying in the same plane in the unrelaxed structure, through one long bond (apical) and two short bonds (equatorial). F. Labat et. al. investigated the structural and electronic properties of TiO_2 crystals including both anatase and rutile by using DFT with different exchange-correlation functionals.[51] It was concluded that by using B3LYP, calculation results can give a good agreement with respect to the experiment concerning the electronic properties, while for structural description, PBE0 outperforms the other DFT models tested.

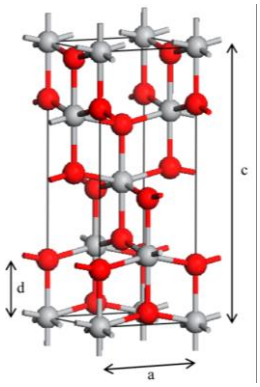

Figure 1.5.2: Tetragonal structure of anatase. It may be described using two cell edge parameters, *a* and *c*, and one internal parameter, *d* (the length of the Ti−O apical bond). The experimental values for a, c, and *d* are, respectively, equal to 3.782, 9.502, and 1.979 Å.[52] Grey and red balls represent, respectively, Ti and O atoms.

When choosing materials for ETL, the surface area is one of the most important factors to be considered.[53-55] Hence, analysis of the anatase surfaces is also crucial.

Following the usual preparation procedures, one can obtain anatase nanocrystals with the (101), (100), (001), (110), and (103) surfaces exposed.[56-57] Usually, the fabricated anatase exhibits the (101) surface, although other crystal faces may be observed. **Figure 1.5.3** shows the characteristic sawtooth profile of anatase (101) viewed along the [010] direction. It can be seen that the surface exposes both 5-fold (Ti_{5c}) and 6-fold (Ti_{6c}) coordinated Ti atoms, as well as 2-fold (O_{2c}) and 3-fold (O_{3c}) oxygens.

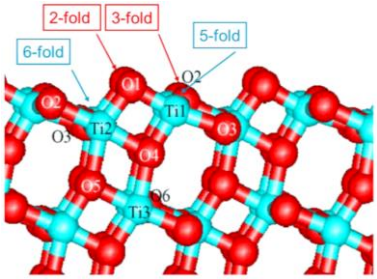

Figure 1.5.3: Side view of the anatase (101) surface.

The relative surface stability can be understood by comparing their surface energies, with a possible effect of the chosen computational approach on the relative stability obtained. For example, it was found that,[58] at local density approximations (LDA) and Hartree-Fock (HF) levels, the surface energies are: anatase (101) < rutile (110) < anatase (100) < rutile (100), rutile (001). However, using PBE, B3LYP, and PBE0, the two most stable surfaces are reversed. This conclusion has been confirmed in other investigations.[59-62]

The ETL/perovskite interface can be obtained by direct contact. However, by using suitable small molecules to do surface engineering on anatase, the properties of anatase can be improved toward a better performance as the role of ETL. The mechanism involved is the dipole moment introduced by small molecules. When a molecule is attached to the TiO_2 surface, it may induce a step in the local vacuum level due to the electric layer across this layer. The work function and the band edge of the TiO_2 surface are then changed.[63] This strategy may help to improve the performances of the cell device and it can be seen that surface engineering of the TiO_2 surface and in particular adsorption of well-chosen molecules on TiO_2 surfaces can be interesting for PSC application.

Because of its relevance to photocatalysis, water splitting, and other important applications,[64] the interaction of water with TiO_2 surfaces has been the subject of numerous investigations over the last decades.[65-71] When trying to understand the TiO_2-

based photocatalytic processes, molecular oxygen is found to play a key role in many such processes; in particular, O_2 adsorbed on TiO_2 surfaces is known to act as an electron scavenger and is often used to suppress electron−hole recombination, which increases the lifetime of the excited state and thus the yield of the photocatalytic reaction. Hence, this topic also gains a lot of research interests.[72-76] As for the surface engineering of TiO_2, the adsorbate is mainly carboxyl derivatives. P. R. McGill et. al. did DFT study of carboxylic acids modes of adsorption on rutile TiO_2(011) surfaces.[77] They concluded that formic acid appears to dissociatively adsorb in a bridging bidentate configuration on the surface. This means that the H^+ atom in the carboxylic group is dissociated and bound to surface via hydrogen bond while two O^{2-} atoms in group are connected to the Ti^{4+} atom on the surface. A. G. Thomas et. al. did adsorption studies of *p*-Aminobenzoic acid on the anatase TiO_2(101) surface by using synchrotron radiation photoelectron spectroscopy, near edge Xray absorption fine structure (NEXAFS) spectroscopy, and DFT calculations.[78] These works suggest that the molecule adsorbs in a bidentate binding mode on the surface, following deprotonation of the carboxyl group, in line with the adsorption of formic acid on rutile surface.

In summary, anatase can be treated as a possible suitable candidate as ETL in PSC, with an exposed (101) surface. Surface engineering by small molecule adsorption may help improve the performance of the cell.

Section 6: Challenges, goals and outline of the thesis

While the works devoted to the investigation of the isolated components of the ETL/perovskite interface are numerous as described in details in sections 4 and 5, much fewer have focused on the investigation of the full interface, probably due to its complexity and to the associated high computational cost. Furthermore, the current works devoted to the modeling of the full MAPI/TiO_2 interface mainly focus on their direct contact without introducing an additional ligand used as a linker.[79-81] However, from the experimental part, a lot of reports proved that self-assembly monolayers formed by the ligand can boost the performance of the whole cell device.[82-84] Related research from the theoretical calculation part is missing so far. This thesis aims to give some in-depth study in this area by using DFT. To achieve this, a series of investigations on bulk perovskite and surfaces, TiO_2 anatase surfaces and molecule adsorption, as well as the simulation on the interface will be done. In detail, they are listed as below:

i. Adsorption of molecule on TiO_2 surface.
ii. Preliminary DFT study on bulk and surface properties of perovskite compounds.
iii. Overall research on the interface between perovskite compound and TiO_2 slab. In particular, self-assembly monolayers are considered in the model.

Due to the complexity of some of the systems considered in this thesis, when possible, a comparison with available experimental data is made, in order to validate the models built and the computational strategies used. In particular, some of the experimental data presented in the following chapters has been obtained in close collaboration with the experimental group of Prof. Thierry Pauporté (IRCP, Chimie ParisTech, FR).

Outline of the thesis

Chapter II first describes the computational methods and theorical background used in this thesis. In **Chapter III**, adsorption of small organic molecules on TiO_2 surfaces, considered as possible linkers for the ETL/perovskite interface, was performed, with a direct comparison with available experimental data. **Chapter IV** proposes a combined theoretical/experimental investigation of the MAPI/ligand/TiO_2 interface, with a special emphasis on the role of ligand in PSC performances. In **Chapter V**, a preliminary computational study was done on the bulk and surface properties of FAPI.

References

1. https://www.bp.com/
2. https://www.iea.org/reports/renewables-2019
3. Rühle, S. Tabulated values of the Shockley–Queisser limit for single junction solar cells. *Sol. Energy* **2016**. *130*, 139 – 147.
4. Shockley, W. The Shockley-Queisser limit. *J. Appl. Phys.* **1961**. *32*, 510–519.
5. Mrinalini, M.; Islavath, N.; Prasanthkumar, S.; and Giribabu, L. Stipulating Low Production Cost Solar Cells All Set to Retail…! *Chem. Rec.* **2019**. *19*, 661–674.

6. Yoshikawa, K.; Kawasaki, H.; Yoshida, W.; Irie, T.; Konishi, K.; Nakano, K.; Uto, T.; Adachi, D.; Kanematsu, M.; Uzu, H.; et al. Silicon heterojunction solar cell with interdigitated back contacts for a photoconversion efficiency over 26%. *Nat. Energy* **2017**. *2*, 17032.
7. Polman, A.; Knight, M.; Garnett, E.C.; Ehrler, B.; and Sinke, W.C. Photovoltaic materials: Present efficiencies and future challenges. *Science* **2016**. *352*.
8. https://www.nrel.gov/pv/cell-efficiency.html
9. Goldschmidt, V.M. Die gesetze der krystallochemie. *Naturwissenschaften* **1926**. *14*, 477–485.
10. Kapustinskii, A. and Yatsimirskii, K. TERMOKHIMICHESKIE RADIUSY I ENERGETIKA TETRAEDRICHESKIKH I TREUGOLNYKH IONOV. *Zhurnal Obshchei Khimii* **1949**. *19*, 2191–2200.
11. Mitzi, D.B. Templating and structural engineering in organic–inorganic perovskites. *Dalton Trans.* **2001**, 1–12.
12. Kieslich, G.; Sun, S.; and Cheetham, A.K. Solid-state principles applied to organic–inorganic perovskites: new tricks for an old dog. *Chem. Sci.* **2014**. *5*, 4712–4715.
13. Glazer, A. Acta Crystallogr., Sect. B: Struct. Crystallogr. Cryst. Chem. **1972**.
14. Weber, D. Z Naturforsch B J. *Chem. Sci.* **1978**. *33*, 1443–1445.
15. Hirasawa, M.; Ishihara, T.; Goto, T.; Uchida, K.; and Miura, N. Magnetoabsorption of the lowest exciton in perovskite-type compound (CH_3NH_3)PbI_3. *Physica B Condens. Matter* **1994**. *201*, 427 – 430.
16. Papavassiliou, G. and Koutselas, I. Structural, optical and related properties of some natural three- and lower-dimensional semiconductor systems. *Synth. Met.* **1995**. *71*, 1713 – 1714.
17. Koutselas, I.B.; Ducasse, L.; and Papavassiliou, G.C. Electronic properties of threeand low-dimensional semiconducting materials with Pb halide and Sn halide units. *J. Phys. Condens. Matter* **1996**. *8*, 1217–1227.
18. Mashiyama, H.; Kurihara, Y.; and Azetsu, T. Disordered Cubic Perovskite Structure of $CH_3NH_3PbX_3$ (X= CI, Br, I). *JOURNAL-KOREAN PHYSICAL SOCIETY* **1998**. *32*, S156–S158.
19. Poglitsch, A. and Weber, D. Dynamic disorder in methylammoniumtrihalogenoplumbates (II) observed by millimeter-wave spectroscopy. *J. Chem. Phys.* **1987**. *87*, 6373–6378.

20. Xing, G.; Mathews, N.; Sun, S.; Lim, S.S.; Lam, Y.M.; Grätzel, M.; Mhaisalkar, S.; and Sum, T.C. Long-Range Balanced Electron- and Hole-Transport Lengths in Organic-Inorganic $CH_3NH_3PbI_3$. *Science* **2013**. *342*, 344–347.
21. Stranks, S.D.; Eperon, G.E.; Grancini, G.; Menelaou, C.; Alcocer, M.J.P.; Leijtens, T.; Herz, L.M.; Petrozza, A.; and Snaith, H.J. Electron-Hole Diffusion Lengths Exceeding 1 Micrometer in an Organometal Trihalide Perovskite Absorber. *Science* **2013**. *342*, 341–344.
22. Suarez, B.; Gonzalez-Pedro, V.; Ripolles, T.S.; Sanchez, R.S.; Otero, L.; and MoraSero, I. Recombination Study of Combined Halides (Cl, Br, I) Perovskite Solar Cells. *J. Phys. Chem. Lett.* **2014**. *5*, 1628–1635.
23. Gonzalez-Pedro, V.; Juarez-Perez, E.J.; Arsyad, W.S.; Barea, E.M.; FabregatSantiago, F.; Mora-Sero, I.; and Bisquert, J. General Working Principles of $CH_3NH_3PbX_3$ Perovskite Solar Cells. *Nano Lett.* **2014**. *14*, 888–893.
24. Du, M.H. Density Functional Calculations of Native Defects in $CH_3NH_3PbI_3$: Effects of Spin–Orbit Coupling and Self-Interaction Error. *J. Phys. Chem. Lett.* **2015**. *6*, 1461–1466.
25. Frost, J.M.; Butler, K.T.; Brivio, F.; Hendon, C.H.; van Schilfgaarde, M.; and Walsh, A. Atomistic Origins of High-Performance in Hybrid Halide Perovskite Solar Cells. *Nano Lett.* **2014**. *14*, 2584–2590.
26. Melissen, S.T.A.G.; Labat, F.; Sautet, P.; and Le Bahers, T. Electronic properties of $PbX_3CH_3NH_3$ (X = Cl, Br, I) compounds for photovoltaic and photocatalytic applications. *Phys. Chem. Chem. Phys.* **2015**. *17*, 2199–2209.
27. Haruyama, J.; Sodeyama, K.; Han, L.; and Tateyama, Y. Termination Dependence of Tetragonal $CH_3NH_3PbI_3$ Surfaces for Perovskite Solar Cells. *J. Phys. Chem. Lett.* **2014**. *5*, 2903–2909.
28. Geng, W.; Tong, C.J.; Tang, Z.K.; Yam, C.; Zhang, Y.N.; Lau, W.M.; and Liu, L.M. Effect of surface composition on electronic properties of methylammonium lead iodide perovskite. *J. Materiomics* **2015**. *1*, 213 – 220.
29. Teng, Q.; Shi, T.T.; Tian, R.Y.; Yang, X.B.; and Zhao, Y.J. Role of organic cations on hybrid halide perovskite $CH_3NH_3PbI_3$ surfaces. *J. Solid State Chem.* **2018**. *258*, 488 – 494.
30. Pellet, N.; Gao, P.; Gregori, G.; Yang, T.Y.; Nazeeruddin, M.K.; Maier, J.; and Grätzel, M. Mixed-Organic-Cation Perovskite Photovoltaics for Enhanced Solar-Light Harvesting. *Angew. Chem. Int. Ed.* **2014**. *53*, 3151–3157.

31. Pang, S.; Hu, H.; Zhang, J.; Lv, S.; Yu, Y.; Wei, F.; Qin, T.; Xu, H.; Liu, Z.; and Cui, G. NH2CHNH2PbI3: An Alternative Organolead Iodide Perovskite Sensitizer for Mesoscopic Solar Cells. *Chem. Mater.* **2014**. *26*, 1485–1491.
32. Koh, T.M.; Fu, K.; Fang, Y.; Chen, S.; Sum, T.C.; Mathews, N.; Mhaisalkar, S.G.; Boix, P.P.; and Baikie, T. Formamidinium-Containing Metal-Halide: An Alternative Material for Near-IR Absorption Perovskite Solar Cells. *J. Phys. Chem. C* **2014**. *118*, 16458–16462.
33. Eperon, G.E.; Stranks, S.D.; Menelaou, C.; Johnston, M.B.; Herz, L.M.; and Snaith, H.J. Formamidinium lead trihalide: a broadly tunable perovskite for efficient planar heterojunction solar cells. *Energy Environ. Sci.* **2014**. *7*, 982–988.
34. Weller, M.T.; Weber, O.J.; Frost, J.M.; and Walsh, A. Cubic Perovskite Structure of Black Formamidinium Lead Iodide, -[$HC(NH_2)_2$]PbI_3, at 298 K. *J. Phys. Chem. Lett.* **2015**. *6*, 3209–3212.
35. Amat, A.; Mosconi, E.; Ronca, E.; Quarti, C.; Umari, P.; Nazeeruddin, M.K.; Grätzel, M.; and De Angelis, F. Cation-Induced Band-Gap Tuning in Organohalide Perovskites: Interplay of Spin–Orbit Coupling and Octahedra Tilting. *Nano Letters* **2014**. *14*, 3608–3616.
36. Karthick, S.; Ríos-Ramírez, J.J.; and Velumani, S. 12 Possible Orientations of organic Formamidinium cation and its structural analysis by First Principles calculations using Van der Waals-Density functional Theory. In *2018 15th International Conference on Electrical Engineering, Computing Science and Automatic Control (CCE)*. 1–5.
37. Gao, X.X.; Luo, W.; Zhang, Y.; Hu, R.; Zhang, B.; Züttel, A.; Feng, Y.; and Nazeeruddin, M.K. Stable and High-Efficiency Methylammonium-Free Perovskite Solar Cells. *Adv. Mater.* **2020**. *32*, 1905502.
38. Lee, J.W.; Kim, D.H.; Kim, H.S.; Seo, S.W.; Cho, S.M.; and Park, N.G. Formamidinium and Cesium Hybridization for Photo- and Moisture-Stable Perovskite Solar Cell. *Adv. Energy Mater.* **2015**. *5*, 1501310.
39. Suzuki, A. and Oku, T. First-principles calculation study of electronic structures of alkali metals (Li, K, Na and Rb)-incorporated formamidinium lead halide perovskite compounds. *Appl. Surf. Sci.* **2019**. *483*, 912 – 921.
40. Qiao, L.; Sun, X.; and Long, R. Mixed Cs and FA Cations Slow Electron–Hole Recombination in $FAPbI_3$ Perovskites by Time-Domain Ab Initio Study: Lattice Contraction versus Octahedral Tilting. *J. Phys. Chem. Lett.* **2019**. *10*, 672–678.

41. Guo, Y.; Li, C.; Xue, Y.; Geng, C.; and Tian, D. First-principles study of Cs/Rb codoped FAPbI3 stability and degradation in the presence of water and oxygen. *Mater. Res. Express* **2018**. *5*, 026203.
42. Wojciechowski, K.; Leijtens, T.; Siprova, S.; Schlueter, C.; Hörantner, M.T.; Wang, J.T.W.; Li, C.Z.; Jen, A.K.Y.; Lee, T.L.; and Snaith, H.J. C60 as an Efficient n-Type Compact Layer in Perovskite Solar Cells. *J. Phys. Chem. Lett.* **2015**. *6*, 2399–2405.
43. Quarti, C.; De Angelis, F.; and Beljonne, D. Influence of Surface Termination on the Energy Level Alignment at the $CH_3NH_3PbI_3$ Perovskite/C60 Interface. *Chem. Mater.* **2017**. *29*, 958–968.
44. Son, D.Y.; Im, J.H.; Kim, H.S.; and Park, N.G. 11% Efficient Perovskite Solar Cell Based on ZnO Nanorods: An Effective Charge Collection System. *J. Phys. Chem. C* **2014**. *118*, 16567–16573.
45. Liu, D. and Kelly, T.L. Perovskite solar cells with a planar heterojunction structure prepared using room-temperature solution processing techniques. *Nature Photon.* **2014**. *8*, 133–138.
46. Xia, F.; Wu, Q.; Zhou, P.; Li, Y.; Chen, X.; Liu, Q.; Zhu, J.; Dai, S.; Lu, Y.; and Yang, S. Efficiency Enhancement of Inverted Structure Perovskite Solar Cells via Oleamide Doping of PCBM Electron Transport Layer. *ACS Appl. Mater. Inter.* **2015**. *7*, 13659–13665.
47. Chen, L.C.; Chen, J.C.; Chen, C.C.; and Wu, C.G. Fabrication and properties of high-efficiency perovskite/PCBM organic solar cells. *Nanoscale Res. Lett.* **2015**. *10*, 312.
48. Jeng, J.Y.; Chiang, Y.F.; Lee, M.H.; Peng, S.R.; Guo, T.F.; Chen, P.; and Wen, T.C. CH3NH3PbI3 Perovskite/Fullerene Planar-Heterojunction Hybrid Solar Cells. *Adv. Mater.* **2013**. *25*, 3727–3732.
49. Grancini, G. and Nazeeruddin, M.K. Dimensional tailoring of hybrid perovskites for photovoltaics. *Nat. Rev. Mater.* **2019**. *4*, 4–22.
50. Zhang, H. and Banfield, J.F. Understanding Polymorphic Phase Transformation Behavior during Growth of Nanocrystalline Aggregates: Insights from TiO_2. *J. Phys. Chem. B* **2000**. *104*, 3481–3487.
51. Labat, F.; Baranek, P.; Domain, C.; Minot, C.; and Adamo, C. Density functional theory analysis of the structural and electronic properties of TiO_2 rutile and anatase polytypes: Performances of different exchange-correlation functionals. *J. Chem. Phys.* **2007**. *126*, 154703.

52. Burdett, J.K.; Hughbanks, T.; Miller, G.J.; Richardson Jr, J.W.; and Smith, J.V. Structural-electronic relationships in inorganic solids: powder neutron diffraction studies of the rutile and anatase polymorphs of titanium dioxide at 15 and 295 K. *J. Am. Chem. Soc.* **1987**. *109*, 3639–3646.
53. Wu, W.Q.; Huang, F.; Chen, D.; Cheng, Y.B.; and Caruso, R.A. Thin Films of Dendritic Anatase Titania Nanowires Enable Effective Hole-Blocking and Efficient Light-Harvesting for High-Performance Mesoscopic Perovskite Solar Cells. *Adv. Func. Mater.* **2015**. *25*, 3264–3272.
54. Dar, M.I.; Ramos, F.J.; Xue, Z.; Liu, B.; Ahmad, S.; Shivashankar, S.A.; Nazeeruddin, M.K.; and Grätzel, M. Photoanode Based on (001)-Oriented Anatase Nanoplatelets for Organic–Inorganic Lead Iodide Perovskite Solar Cell. *Chem. Mater.* **2014**. *26*, 4675–4678.
55. Roy, P.; Kim, D.; Lee, K.; Spiecker, E.; and Schmuki, P. TiO_2 nanotubes and their application in dye-sensitized solar cells. *Nanoscale* **2010**. *2*, 45–59.
56. Gao, Y. and Elder, S. TEM study of TiO_2 nanocrystals with different particle size and shape. *Mater. Lett.* **2000**. *44*, 228 – 232.
57. Bourikas, K.; Kordulis, C.; and Lycourghiotis, A. Titanium Dioxide (Anatase and Rutile): Surface Chemistry, Liquid–Solid Interface Chemistry, and Scientific Synthesis of Supported Catalysts. *Chem. Rev.* **2014**. *114*, 9754–9823.
58. Labat, F.; Baranek, P.; and Adamo, C. Structural and Electronic Properties of Selected Rutile and Anatase TiO_2 Surfaces: An ab Initio Investigation. *J. Chem. Theory Comput.* **2008**. *4*, 341–352.
59. Marotta, G.; Reddy, M.A.; Singh, S.P.; Islam, A.; Han, L.; De Angelis, F.; Pastore, M.; and Chandrasekharam, M. Novel Carbazole-Phenothiazine Dyads for DyeSensitized Solar Cells: A Combined Experimental and Theoretical Study. *ACS Appl. Mater. Inter.* **2013**. *5*, 9635–9647.
60. Pastore, M. and De Angelis, F. Aggregation of Organic Dyes on TiO_2 in DyeSensitized Solar Cells Models: An ab Initio Investigation. *ACS Nano* **2010**. *4*, 556–562.
61. Zhang, L. and Cole, J.M. Adsorption Properties of p-Methyl Red Monomeric-toPentameric Dye Aggregates on Anatase (101) Titania Surfaces: First-Principles Calculations of Dye/TiO_2 Photoanode Interfaces for Dye-Sensitized Solar Cells. *ACS Appl. Mater. Inter.* **2014**. *6*, 15760–15766.

62. Agrawal, S.; Pastore, M.; Marotta, G.; Reddy, M.A.; Chandrasekharam, M.; and De Angelis, F. Optical Properties and Aggregation of Phenothiazine-Based DyeSensitizers for Solar Cells Applications: A Combined Experimental and Computational Investigation. *J. Phys. Chem. C* **2013**. *117*, 9613–9622.
63. Goh, C.; Scully, S.R.; and McGehee, M.D. Effects of molecular interface modification in hybrid organic-inorganic photovoltaic cells. *J. Appl. Phys.* **2007**. *101*, 114503.
64. De Angelis, F.; Di Valentin, C.; Fantacci, S.; Vittadini, A.; and Selloni, A. Theoretical Studies on Anatase and Less Common TiO_2 Phases: Bulk, Surfaces, and Nanomaterials. *Chem. Rev.* **2014**. *114*, 9708–9753.
65. Henderson, M.A. A surface science perspective on TiO_2 photocatalysis. *Surf. Sci. Rep.* **2011**. *66*, 185 – 297.
66. Sun, C.; Liu, L.M.; Selloni, A.; Lu, G.Q.M.; and Smith, S.C. Titania-water interactions: a review of theoretical studies. *J. Mater. Chem.* **2010**. *20*, 10319–10334.
67. Fujishima, A.; Zhang, X.; and Tryk, D.A. TiO_2 photocatalysis and related surface phenomena. *Surf. Sci. Rep.* **2008**. *63*, 515 – 582.
68. Vittadini, A.; Casarin, M.; and Selloni, A. Chemistry of and on TiO_2-anatase surfaces by DFT calculations: a partial review. *Theor. Chem. Acc.* **2007**. *117*, 663–671.
69. Diebold, U. The surface science of titanium dioxide. *Surf. Sci. Rep.* **2003**. *48*, 53 – 229.
70. Henderson, M.A. The interaction of water with solid surfaces: fundamental aspects revisited. *Surf. Sci. Rep.* **2002**. *46*, 1 – 308.
71. Linsebigler, A.L.; Lu, G.; and Yates Jr, J.T. Photocatalysis on TiO_2 surfaces: principles, mechanisms, and selected results. *Chem. Rev.* **1995**. *95*, 735–758.
72. Mattioli, G.; Filippone, F.; and Amore Bonapasta, A. Reaction Intermediates in the Photoreduction of Oxygen Molecules at the (101) TiO_2 (Anatase) Surface. *J. Am. Chem. Soc.* **2006**. *128*, 13772–13780.
73. Filippone, F.; Mattioli, G.; and Bonapasta, A.A. Reaction intermediates and pathways in the photoreduction of oxygen molecules at the (101) TiO_2 (anatase) surface. *Catal. Today* **2007**. *129*, 169 – 176.

74. Setvín, M.; Aschauer, U.; Scheiber, P.; Li, Y.F.; Hou, W.; Schmid, M.; Selloni, A.; and Diebold, U. Reaction of O_2 with Subsurface Oxygen Vacancies on TiO_2 Anatase (101). *Science* **2013**. *341*, 988–991.
75. Zhang, Z. and Yates, J.T. Effect of Adsorbed Donor and Acceptor Molecules on Electron Stimulated Desorption: $O_2/TiO_2(110)$. *J. Phys. Chem. Lett.* **2010**. *1*, 2185–2188.
76. Epling, W.S.; Peden, C.H.; Henderson, M.A.; and Diebold, U. Evidence for oxygen adatoms on $TiO_2(110)$ resulting from O_2 dissociation at vacancy sites. *Surf. Sci.* **1998**. *412-413*, 333 – 343.
77. McGill, P. and Idriss, H. DFT study of carboxylic acids modes of adsorption on rutile $TiO_2(011)$ surfaces. *Surf. Sci.* **2008**. *602*, 3688 – 3695.
78. Thomas, A.G.; Jackman, M.J.; Wagstaffe, M.; Radtke, H.; Syres, K.; Adell, J.; Lévy, A.; and Martsinovich, N. Adsorption Studies of p-Aminobenzoic Acid on the Anatase $TiO_2(101)$ Surface. *Langmuir* **2014**. *30*, 12306–12314.
79. Roiati, V.; Mosconi, E.; Listorti, A.; Colella, S.; Gigli, G.; and De Angelis, F. Stark Effect in Perovskite/TiO_2 Solar Cells: Evidence of Local Interfacial Order. *Nano Lett.* **2014**. *14*, 2168–2174.
80. De Angelis, F. Modeling Materials and Processes in Hybrid/Organic Photovoltaics: From Dye-Sensitized to Perovskite Solar Cells. *Acc. Chem. Res.* **2014**. *47*, 3349–3360.
81. Geng, W.; Tong, C.J.; Liu, J.; Zhu, W.; Lau, W.M.; and Liu, L.M. Structures and electronic properties of different $CH_3NH_3PbI_3/TiO_2$ interface: a first-principles study. *Sci. Rep.* **2016**. *6*, 20131.
82. Qiao, R. and Zuo, L. Self-assembly monolayers boosting organic-inorganic halide perovskite solar cell performance. *J. Mater. Res.* **2018**. *33*, 387.
83. Guo, X.; Zhang, B.; Lin, Z.; Ma, J.; Su, J.; Zhu, W.; Zhang, C.; Zhang, J.; Chang, J.; and Hao, Y. Interface engineering of TiO_2/perovskite interface via fullerene derivatives for high performance planar perovskite solar cells. *Org. Electron.* **2018**. *62*, 459 – 467.
84. Çisem Kırbıyık; Kara, K.; Kara, D.A.; Yiğit, M.Z.; İstanbullu, B.; Can, M.; Sariciftci, N.S.; Scharber, M.; and Kuş, M. Enhancing the c-TiO_2 based perovskite solar cell performance via modification by a serial of boronic acid derivative self-assembled monolayers. *Appl. Surf. Sci.* **2017**. *423*, 521 – 527.

Chapter II: Theoretical methods

Section 1: The Schrödinger equation

The time-independent and non-relativistic form of the Schrödinger equation (equation 2.1.1) for a system of *m* nuclei and *n* electrons is given by:

$$\hat{H}\Psi=E\Psi \tag{2.1.1}$$

where the $\hat{\boldsymbol{H}}$ operator is the Hamiltonian of the system, E is an eigenvalue and Ψ is an eigenvector of $\hat{\boldsymbol{H}}$, corresponding to the system's total energy and multi-electron wavefunction, respectively. The Hamiltonian can be described by the sum of the kinetic energy operators of the nuclei (T_N) and the electrons (T_e), the Coulomb attraction potential between the electrons and the nuclei with charge Z_I (V_{Ne}), the Coulomb repulsion potential between the electrons with charge e (V_{ee}), and the Coulomb repulsion potential between the nuclei (V_{NN}). The use of atomic units can describe them clearly. In atomic units, electron mass m_e, elementary charge e and $\hbar$ all equal to 1, while they equal to 9.109×10^{-31}kg, 1.602×10^{-19}C, and 1.054×10^{-34}J·s in SI units, respectively. $\hat{\boldsymbol{H}}$ operator is then expressed in the following form:

$$\begin{aligned}\hat{H} &= -\sum_{I=1}^{m}\frac{1}{2m_I}\nabla_i^2 - \sum_{i=1}^{n}\frac{1}{2}\nabla_i^2 - \sum_{I=1}^{m}\sum_{i=1}^{n}\frac{Z_I}{r_{Ii}} + \sum_{i=1}^{n-1}\sum_{j>i}^{n}\frac{1}{r_{ij}} + \sum_{I=1}^{m-1}\sum_{J>I}^{m}\frac{Z_I Z_J}{r_{IJ}} \\ &= T_N + T_e + V_{Ne} + V_{ee} + V_{NN}\end{aligned} \tag{2.1.2}$$

where m_I stands for the mass of nuclei I, Z_I for the nuclear charge of nuclei I, r for the inter-particule distances, and ∇^2 is the Laplacian operator in a 3-dimensional Cartesian coordinate system:

$$\nabla^2 = \frac{\partial^2}{\partial x^2} + \frac{\partial^2}{\partial y^2} + \frac{\partial^2}{\partial z^2} \tag{2.1.3}$$

By considering that the mass of electrons is negligible with respect to those of the nuclei, **Equation 2.1.2** can be simplified by applying the Born-Oppenheimer approximation. In detail, if the nuclei are fixed in space and do not move, their kinetic energy is zero and the potential energy due to nucleus-nucleus repulsion is merely a constant. Thus, the Hamiltonian can be decoupled, and written as the sum of an electronic ($\hat{H}_\mathrm{el}$) and a nuclear Hamiltonian ($\hat{H}_\mathrm{nuc}$):

$$\hat{H} = \hat{H}_{el} + \hat{H}_{nuc} \tag{2.1.4}$$

where $\hat{H}_{\text{nuc}}$ corresponds to the V_{NN} term, while $\hat{H}_{\text{el}}$ corresponds to the sum of T_{e}, V_{Ne}, and V_{ee}.

Solving equation 2.1.1 now reduces to the solution of the electronic part:

$$\hat{H}_{el}\Psi_{el} = E_{el}\Psi_{el} \tag{2.1.5}$$

The wavefunction can thus be treated as a product of an electronic (Ψ_{el}) and a nuclear wavefunction (Ψ_{nuc}):

$$\Psi = \Psi_{el} \times \Psi_{nuc} \tag{2.1.7}$$

with the total energy of the system written as the sum of the electronic energy (E_{el}) and the nuclear one (E_{nuc}) as:

$$E_{tot} = E_{el} + E_{nuc} = E_{el} + \sum_{I=1}^{m-1}\sum_{J>I}^{m}\frac{Z_I Z_J}{r_{IJ}} \tag{2.1.8}$$

In an n-electron system, Ψ is a function of 3n variables corresponding to the x, y and z coordinates of $\mathbf{r}_1$, $\mathbf{r}_2$, … $\mathbf{r}_{\text{n}}$, which makes calculations very demanding in terms of time and computational cost. Moreover, because of the bielectronic term in V_{ee}, the Schrödinger equation can be solved analytically only for a few simple cases like the H atom, the hydrogen molecular ion or hydrogenoid systems. Therefore, additional approximations are required and developed for multielectronic systems, such as the Hartree-Fock (HF) and density functional theory (DFT) methods which are introduced in the next sections. Since HF is the basis of most of the quantum methods, this is first briefly presented below.

Section 2: Hartree-Fock method

One of the simplest approximate theories for solving the Schrödinger equation is the HF theory. The essence of the HF approximation is to replace the complex many-electron problem by a one-electron problem in which the electron-electron interaction is treated in an average way. This means that each electron is subject to an average non-local potential arising from the other electrons. Although this approximation can lead to a poor description of the electronic structure, since the correlation among the electrons is neglected, the HF theory represents the starting point for most ab initio quantum chemistry methods.

If we assume that there is no interaction between the electrons of the system, the multielectronic Hamiltonian is decomposed into monoelectronic operators [$h_1(i)$],

resulting in the following equations:

$$h_1(i)\varphi_i(\vec{r}_i) = \varepsilon_i\varphi_i(\vec{r}_i) \tag{2.2.1}$$

where the ε_i eigenvalues correspond to the orbital energies, the sum of which makes up the electronic energy of the system:

$$E_{el} = \sum_i^n \varepsilon_i \tag{2.2.2}$$

$\boldsymbol{r}_i$ corresponds to the vectorial position of an electron *i* and the φ_i one-electron functions are called *orbitals*, the product of which would make up the multielectronic wavefunction. However, if the inter-electronic interactions are taken into account, ϕ_i spin-orbital functions are used instead of φ_i to express the multielectronic wavefunction of the system. With a non-relativistic Hamiltonian, the latter can be written as the product of a spin (σ_i) and a space function (ψ_i), within the orbital approximation:

$$\phi_i(\boldsymbol{r}_i, s_i) = \psi_i(\boldsymbol{r}_i)\sigma_i(s_i) \tag{2.2.3}$$

where the spin function is $\sigma_i = \pm 1/2$. The multielectronic wavefunction formed from the spinorbital functions (ϕ_i) must satisfy the Pauli principle by changing sign if two electrons are exchanged, which is possible if it is written in the form of the normalized Slater determinant:

$$\Phi_{Slater} = \frac{1}{\sqrt{n!}}\begin{vmatrix} \phi_1(\boldsymbol{r}_1) & \cdots & \phi_n(\boldsymbol{r}_1) \\ \vdots & \ddots & \vdots \\ \phi_1(\boldsymbol{r}_n) & \cdots & \phi_n(\boldsymbol{r}_n) \end{vmatrix} \tag{2.2.4}$$

with the condition that the space functions are orthonormal to each other:

$$\langle \psi_i | \psi_j \rangle = \delta_{ij} \tag{2.2.5}$$

with δ_{ij} corresponding to the Dirac delta.

The Hartree-Fock energy (E_0^{HF}) can be determined using the variational principle. For a given electronic configuration, the space functions ψ_i are varied until the Slater determinant (Φ_0) associated with the minimal energy E_0 that corresponds to the fundamental state of the system is obtained.

$$E_0^{HF} = \frac{\langle \Phi_0 | \hat{H}_N | \Phi_0 \rangle}{\langle \Phi_0 | \Phi_0 \rangle} \geq E_0 \tag{2.2.6}$$

In a closed-shell system, where electrons are organized in pairs on n/2 doubly occupied molecular orbitals, the HF energy is the sum of mono- (h_{ii}) and bielectronic

terms (J_{ij} and K_{ij}):

$$E_0^{HF} = 2\sum_i^{n/2} h_{ii} + \sum_i^{n/2}\sum_j^{n/2}(2J_{ij} - K_{ij}) \tag{2.2.7}$$

where J_{ij} and K_{ij} are known as the Coulomb and exchange integrals.

The interaction of a given electron *i* with the other electrons and the nuclei can be included in an approximative way: an effective field is defined, in which each electron *i* is affected by the potential generated by the nuclei and the average field of the other electrons. In this field, the molecular orbitals ϕ_i are eigenvectors of an effective operator known as the Fock operator *F*, and the energy levels of the system can be determined by solving the following monoelectronic Hartree-Fock equations:

$$F\phi_i = \varepsilon_i\phi_i \tag{2.2.8}$$

where ε_i are the eigenvalues of the Fock operator and correspond to the system's Koopmans ionization energies. The Fock operator is expressed as:

$$F(1) = h_1(1) + v_1^{HF} = h_1(1) + \sum_j^{n/2}[2J_j(1) - K_j(1)] \tag{2.2.9}$$

where v_1^{HF} is the above-mentioned effective potential felt by electron (1).

Molecular orbitals are developed on the basis of atom-centered functions χ_μ called atomic orbitals.[1] This approach is known as the *linear combination of atomic orbitals (LCAO)* approximation:

$$\phi_i = \sum_\mu^m c_{\mu i}\chi_u \tag{2.2.10}$$

with $c_{\mu i}$ coefficients. The size of the basis set χ_μ is chosen as a compromise between precision and computational cost. A complete (infinite) basis set would correspond to the so-called HF limit. The matrix representation of the Fock operator on the basis of the χ_μ atomic orbitals is expressed as:

$$\langle \chi_\mu | F | \chi_\nu \rangle = F_{\mu\nu} \tag{2.2.11}$$

And the *S* overlap matrix is written as:

$$\langle \chi_\mu | \chi_\nu \rangle = S_{\mu\nu} \tag{2.2.12}$$

Equation 2.2.6 can be reformulated as:

$$E_0^{HF} = \frac{\sum_\mu \sum_\nu c_\mu^* c_\nu F_{\mu\nu}}{\sum_\mu \sum_\nu c_\mu^* c_\nu S_{\mu\nu}} \geq E_0 \tag{2.2.13}$$

Instead of varying ψ_i space functions, we are now seeking the c_μ, c_ν coefficients that minimize the energy of the system which means we are looking for the cases when the partial derivative is equal to 0:

$$\frac{\partial E_0^{HF}}{\partial c_\mu} = 0 \tag{2.2.14}$$

After applying Equation 2.2.14, Equation 2.2.13 is transformed into the following secular matrix equation:

$$\sum_{\mu}^{m} F_{\mu\nu} c_{\nu i} = \varepsilon_i \sum_{\mu}^{m} S_{\mu\nu} c_{\nu i}$$
$$FC = SC\varepsilon \tag{2.2.15}$$

Equation 2.2.15 is solved in an iterative way, using the self-consistent field (SCF) procedure. In the first SCF cycle, the equation is solved using an initial guess of the coefficients c_μ, c_ν, and a new series of coefficients is thus obtained. The SCF procedure is continued until a predefined convergence threshold on energy between two SCF cycles is reached.

By using the HF approach, one can solve the Schrödinger equation approximately. However, a single determinant, like the one used in the HF formulation, is not able to express the exact wave function of most systems since the explicit electron-electron interaction is not taken into account: in the HF method the probability of finding an electron at some location around an atom is determined by the distance from the nucleus but not from the distance to the other electrons so that the correlation due to the coulomb interaction between the electrons (named Coulomb correlation) is completely neglected. Furthermore, although the use of Slater determinants allows to fully account for the correlation between electrons of parallel spin (electron exchange), the correlation between electrons of opposite spins is completely neglected so that the probability of finding two electrons having opposite spins in the same location of space is not equal to zero. The correlation energy (E_{corr}) is thus defined as the difference between the exact nonrelativistic energy of the system (E_{exact}) and the HF energy (E_{HF}) obtained in the limit of a complete basis set:

$$E_{corr} = E_0^{exact} - E_0^{HF} < 0 \tag{2.2.16}$$

Different methods, like the post-HF methods or the Density Functional Theory (DFT), have been proposed to introduce this correlation energy contribution. In the following section, we will briefly introduce the fundamentals of DFT, which have been

almost exclusively applied in this work.

Section 3: Density functional theory

Density functional theory (DFT) method was developed to solve the problem where correlation is ignored. DFT is a quantum mechanical method to investigate the electronic structure of many-body systems, such as molecules and condensed phases. DFT has gained popularity among chemists, physicists and material scientists due to the accurate results obtained at low computational cost. DFT has its conceptual roots in the Thomas-Fermi model from 1927,[2-3] which is based on the approximation that electrons are distributed uniformly in small ΔV volumes of a system, but the electron density (ρ) varies from one ΔV volume element to the other. The overall electron density depends only on the 3 spatial coordinates (x, y, z) expressed by the $\boldsymbol{r}$ vector, as shown in Equation:

$$\rho(\boldsymbol{r}) = \int_{\boldsymbol{r}_z} \ldots \int_{\boldsymbol{r}_n} \Psi(\boldsymbol{r}_1, \ldots \boldsymbol{r}_n)\Psi^*(\boldsymbol{r}_1, \ldots \boldsymbol{r}_n) d\boldsymbol{r}_z \ldots d\boldsymbol{r}_n \tag{2.3.1}$$

According to the Thomas-Fermi model, the kinetic energy of electrons, as well as the potentials describing classical electron-electron and electron-nucleus interactions can be expressed only in terms of electron density. ρ is a function of only 3 variables, while the many-body wavefunction of the Schrödinger equation depends on 3n variables in the Born-Oppenheimer approximation. In this way, the Thomas-Fermi model is an important step towards simplifying calculations. However, the model provides poor results for realistic systems, partly due to its basic assumption that electrons are uncorrelated. This drawback was improved by Dirac[4] who proposed to include an electron exchange energy term that also depended solely on $\rho(\boldsymbol{r})$.

Later, Hohenberg and Kohn established two theorems that made it possible for the electron density to become the basis of quantum mechanical calculations and the paved the way for modern DFT calculations in 1964.[5] The first Hohenberg-Kohn theorem states that every observable property of a system is a functional (a function from vector space into its underlying scalar field) of the electronic density. Most importantly, the total energy of the system can be written as:

$$E[\rho(\boldsymbol{r})] = T_e[\rho(\boldsymbol{r})] + V_{ee}[\rho(\boldsymbol{r})] + V_{Ne}[\rho(\boldsymbol{r})] \tag{2.3.2}$$

As all electrons share the same $v(\boldsymbol{r})$ external potential, the $V_{\mathrm{Ne}}[\rho(\boldsymbol{r})]$ term can be expressed as:

$$V_{Ne}[\rho(\boldsymbol{r})] = \int_{r_1}\ldots\int_{r_n} \Psi(\boldsymbol{r}_1,\ldots\boldsymbol{r}_n)\Psi^*(\boldsymbol{r}_1,\ldots\boldsymbol{r}_n)\sum_i v(\boldsymbol{r}_i)d\boldsymbol{r}_1\ldots d\boldsymbol{r}_n = \int \rho(\boldsymbol{r})v(\boldsymbol{r})d\boldsymbol{r} \tag{2.3.3}$$

Thus, the total energy functional can be written as:

$$E[\rho(\boldsymbol{r})] = F[\rho(\boldsymbol{r})] + \int \rho(\boldsymbol{r})v(\boldsymbol{r})d\boldsymbol{r} \tag{2.3.4}$$

where the $F[\rho(\boldsymbol{r})]$ term is the Hohenberg-Kohn functional defined as:

$$F[\rho(\boldsymbol{r})] = T_e[\rho(\boldsymbol{r})] + V_{ee}[\rho(\boldsymbol{r})] \tag{2.3.5}$$

The second Hohenberg-Kohn theorem states that in case $\rho_0(\boldsymbol{r})$ corresponds to the system's ground state electron density and E_0 to its ground state energy, then $E[\rho] > E_0$ for any $\rho \neq \rho_0$. Therefore, finding the ground state energy of a system in function of its electron density is a variational problem: one is seeking the electron density closest to ρ_0 in order to minimize the total energy. However, it is not possible to analytically solve this problem as we do not know the exact formula of $V_{ee}[\rho]$.

Kohn and Sham developed a method in 1965 to overcome the problem of expressing $V_{ee}[\rho]$.[6] It is introduced by considering a reference system with no electron-electron interactions which has the same ground-state electron density as the interacting system we want to study. Without electron-electron interactions, the properties of the reference system can be calculated by solving one-electron Schrödinger equations. Therefore, its wave function can be exactly represented by a Slater determinant defined in Equation 2.2.4. In the following, the single-electron wavefunctions known as *Kohn-Sham* (*KS*) orbitals [$\varphi_i(\boldsymbol{r}_i)$, with i = 1,…,n]] are used to express the electron density. The kinetic energy of the non-interacting reference system is written as:

$$T_s[\rho] = \sum_{i=1}^{N}\left\langle \varphi_i \left| -\frac{\hbar^2}{2m}\nabla^2\varphi_i \right\rangle \right. \tag{2.3.6}$$

In the next step, we suppose that the reference system is affected by an effective potential v_{eff}, which is expressed as the sum of terms describing nuclear-electron and electron-electron interactions:

$$v_{eff}(\boldsymbol{r}) = v(\boldsymbol{r}) + \frac{\delta J[\rho(\boldsymbol{r})]}{\delta\rho(\boldsymbol{r})} + \frac{\delta E_{XC}[\rho(\boldsymbol{r})]}{\delta\rho(\boldsymbol{r})} \tag{2.3.7}$$

where $v(\boldsymbol{r})$ corresponds to the nuclear-electron potential, $J[\rho]$ is the classical Coulombic term of the electron-electron interaction:

$$J[\rho] = \frac{1}{2}\int \frac{\rho(\boldsymbol{r})\rho(\boldsymbol{r}')}{|\boldsymbol{r}-\boldsymbol{r}'|}d\boldsymbol{r}d\boldsymbol{r}' \tag{2.3.8}$$

and $E_{xc}[\rho]$ is the exchange-correlation functional which accounts for the differences between the real interacting and the non-interacting reference system with $T[\rho]$ as the kinetic energy of the real interacting system:

$$\boldsymbol{E}_{XC}[\rho] = T[\rho] - T_S[\rho] + V_{ee}[\rho] - J[\rho] \tag{2.3.9}$$

Thus, the *Kohn-Sham Hamiltonian* ($\boldsymbol{H}_{\mathrm{KS}}$) can be obtained:

$$H_{\mathrm{KS}} = -\frac{\hbar^2}{2m}\nabla^2 + \nu_{eff}(\boldsymbol{r}) \tag{2.3.10}$$

The resulting Schrödinger equation is written in the following form:

$$[-\frac{\hbar^2}{2m}\nabla^2 + \nu_{eff}(\boldsymbol{r})]\varphi_i = \sum_{j=1}^{N}\varepsilon_{ij}\varphi_i \tag{2.3.11}$$

This is solved in a self-consistent iterative way, very similarly to HF calculations. First, an initial guess of $\rho(\boldsymbol{r})$ is used to calculate the corresponding $v_{\mathrm{eff}}(\boldsymbol{r})$ and solve the KS equations to obtain φ_{i}. A new electron density is then constructed from these KS orbitals, and the procedure is continued until convergence on orbital energies is reached. In this way, Kohn and Sham established an appealing method for the calculation of the ground-state properties of multi-electronic systems. However, as the exact form of the *exchange-correlation* functional is not known, it has to be approximated.

Exchange-correlation functionals

In the Kohn-Sham density functional theory, the exchange-correlation energy $E_{\mathrm{XC}} = E_{\mathrm{X}} + E_{\mathrm{C}}$ is a functional of the electron spin densities $\rho(\boldsymbol{r}) = n_{\uparrow}(\boldsymbol{r}) + n_{\downarrow}(\boldsymbol{r})$, which must be approximated. The most popular functionals have a form appropriate for slowly varying densities: the local spin density (LSD) approximation[7]:

$$E_{XC}^{LSD}[n_{\uparrow}, n_{\downarrow}] = \int d^3r n \in_{\mathrm{XC}}^{\mathrm{unif}}(n_{\uparrow}, n_{\downarrow}) \tag{2.3.12}$$

where $n = n_{\uparrow} + n_{\downarrow}$, and the generalized gradient approximation (GGA)[8]:

$$E_{XC}^{GGA}[n_{\uparrow}, n_{\downarrow}] = \int d^3r f(n_{\uparrow}, n_{\downarrow}, \nabla n_{\uparrow}, \nabla n_{\downarrow}) \tag{2.3.13}$$

In comparison with LSD, GGA tends to improve total energies,[8] atomization energies, [8-10] energy barriers and structural energy differences.[11-14] GGA can expand and soften bonds,[10] an effect that sometimes corrects[15] and sometimes overcorrects[16] the LSD prediction. Typically, GGA's favor density inhomogeneity more than LSD does.

Although GGA are known to provide accurate lattice parameters for a wide range

of semiconductors,[17] and computationally less expensive,[18] it is also known to severely underestimate band gaps.[19] This severe underestimation of band gaps originates from the spurious self-interaction error (SIE): Coulombic and approximated exchange self-interaction energies are not cancelled out. In purely Hartree-Fock calculations, this does not lead to a problem, since Coulomb self-interaction terms are perfectly cancelled out by the exact exchange self-interaction terms. It is thus a plausible idea to include a portion of HF exchange in the exchange term in order to decrease the SIE and reach a partial cancellation. This is called hybrid functionals, and this approximate method has been proved to reproduce experimental band gaps of semiconductor systems with very low error.[20] The as-constructed hybrid functionals are written in the general form of **Equation 2.3.14**:

$$E_{XC}^{hyb} = \alpha E_X^{HF} + (1-\alpha) E_X^{GGA} + E_C^{GGA} \tag{2.3.14}$$

In the above equation, the exchange-correlation functional is separated into an exchange (E_X) and a correlation term (E_C). The α coefficient is either a priori set to be a specific value based on theoretical arguments (for example the PBE0 functional[21]), or fitted to experimentally measured or calculated properties from a database (for example B3LYP,[22-23] O3LYP,[24] X3LYP[25] etc. functionals). Hybrids with a fixed α coefficient are called global hybrids, and the hybrids considered in this thesis (PBE0, with $\alpha = 25\%$[21]) belong to this group of functionals. Another notable group of hybrids is formed by the range-separated hybrid (RSH) functionals, which include different amount of exact HF exchange depending on the electron-electron distance. Some examples of RSH functionals include HSE06,[26] HISS[27-28] and LCwPBE[29].

It is noteworthy that although hybrid functionals can both be used with plane-wave (PW) and Gaussian-type orbtitals (GTO) basis sets, calculations remain so far computationally much more expensive with PW.[30] On the other hand, when combined with Gaussian-type basis sets, hybrids can efficiently be applied to periodic systems,[19,31] even to very large ones.[32] In this thesis, the systems we intended to study are semiconductor and corresponding heterostructures. Therefore, the use of Gaussian-type basis sets is suitable with hybrid functionals.

Long-Range Dispersion Correction

The introduction of GGA and the use of exchange-correlation functionals can provide reasonably accurate predictions for many properties of various molecules and

solids.[33-34] However, a general drawback of all common GGA and hybrid functionals, is that they cannot describe long-range electron correlations that are responsible for van der Waals (vdW, dispersive) forces.[35-37] The vdW interactions between atoms and molecules play an important role in many chemical systems. They are in detailed balance with electrostatic and exchange-repulsion interactions and, together, they control, for example, the structures of DNA and proteins, the packing of some crystals, the formation of aggregates, host–guest systems, or the orientation of some molecules on different surfaces or in molecular films. Therefore, long-range dispersion corrections should be in principle accounted for in such cases. A simple yet efficient proposal is that of Grimme et. al. who proposed semi-classical DFT-D corrections to take into account dispersion interactions, which can be applied even for large systems where dispersion forces are of general importance.[38-39] Such corrections have been formulated for both the energy and corresponding nuclear gradients.

With such an approach, the total energy is given by:

$$E_{DFT-D} = E_{KS-DFT} + E_{\text{disp}} \tag{2.3.15}$$

where $E_{KS\text{-}DFT}$ is the usual self-consistent Kohn-Sham energy and E_{disp} is an empirical dispersion correction given by:

$$E_{\text{disp}} = -s_6 \sum_{i=1}^{N_{at}-1} \sum_{j=i+1}^{N_{\text{at}}} \frac{C_6^{ij}}{R_{ij}^6} f_{\text{dmp}}(R_{ij}) \tag{2.3.16}$$

For the DFT-D2 approach. Here, N_{at} is the number of atoms in the system, C_6^{ij} denotes the dispersion coefficient for atom pair ij, s_6 is a global scaling factor that only depends on the functional used, and R_{ij} is an interatomic distance. In order to avoid near-singularities for small R, a damping function f_{dmp} must be used, which is given by:

$$f_{\text{dmp}}(R_{ij}) = \frac{1}{1+e^{-d(R_{ij}/R_r-1)}} \tag{2.3.17}$$

where R_{r} is the sum of atomic vdW radii.

The dispersion coefficients C_6^{ij} mentioned above are empirically derived. In the DFT-D3 approach, the dispersion coefficients are computed ab initio by time-dependent TD-DFT employing known recursion relations for the higher-multipole terms.[38] This approach has been proven to be asymptotically correct with all density functionals for finite systems (molecules) or nonmetallic infinite systems. It can provide a consistent description of all chemically relevant elements of the periodic system (nuclear charge Z=1–94), and similar or better accuracy for “light” molecules and a strongly improved

description of metallic and “heavier” systems. These advantages and properties make DFT-D3 approach a general tool for the computation of the dispersion energy in molecules and solids of any kind with DFT and related (low-cost) electronic structure methods for large systems.

Section 4: Modeling periodic systems

Bulk crystals

In this thesis, most of the systems considered correspond to systems with an infinite periodic structure, obtained by repeating in space an elementary structure called the unit cell. A crystal’s unit cell is the smallest unit of volume that contains all structural and symmetry information to build up the macroscopic structure of the crystal lattice in direct space by translation with the primitive lattice vectors ($\boldsymbol{a}_1$, $\boldsymbol{a}_2$, $\boldsymbol{a}_3$) or any of their linear combination:

$$\vec{R} = n_1\overrightarrow{a_1} + n_2\overrightarrow{a_2} + n_3\overrightarrow{a_3} \tag{2.4.1}$$

where n_1, n_2 and n_3 in N.

The corresponding reciprocal space is based on the ($\boldsymbol{b}_1$, $\boldsymbol{b}_2$, $\boldsymbol{b}_3$) basis vectors or their linear combinations:

$$\vec{R} = N_1\overrightarrow{a_1} + N_2\overrightarrow{a_2} + N_3\overrightarrow{a_3} \tag{2.4.2}$$

These ($\boldsymbol{b}_1$, $\boldsymbol{b}_2$, $\boldsymbol{b}_3$) vectors are determined from:

$$\mathbf{a}_i\mathbf{b}_j = 2\pi\delta_{ij} \tag{2.4.3}$$

where δ_{ij} stands for the Dirac delta. In consequence, the **b** vectors in reciprocal space are perpendicular to a plane defined by two **a** basis vectors with a different index in direct space. A unit cell in reciprocal space is defined by connecting a chosen origin point of the reciprocal space with its nearest neighbors. A plane perpendicular to these lines is drawn at their midpoint. The smallest volume enclosed by these planes is called the first Brillouin zone. By considering second, third etc. nearest neighbors, second, third etc. Brillouin zones of higher orders can also be defined. By applying the symmetry operations of the point group of the lattice, the irreducible Brillouin zone (IBZ) is obtained.

As crystals can ideally be built up by the periodic repetition of the unit cell, the electronic structure of crystals also shows a periodic pattern, which can be described by imposing periodic boundary conditions (PBCs) to the wavefunction of the system. According to Bloch's theorem, electron wave functions in these systems can be expressed solely on a basis of Bloch functions (BFs). BFs are periodic wavefunctions written in the following general form:

$$\phi_{\mathbf{k}}(\mathbf{r}) = e^{i\mathbf{k}\cdot\mathbf{r}} u_{\mathbf{k}}(\mathbf{r}) \tag{2.4.4}$$

In the above equation, **r** denotes the vector position in real space, **k** is the crystal wave vector in reciprocal space and u_kI is a periodic function that follows the periodicity of the crystal defined by I_i lattice vectors (i=1, 2, 3):

$$u_{\mathbf{k}}(\mathbf{r}) = u_{\mathbf{k}}(\mathbf{r} + \mathbf{a}_i) \tag{2.4.5}$$

It is thus assured that:

$$\phi_{\mathbf{k}}(\mathbf{r} + \mathbf{a}_i) = e^{i\mathbf{k}\cdot\mathbf{r}} \phi_{\mathbf{k}}(\mathbf{r}) \tag{2.4.6}$$

In consequence, the probability density is the same if the wave function is displaced by a lattice vector, since the imaginary terms in **Equation 2.4.6** cancel out. Therefore, the electronic structure mirrors the structural periodicity of the crystal:

$$\left|\phi_{\mathbf{k}}(\mathbf{r})\right|^2 = \left|\phi_{\mathbf{k}}(\mathbf{r} + \mathbf{a}_i)\right|^2 \tag{2.4.7}$$

In the LCAO approach for molecules, a finite number of molecular orbitals (MOs) are developed on a basis of atomic orbitals (AOs). In a crystal, an infinite number of unit cells (described individually by MOs) are repeated periodically in three dimensions, therefore the system should be described using an infinite number of MOs (and consequently AOs). These MOs are delocalized in a periodic pattern over the crystalline lattice, and are called crystalline orbitals (COs). The COs ($\Psi_{i,\mathbf{k}}$) are developed on a basis of Bloch functions ($\phi_{u,\mathbf{k}}$):

$$\Psi_{i,\mathbf{k}}(\mathbf{r}) = \sum_{\mu} c_{\mu,i}(\mathbf{k}) \phi_{\mu,\mathbf{k}}(\mathbf{r}) \tag{2.4.8}$$

with $c_{\mu,i}$ coefficients that are determined using the variational principle, by solving the matrix equations introduced in **Equation 2.2.15**, on the basis of Bloch functions:

$$H^K C^K = S^K C^K E^K \tag{2.4.9}$$

where H^K is the matrix representation of the Hamiltonian on the basis of Bloch functions, C^K is the matrix containing the coefficients of Equation 2.6.6, S^K is the overlap matrix, E^K is the diagonal matrix containing the eigenvalues ε^K. Because of the PBCs, these calculations are limited to the first BZ of the system. However, with an infinite N number of unit cells in the lattice, the number of **k** points is also infinite. In consequence, matrix equation **Equation 2.4.9** need to be solved for an infinite number of **k** points in the first BZ in principle, which would be impossible. However, in practice, the calculated properties actually converge with the number of the used **k** points. In consequence, a limited number of **k** points is sufficient for the sampling of the first BZ.

Two types of basis functions are commonly used to represent Bloch functions in DFT calculations of periodic systems: localized and plane wave basis sets. In our calculation, the CRYSTAL program was mainly used, where the localized basis sets are considered. Some details regarding the use of localized basis sets with periodic boundary conditions are given in Section 6.

Crystal surfaces

In nature, crystals are not infinite but finite 3-D objects terminated by surfaces. Many phenomena and processes occur at the interface between a condensed phase and the environment. Modeling surfaces is then of great theoretical and practical interest. A surface can be created by cutting a crystal, which we simulate as an infinite object, through a crystalline plane. Two semi-infinite crystals are then generated containing an infinite number of atoms in the direction orthogonal to the surface, where periodicity is lost. We then need further approximations to be able to treat this problem. We will focus here on the two-dimensional (2-D) slab model. The slab model consists of a film formed by a few atomic layers parallel to the (*hkl*) crystalline plane of interest. The film, of finite thickness, is limited by two surface planes, possibly related by symmetry. For sufficiently thick slabs, this kind of model can provide a faithful description of the ideal surface.

The (*hkl*) indices are the Miller indices. The indices of any given plane can be worked out by considering the intersection of the plane with the crystallographic unit cell vectors **a**, **b**, and **c**. If *x*, *y* and *z* are the fractional coordinates of the intersections of the plane with **a**, **b**, and **c**, Miller indices are the smallest integers in the same ratio as (1/x,1/y,1/z). Here are some examples for cubic lattices:

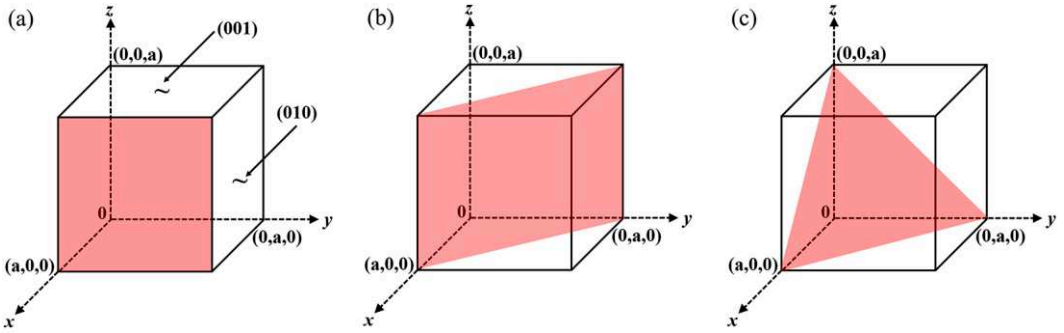

Figure 2.4.1: Miller indices of some important low-indices planes in a cubic crystal. (a) (100); (b) (110) and (c) (111).

After optimizing the structure of slabs of different thicknesses, the adequacy of the model is checked by considering the convergence of a number of properties, including atomic relaxations, surface formation energies and band gaps with respect to slab thickness.

When studying processes of adsorption or defect formation, the unit cell of the surface may be too small to avoid spurious interactions between the defect or the adsorbate and its periodic images. In these cases, the supercell approach can be applied. For bulk systems, creating a supercell corresponds to multiplying the unit cell in the three periodic directions. For surfaces, the multiplication of the unit cell is operated in the two periodic directions. The dimensions of the supercell should be such as to ensure that the spurious interactions become negligible.

Furthermore, when considering an interface system like the boundary between two spatial regions occupied by different matter, there would be lattice mismatch between two surface unit cells or supercells. In such cases, there is a certain difference in the orientation of the two parts forming the interface. When the equilibrium is reached, atoms at the interface form a distinct transitional zone. The construction of a model interface can generally be done by modifying the lattice of the less symmetric surface slab to match the more symmetric one.

Section 5: CRYSTAL code and localized basis sets

All calculations in this thesis were performed with the *CRYSTAL*14[40] and *CRYSTAL*17[41] codes, which use a linear combination of atomic orbitals (LCAO) approach to self-consistently solve both Hartree-Fock and Kohn-Sham equations. *CRYSTAL* calculations are based on crystalline orbitals (COs, $\mathbf{\Psi}_{i,\mathbf{k}}$) that are defined as

linear combinations of Bloch functions (BFs, $\phi_{\mu,\mathbf{k}}$), as described by **Equation 2.4.8**. BFs are described in terms of localized (atom-centered) atomic orbitals (AOs, $\varphi_{\mu}(\mathbf{r})$) on a set of lattice vectors **a**:

$$\phi_{\mu,\mathbf{k}}(\mathbf{r}) = \sum_{a} \varphi_{\mu}(\mathbf{r} - \mathbf{A}_{\mu} - \mathbf{a}) e^{i\mathbf{k}\cdot\mathbf{a}} \tag{2.5.1}$$

In above equation, $\mathbf{A}_{\mu}$ is the coordinate of the nucleus in the reference cell on which φ_{μ} is centered. As described below:

$$\sum_{g} \varphi_{\mathbf{k}}(\mathbf{r} - \mathbf{A} - \mathbf{a}) = \sum_{j}^{n_G} d_j G(\alpha_{j,} \mathbf{r} - \mathbf{A} - \mathbf{a}) \tag{2.5.2}$$

the AOs are expressed as linear combinations of a finite n_G number of Gaussian-type functions (GTFs, denoted as G in Equation 2.7.2) with fixed d_j coefficients and α_j exponents.

GTFs are described as the product of a radial ($\mathbf{R}_l(\mathbf{r})$) and an angular ($Y_l^m(\theta, \varphi)$) term:

$$G(\mathbf{r}) = AY_l^m(\theta,\varphi) R_l(\mathbf{r}) = AY_l^m(\theta,\varphi) \mathbf{r}^l e^{-\alpha r^2} \tag{2.5.3}$$

where A is the normalization term, α is the above-mentioned exponential coefficient and Y_l^m is a spherical harmonic associated with the angular (l) and the magnetic (m) quantum numbers and depends on the angular variables θ and φ. The mathematical formula of GTF-based basis sets makes the calculation of HF exchange faster and simpler with respect to other types of basis sets based on Slater functions with a radial dependence $\sim \mathbf{r}^{n-1} e^{-\mathbf{r}}$ (where n is the principle quantum number). However, GTFs describe poorly the electrons in the proximity of the nuclei, which is overcome by taking into account the linear combination of primitive Gaussians to get contracted Gaussian functions, and the latter are used as basis functions.

In the simplest case of a minimal basis set, one Gaussian basis function is used for each atomic orbital. Auxiliary functions with an additional node called polarization functions can be added to this minimal basis set to increase its flexibility in describing chemical bonds. In practice, it is realized by adding p-functions to a basis set containing s orbitals, d-functions to a basis set with p orbitals etc. Another common modification is to "augment" basis sets, or in other words, to add diffuse functions to provide a better description of the distant tails of Gaussian functions. In periodic systems, however, care must be taken to avoid numerical problems with diffuse functions, and they are omitted in most cases.[42]

When calculating the wave function and total energy of a system composed of two

molecules A and B with a finite basis set, the description of molecule A in the crystal will be improved by the variational freedom provided by the functions of the adjacent molecule B, and vice versa. As a result, the energy content of A and B in the crystalline environment turns out to be overestimated, as if an extra binding occurred between A and B. This is the so-called basis set superposition error (BSSE).[43-44] Boys and Bernardi proposed the counterpoise (CP) method to correct for the BSSE error, by supplementing the basis set of an isolated molecule with the functions of an increasing number of atoms (ghost atoms) belonging to the surrounding array of molecules that would be present in the crystal.[45] Formal dissection of the complex formation process in two separate steps offers a solution to the problem: i) deformation of the components A and B from their equilibrium structures (r_e) to those assumed in the complex (r_c); ii) formation of complex AB from the deformed components. A CP correction would therefore be:

$$E_{int,cp} = E(AB, r_c)^{AB} - E(A, r_e) - E(B, r_e) + E_{def} \tag{2.5.4}$$

with $E(AB,r_c)^{AB}$, $E(A,r_e)$, and $E(B,r_e)$ energy terms of AB, A, and B at their equilibrium structures, respectively, calculated in the full basis of the complex AB, and E_{def}:

$$E_{def} = [E(A, r_c)^{AB} - E(A, r_e)] + [E(B, r_c)^{AB} - E(B, r_e)] \tag{2.5.5}$$

with $E(A,r_c)^{AB}$ and $E(B,r_c)^{AB}$ energy terms of A and B calculated by supplementing the basis set of an isolated molecule with the functions of an increasing ghost atoms belonging to the surrounding array of molecules B and A, respectively.

References

1. Roothaan, C.C.J. New Developments in Molecular Orbital Theory. *Rev. Mod. Phys.* **1951**. *23*, 69–89.
2. Thomas, L.H. The calculation of atomic fields. *Mathematical Proceedings of the Cambridge Philosophical Society* **1927**. *23*, 542–548.
3. Fermi, E. Statistical method to determine some properties of atoms. *Rend. Accad. Naz. Lincei* **1927**. *6*, 5.

4. Dirac, P.A. Note on exchange phenomena in the Thomas atom. In *Mathematical Proceedings of the Cambridge Philosophical Society*, volume 26. Cambridge University Press, 376–385.
5. Hohenberg, P. and Kohn, W. Inhomogeneous electron gas. *Phys. Rev.* **1964**. *136*, B864.
6. Kohn, W. and Sham, L.J. Self-Consistent Equations Including Exchange and Correlation Effects. *Phys. Rev.* **1965**. *140*, A1133–A1138.
7. Langreth, D.C. and Mehl, M.J. Beyond the local-density approximation in calculations of ground-state electronic properties. *Phys. Rev. B* **1983**. *28*, 1809–1834.
8. Perdew, J.P.; Chevary, J.A.; Vosko, S.H.; Jackson, K.A.; Pederson, M.R.; Singh, D.J.; and Fiolhais, C. Atoms, molecules, solids, and surfaces: Applications of the generalized gradient approximation for exchange and correlation. *Phys. Rev. B* **1992**. *46*, 6671–6687.
9. Becke, A.D. Density-functional thermochemistry. I. The effect of the exchange-only gradient correction. *J. Chem. Phys.* **1992**. *96*, 2155–2160.
10. Proynov, E.I.; Ruiz, E.; Vela, A.; and Salahub, D.R. Determining and extending the domain of exchange and correlation functionals. *Int. J. Quantum Chem.* **1995**. *56*, 61–78.
11. Hamann, D.R. Generalized Gradient Theory for Silica Phase Transitions. *Phys. Rev. Lett.* **1996**. *76*, 660–663.
12. Hammer, B. and Scheffler, M. Local Chemical Reactivity of a Metal Alloy Surface. *Phys. Rev. Lett.* **1995**. *74*, 3487–3490.
13. Philipsen, P.; te Velde, G.; and Baerends, E. The effect of density-gradient corrections for a molecule-surface potential energy surface. Slab calculations on Cu(100)c(2x2)CO. *Chem. Phys. Lett.* **1994**. *226*, 583 – 588.
14. Hammer, B.; Jacobsen, K.W.; and Nørskov, J.K. Role of nonlocal exchange correlation in activated adsorption. *Phys. Rev. Lett.* **1993**. *70*, 3971–3974.

15. Ozoliņš, V. and Körling, M. Full-potential calculations using the generalized gradient approximation: Structural properties of transition metals. *Phys. Rev. B* **1993**. *48*, 18304–18307.
16. Filippi, C.; Singh, D.J.; and Umrigar, C.J. All-electron local-density and generalizedgradient calculations of the structural properties of semiconductors. *Phys. Rev. B* **1994**. *50*, 14947–14951.
17. Xiao, H.; Tahir-Kheli, J.; and Goddard, W.A. Accurate Band Gaps for Semiconductors from Density Functional Theory. *J. Phys. Chem. Lett.* **2011**. *2*, 212–217.
18. Martsinovich, N.; Jones, D.R.; and Troisi, A. Electronic Structure of TiO_2 Surfaces and Effect of Molecular Adsorbates Using Different DFT Implementations. *J. Phys. Chem. C* **2010**. *114*, 22659–22670.
19. Corà, F.; Alfredsson, M.; Mallia, G.; Middlemiss, D.S.; Mackrodt, W.C.; Dovesi, R.; and Orlando, R. *The Performance of Hybrid Density Functionals in Solid State Chemistry*. Springer Berlin Heidelberg, Berlin, Heidelberg. **2004**. 171–232.
20. Csonka, G.I.; Perdew, J.P.; and Ruzsinszky, A. Global Hybrid Functionals: A Look at the Engine under the Hood. *J. Chem. Theory Comput.* **2010**. *6*, 3688–3703.
21. Adamo, C. and Barone, V. Toward reliable density functional methods without adjustable parameters: The PBE0 model. *J. Chem. Phys.* **1999**. *110*, 6158–6170.
22. Becke, A.D. Density-functional thermochemistry. III. The role of exact exchange. *J. Chem. Phys.* **1993**. *98*, 5648–5652.
23. Lee, C.; Yang, W.; and Parr, R.G. Development of the Colle-Salvetti correlationenergy formula into a functional of the electron density. *Phys. Rev. B* **1988**. *37*, 785–789.
24. COHEN, A.J. and HANDY, N.C. Dynamic correlation. *Mol. Phys.* **2001**. *99*, 607–615.
25. Xu, X. and Goddard, W.A. The X3LYP extended density functional for accurate descriptions of nonbond interactions, spin states, and thermochemical properties. *Proc. Natl. Acad. Sci. U.S.A.* **2004**. *101*, 2673–2677.

26. Krukau, A.V.; Vydrov, O.A.; Izmaylov, A.F.; and Scuseria, G.E. Influence of the exchange screening parameter on the performance of screened hybrid functionals. *J. Chem. Phys.* **2006**. *125*, 224106.
27. Henderson, T.M.; Izmaylov, A.F.; Scuseria, G.E.; and Savin, A. The importance of middle-range Hartree-Fock-type exchange for hybrid density functionals. *J. Chem. Phys.* **2007**. *127*, 221103.
28. Henderson, T.M.; Izmaylov, A.F.; Scuseria, G.E.; and Savin, A. Assessment of a Middle-Range Hybrid Functional. *J. Chem. Theory Comput.* **2008**. *4*, 1254–1262.
29. Weintraub, E.; Henderson, T.M.; and Scuseria, G.E. Long-Range-Corrected Hybrids Based on a New Model Exchange Hole. *J. Chem. Theory Comput.* **2009**. *5*, 754–762.
30. Marsman, M.; Paier, J.; Stroppa, A.; and Kresse, G. Hybrid functionals applied to extended systems. *Journal of Physics: Condensed Matter* **2008**. *20*, 064201.
31. Towler, M.D.; Zupan, A.; and Causà, M. Density functional theory in periodic systems using local Gaussian basis sets. *Comput. Phys. Commun.* **1996**. *98*, 181 – 205.
32. Delle Piane, M.; Corno, M.; Orlando, R.; Dovesi, R.; and Ugliengo, P. Elucidating the fundamental forces in protein crystal formation: the case of crambin. *Chem. Sci.* **2016**. *7*, 1496–1507.
33. Koch, W. and Holthausen, M.C. *A chemist's guide to density functional theory*. John Wiley & Sons, **2015**.
34. Parr, R.G. Density Functional Theory of Atoms and Molecules. In K. Fukui and B. Pullman, editors, *Horizons of Quantum Chemistry*. Springer Netherlands, Dordrecht. ISBN 978-94-009-9027-2, 5–15.
35. Allen, M.J. and Tozer, D.J. Helium dimer dispersion forces and correlation potentials in density functional theory. *J. Chem. Phys.* **2002**. *117*, 11113–11120.
36. Hobza, P.; šponer, J.; and Reschel, T. Density functional theory and molecular clusters. *J. Comput. Chem.* **1995**. *16*, 1315–1325.
37. Kristyán, S. and Pulay, P. Can (semi) local density functional theory account for the London dispersion forces? *Chem. Phys. Lett.* **1994**. *229*, 175–180.

38. Grimme, S.; Antony, J.; Ehrlich, S.; and Krieg, H. A consistent and accurate ab initio parametrization of density functional dispersion correction (DFT-D) for the 94 elements H-Pu. *J. Chem. Phys.* **2010**. *132*, 154104.
39. Grimme, S. Semiempirical GGA-type density functional constructed with a long-range dispersion correction. *Journal of Computational Chemistry* **2006**. *27*, 1787–1799.
40. Dovesi, R.; Orlando, R.; Civalleri, B.; Roetti, C.; Saunders, V.R.; and ZicovichWilson, C.M. CRYSTAL: a computational tool for the ab initio study of the electronic properties of crystals. *Zeitschrift für Kristallographie-Crystalline Materials* **2005**. *220*, 571–573.
41. Erba, A.; Baima, J.; Bush, I.; Orlando, R.; and Dovesi, R. Large-Scale Condensed Matter DFT Simulations: Performance and Capabilities of the CRYSTAL Code. *J. Chem. Theory Comput.* **2017**. *13*, 5019–5027.
42. Daga, L.E.; Civalleri, B.; and Maschio, L. Gaussian Basis Sets for Crystalline Solids: All-Purpose Basis Set Libraries vs System-Specific Optimizations. *J. Chem. Theory Comput.* **2020**. *16*, 2192–2201.
43. Kestner, N.R. and Combariza, J.E. Basis set superposition errors: theory and practice. *ReV. Comput. Chem.* **1999**. *13*, 99–126.
44. Davidson, E.R. and Feller, D. Basis set selection for molecular calculations. *Chem. Rev.* **1986**. *86*, 681–696.
45. Boys, S. and Bernardi, F. The calculation of small molecular interactions by the differences of separate total energies. Some procedures with reduced errors. *Mol. Phys.* **1970**. *19*, 553–566.

Chapter III

Section 1 Context

As already described in detail in chapter I and shown in **Figure 3.1.1(a)**, the general working principle of a PSC device with MAPI as light absorbing layer is: i) generation of charge carriers under irradiation; ii) transport of charge carriers; iii) carriers' migration to the electrode. During this process, TiO_2 is used as an ETM. Among the three main crystal polymorphs of TiO_2, anatase is a possible candidate for PV due to its remarkably higher specific surface area. When acting as an ETM, anatase can form electron selective contact with the perovskite layer, improve the extraction efficiency of photogenerated electrons, effectively block the migration of holes toward the cathode, balance the transport of carriers in each layer and shorten the migration distance of photogenerated electrons. Despite these advantages, there are still some breakthroughs left, which may help improve the whole performance of the device. For example, since the PSC device is fabricated by different layers, there exists an interface energetic difference between each layer. How to optimize this energetic is then a key question, especially for the interface between ETL and perovskite. In this context, interfacial engineering is becoming essential to improve solar cells performance.[1-4] Usually, this is done by adsorption of molecules on TiO_2 anatase surface, with these molecules functioning as a bifunctional linker to connect the anatase and perovskite moieties. The adoption of such molecules will bring the following benefits: i) they can impart a dipole at the donor-acceptor interface and shift the interface energy offset upon attachment; ii) they can affect the energy levels of the donor-acceptor pair; iii) their molecular orbitals can form electronic states at the interface, which may block or mediate forward charge transfer or reduce back charge recombination; iv) they can passivate inorganic surface states by chemically interacting with surface dangling bonds; v) they can also act as energy acceptors if their absorption spectrum corresponds to a suitable region.[5] These conclusions are mainly derived from the experimental studies. On the other hand, first principles calculations can also help us to better understand the mechanisms at play in such systems. A first step is understanding how these molecules adsorb on the anatase surface. Four molecules are here introduced and

adsorbed onto the TiO_2 anatase (101) surface (**Figure 3.1.1(b)**), to characterize the structural and electronic properties of the resulting systems. Based on the obtained results, the best candidate molecule can then be selected for PV application and the involved mechanism can be better understood.

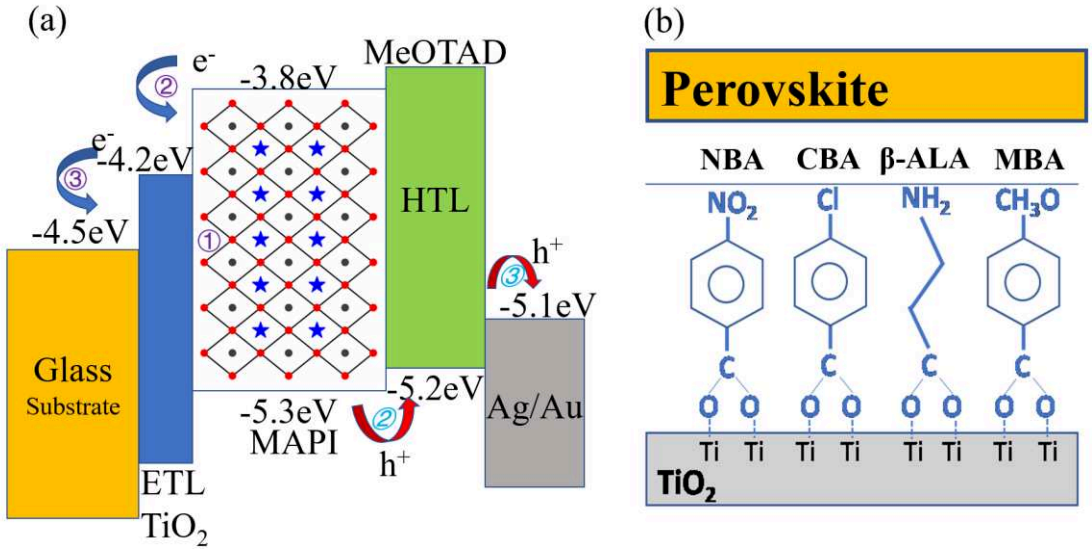

Figure 3.1.1: (a) Working mechanism diagram of PSC device with MAPI as the light absorbing layer. (b) Schematic of the acids self-assembled interlayer between TiO2 and Spiro-OMetAD. From left to right: 4-Chlorobenzoate (CBA); 4-methoxybenzoate (MBA); 4-Nitrobenzoate (NBA) and β-ALAnine (β-ALA).

This chapter is organized as follows: after a description of the computational details, calculations performed on TiO_2 anatase bulk and (101) surface are presented. Then, four small organic molecules are introduced and their adsorption on the anatase surface is discussed. Finally, the best candidates are selected according to the results. This work has been performed in collaboration with the experimental group of Prof. Thierry Pauporté from Chimie Paristech who provided all experimental data presented below.

Section 2 Computational details

All calculations were carried out with the ab initio CRYSTAL17 code,[6-7] which is based on a linear combination of atom-centered Gaussian orbitals and solves self-consistently Hartree-Fock and Kohn-Sham equations.

The (101) surface of the anatase phase of TiO_2 was considered for the adsorption of the ligands since this surface is well-known to be highly stable and reactive.[8-10] A two-dimensional periodic slab with 4-Ti layers was cut out from the TiO_2 anatase bulk

system ($I4_1$/amd space group) with the following PBE0-D3 optimized cell parameters: 3.7578 Å (a), 9.7039 Å (c). The slab obtained here is used as a starting point for the adsorption, and a rectangular (2x1) supercell was considered in order to avoid artificial interaction between adsorbates from one cell to the other due to the 2D periodicity of the model. The *a* and *b* lattice parameters for this supercell slab model are 7.4906 Å and 5.5442 Å, respectively, corresponding to a surface coverage of one ligand molecule per 3.9 nm^2. Sampling of the irreducible Brillouin zone was done with 7 **k** points for this system. Numerical DFT integration was performed considering 75 radial points and 974 angular points, ensuring an error on the integrated electron density lower than 10^{-5} |e-| per unit cell. The Coulomb and exchange series were truncated with threshold values of 10^{-7}, 10^{-7}, 10^{-7}, 10^{-7}, and 10^{-18}.

Organic ligands were described using all electron basis sets with (621/21/1), (7311/311/1), (8411/411/1), (511/1) and (86311/6311) for C, N, O, H and Cl atoms, respectively. Durand and Barthelat large core pseudopotentials with (1/1/41) and (31/31) contractions were used for Ti and O atoms of the TiO_2 substrate, respectively.[11-12]

Exchange and correlation energies were described using the global hybrid PBE0 functional,[13] with 25% of HF exchange. Additional D3 dispersion corrections were also included.[14-15]

To simulate the experimental environment, the solvent, methanol, was added to the models, considering a molecular binding mode to the TiO_2 surface. As described in the manuscript, this allows to limit the tilting of the different ligands adsorbed on the surface.

For surface energies of TiO_2 slab ($E_{surface}$), it was calculated by:

$$E_{surface} = \frac{E_{slab}(n) - n \cdot E_{bulk}}{2 \cdot A} \quad (3.2.1)$$

where $E_{slab}(n)$ is the energy of the slab; n is the number of the layer; E_{bulk} is the corresponding TiO_2 bulk energy; A is the surface area.

For adsorption energies (E_{ads}), total adsorption energies of ligand and methanol ($E_{ads\text{-}total}$) were first computed, as the difference between the total energies ($E_{adsorbate\text{-}surface}$) of the combined adsorbate/substrate system and the sum of the relaxed energies of a TiO_2 surface with a H^+ ($E_{surface+H}$) and a negatively charged adsorbate molecule in the gas phase ($E_{ligand\text{-}}$), and a methanol molecule in the gas phase (E_{CH3OH}) as:

$$E_{ads\text{-}total} = E_{adsorbate\text{-}surface} - (E_{surface+H} + E_{ligand\text{-}} + E_{CH3OH}) \quad (3.2.2)$$

The adsorption energy of methanol $E_{ads\text{-}methanol}$ was calculated with the following

formula:

$$E_{ads\text{-}methanol} = E_{CH3OH\text{-}surface} - (E_{surface} + E_{CH3OH}) \quad (3.2.3)$$

with $E_{ads\text{-}methanol}$ corresponding to the difference of the total energy of the CH_3OH/TiO_2 system ($E_{CH3OH\text{-}surface}$) and the sum of the relaxed energies of a bare TiO_2 surface ($E_{surface}$) and the CH_3OH molecule (E_{CH3OH}). Finally, the adsorption energies of the ligands ($E_{ads\text{-}ligand\text{-}}$) was computed as the difference between $E_{ads\text{-}total}$ and $E_{ads\text{-}methanol}$:

$$E_{ads\text{-}ligand\text{-}} = E_{ads\text{-}total} - E_{ads\text{-}methanol} \quad (3.2.4)$$

A negative value of $E_{ads\text{-}ligand}$ corresponds a thermodynamically favored adsorption process.

During geometry optimization, only atomic positions were allowed to relax, while lattice parameters were constrained to those of the supercell mentioned above. Numerical harmonic frequency calculations were performed at the Γ-point on the optimized structures in order to compute the IR spectra of the adsorbed molecules. To limit computational cost, only the first TiO_2 layer and the adsorbed ligand and methanol molecule were included in the Hessian construction. Test calculations including more TiO_2 layers showed negligible differences with values discussed here.

Section 3 Bulk anatase and its slab

Figure 3.3.1(a) depicts the tetragonal structure of anatase which is formed by chains of distorted TiO_2 octahedra. In an octahedra, each Ti atom is coordinated to the six neighboring oxygen atoms through two apical and four equatorial bonds of lengths 1.979 and 1.932 Å at 295 K, respectively. These values were obtained from the Rietveld analysis of time-of-flight pulsed neutron diffraction of powders, and the structure diagram is shown in **Figure 3.3.1(b)**.[16]

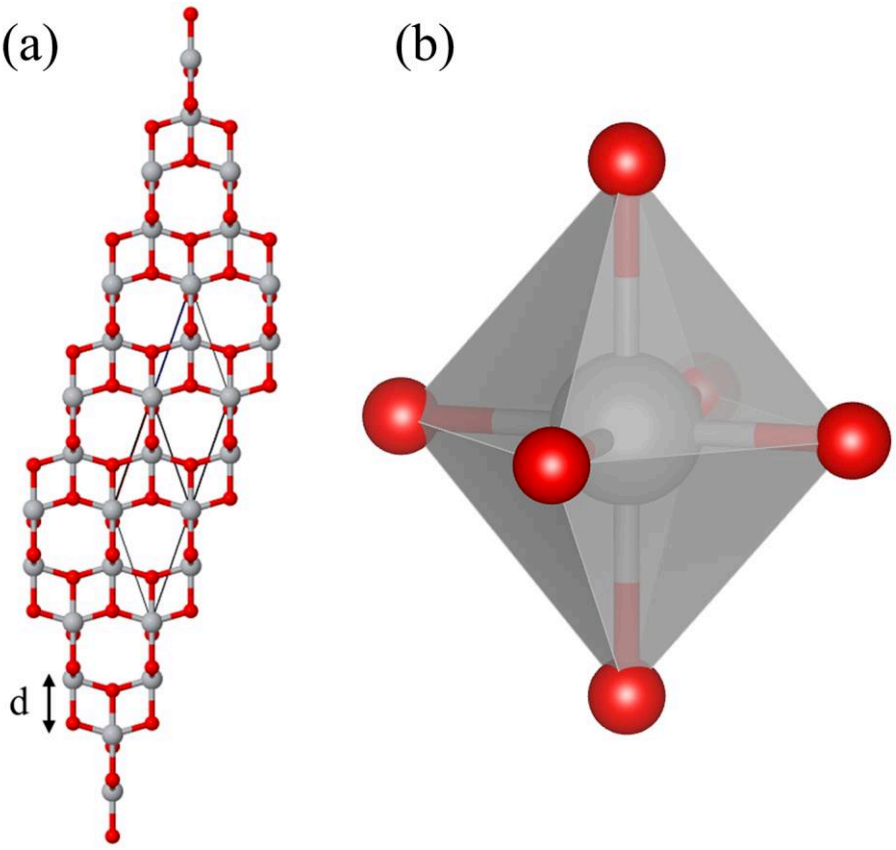

Figure 3.3.1: (a) Tetragonal structure of anatase. Its space group number is 141 with experimental cell edge parameters *a* and *c* equaling to 3.782 and 9.502 Å, respectively. The length of the Ti-O apical bond is described by *d*, where the value is 1.979 Å. (b) Schematic diagram of TiO_2 octahedra. It should be mentioned that the actual octahedra is distorted. The titanium and oxygen atoms are represented by silver and red balls, respectively.

The optimized structure parameters are listed in **Table 3.3.1**, and results from experiments are also given for comparison. It can be seen that the calculated *a* is smaller while *c* is larger than the experimental value, which means there is a contraction in the horizontal direction while an expansion in the vertical direction for the calculated system. As for the bandgap, an overestimation has been observed in our results. This is due to the contribution of 25% of exact exchange in the hybrid functional PBE0. Lower amounts of 12−15% have been reported to better match the experimental fundamental gap of TiO_2.[17]

Table 3.3.1: Calculated and experimental lattice parameters and bandgap of bulk anatase.

	a (Å)	c (Å)	Bandgap (eV)
Calculated (PBE0-D3)	3.745	9.742	4.14
Experimental[16]	3.782	9.502	Between 3.2 and 3.6

Based on the bulk structure, an eight-layer TiO_2 slab with (101) surface exposed was built, and the model is shown in **Figure 3.3.2**. From the oblique top view (**Figure 3.3.3(c)**), both 5-fold- (Ti_{5C}, an example atom marked as C) and 6-fold- (Ti_{6C}, an example marked as B) coordinated Ti atoms as well as 2-fold- and 3-fold-coordinated O atoms (O_{2C}, O_{3C}) can be observed. The dangling bond in these un-fully coordinated atoms gives a possibility for a molecule's adsorption. The calculated lattice parameters and bandgap of TiO_2 slab with (101) surface exposed are given in **Table 3.3.2**. The bandgap of the slab is larger than that of bulk and the surface energy equals to 0.94 $J \cdot m^{-2}$ which indicates a stable surface. All conclusions are in line with previously-reported data on this surface.[18-19]

Table 3.3.2: Calculated lattice parameters and bandgap of TiO_2 slab with (101) surface exposed.

	a (Å)	*b* (Å)	γ (°)	Bandgap (eV)	Surface Energy ($J \cdot m^{-2}$)
TiO_2-(101)-Slab	3.745	5.544	109.74	5.05	0.94

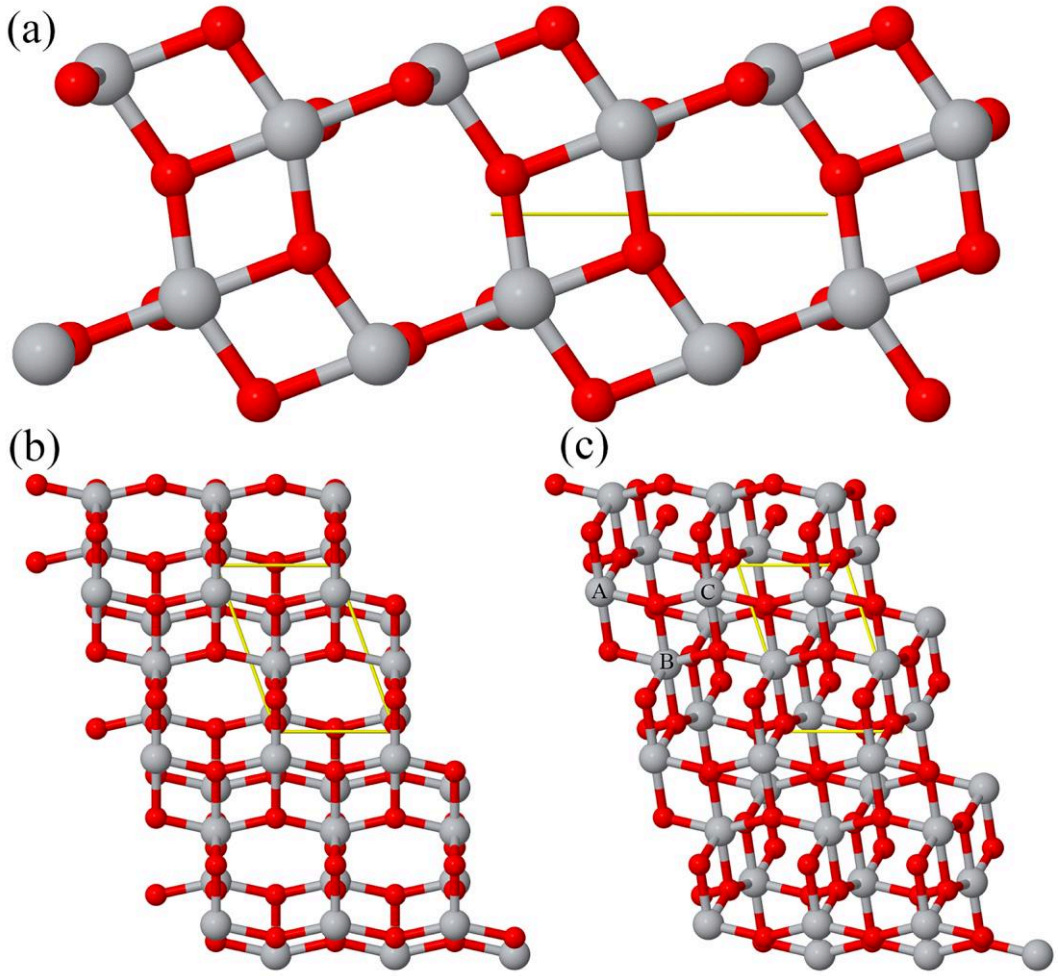

Figure 3.3.2: Schematic diagram of the TiO_2 slab with (101) surface exposed. Grey and red balls represent, respectively, Ti and O atoms. (a) Front view. (b) Top view. (c) Oblique top view with A, B and C labelling typical Ti atoms.

Section 4 Ligands adsorption on anatase (101) surface

In this section, the results about ligands adsorption on anatase (101) surface are discussed.

The structure of four considered molecules are given in **Figure 3.4.1**. All of them have a carboxylic group which can be dissociated and interact with the anatase (101) surface following a bidentate binding mode,[20-23] according to:

$$\text{-COOH} \rightarrow \text{-COO}^- + \text{H}^+ \qquad (3.4.1)$$

The O-H bond is broken and the H^+ specie is adsorbed onto an O_{2C} atom of the anatase surface. In the bidendate bridging mode, each oxygen atom in the -COO functional group is bound to a different Ti_{5C} atom of the surface, with very similar O-

Ti distances.

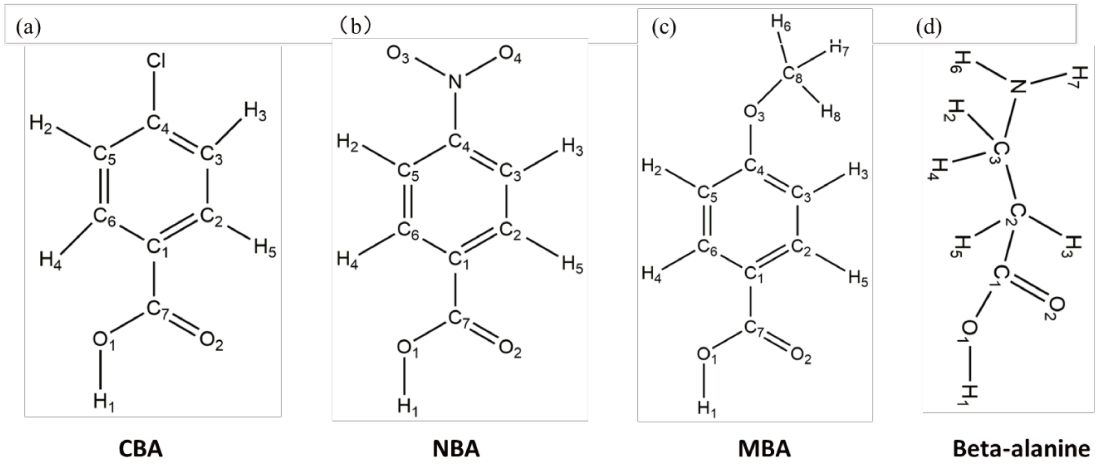

Figure 3.4.1: Molecular structure and atom labelling of (a) CBA, (b) NBA, (c) MBA and (d) β-ALA.

Table 3.4.1: Selected geometrical parameters (Angles in deg; Distances in Å) for isolated and adsorbed molecular systems and corresponding adsorption energies (in kcal/mol) and tilt angle to the surface normal (θ_a). The atom labels correspond to the one used in **Figure 3.4.1**.

Distance(Å)	CBA	CBA@TiO_2	Distance(Å)	NBA	NBA@TiO_2
dO_1C_7/dO_2C_7	1.35/1.21	1.26/1.27	dO_1C_7/dO_2C_7	1.35/1.21	1.26/1.27
dC_1C_7/dC_4Cl	1.48/1.79	1.48/1.79	dC_1C_7/dC_4N	1.49/1.47	1.49/1.48
dH_2C_5/dH_3C_3	1.09/1.09	1.09/1.09	dH_2C_5/dH_3C_3	1.09/1.08	1.08/1.08
dH_4C_6/dH_5C_2	1.09/1.09	1.08/1.09	dH_4C_6/dH_5C_2	1.09/1.09	1.08/1.09
dO_1Ti/dO_2Ti	-	2.15/2.06	dO_3N/dO_4N	1.22/1.22	1.22/1.22
			dO_1Ti/dO_2Ti	-	2.16/2.05
θ_a		30.3°	θ_a		31.6°
$E_{ads\text{-}ligand\text{-}}$		-20.73	$E_{ads\text{-}ligand\text{-}}$		-11.33
Distance(Å)	MBA	MBA@TiO_2		β-ALA	β-ALA@TiO_2
dO_1C_7/dO_2C_7	1.35/1.21	1.27/1.27	dO_1C_1/dO_2C_1	1.35/1.21	1.26/1.27
dC_1C_7/dC_4O	1.47/1.36	1.48/1.35	dC_1C_2/dC_2C_3	1.51/1.54	1.51/1.52
dH_2C_5/dH_3C_3	1.09/1.09	1.09/1.08	dC_3N_1	1.46	1.46
dH_4C_6/dH_5C_2	1.09/1.09	1.08/1.09	dH_2C_2/dH_3C_2	1.10/1.09	1.10/1.10
$dOC_8/dH_{6\text{-}8}C_8$	1.41/1.10	1.35/1.10	dC_3H_4/dC_3H_5	1.10/1.10	1.10/1.09
dO_1Ti/dO_2Ti	-	2.16/2.04	dNH_6/dNH_7	1.02/1.01	1.02/1.01
			dO_1Ti/dO_2Ti	-	2.13/2.08
θ_a		31.6°	θ_a		13.4°
$E_{ads\text{-}ligand\text{-}}$		-30.62	$E_{ads\text{-}ligand\text{-}}$		-20.20

The molecules were adsorbed onto a 2*1 supercell of anatase (101) surface slab, in order to minimize spurious interaction between periodically-repeated adsorbed

molecules.

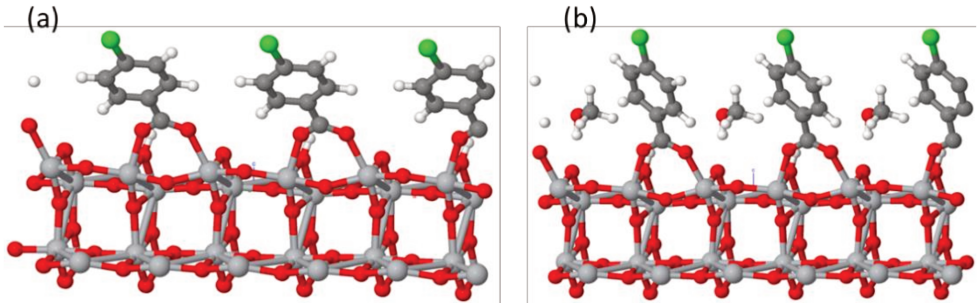

Figure 3.4.2: Optimized structure of CBA molecules adsorbed on anatase TiO_2 (101) surface without (a) and with (b) methanol solvent. The carbon, titanium, oxygen, chloride and nitrogen atoms are represented by grey, silver, white, red, green and blue balls, respectively.

Experimentally, solvent environment is used to adsorb such ligands on the TiO_2 anatase (101) surface. Here, the solvent environment is approximated by a single explicit methanol molecule per unit cell. **Figure 3.4.2** presents the optimized DFT structure of CBA adsorbed on anatase both without (a) and with an explicit methanol solvent molecule (b). A large tilting of the benzene ring compared to the vertical position is observed. This tilting is found for all the benzoic acid derivatives and for β-ALA (**Figure 3.4.3**). The tilt angle (θ_a) is reduced and the molecules are straightened when an explicit solvent molecule (methanol, the solvent used experimentally for the acid treatment of the surface) is considered. For instance, the angle changed from 42° to 30° in the case of CBA. θ_a for various acids are gathered in **Table 3.4.1**. The tilting is more relevant for the benzoic acids compared to β-ALA due to the π-interaction between H^+ atom on the surface and the ring. **Table 3.4.1** also reports the adsorption energies of each molecule. All values are negative, corresponding to a thermodynamically favored process. From the computed adsorption energies, it can be seen that the stability order is MBA > CBA > B-ALA > NBA (from stable to less stable). Furthermore, only the distances related to the C-O of the carboxylic groups change after relaxation, indicating again a dissociative adsorption process with two non-equivalent O-Ti distances.

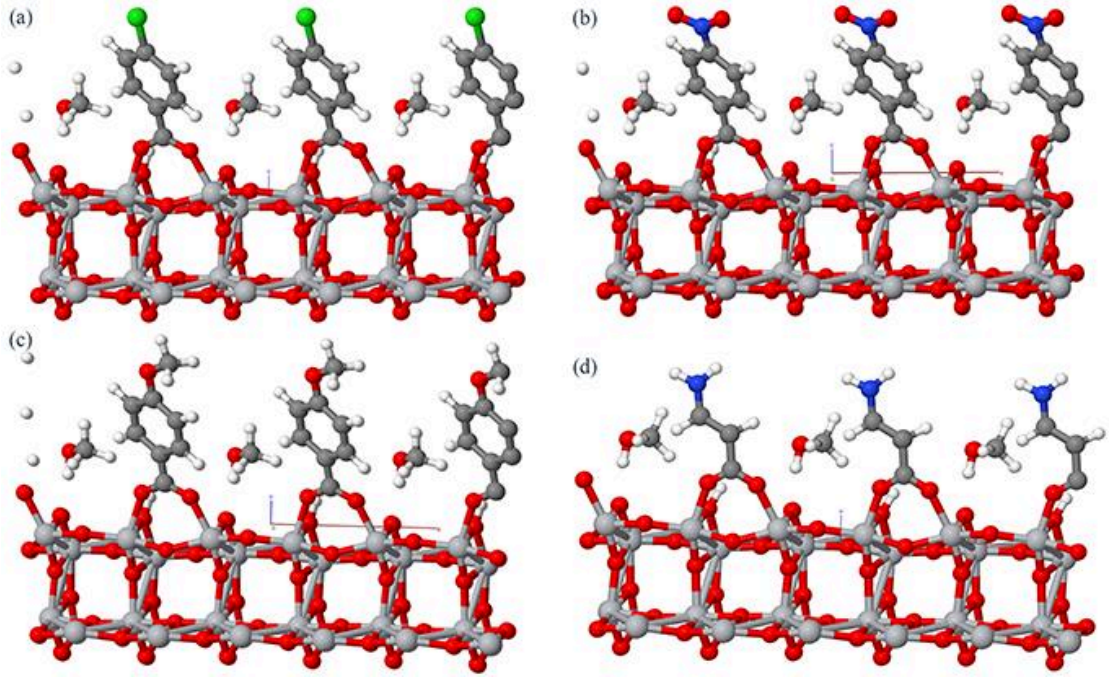

Figure 3.4.3: Optimized structure of the 4 acids adsorbed onto anatase (101) surface. The carbon, titanium, oxygen, chloride and nitrogen atoms are represented by grey, silver, white, red, green and blue balls, respectively. (a) CBA, (b) NBA, (c) MBA and (d) β-ALA.

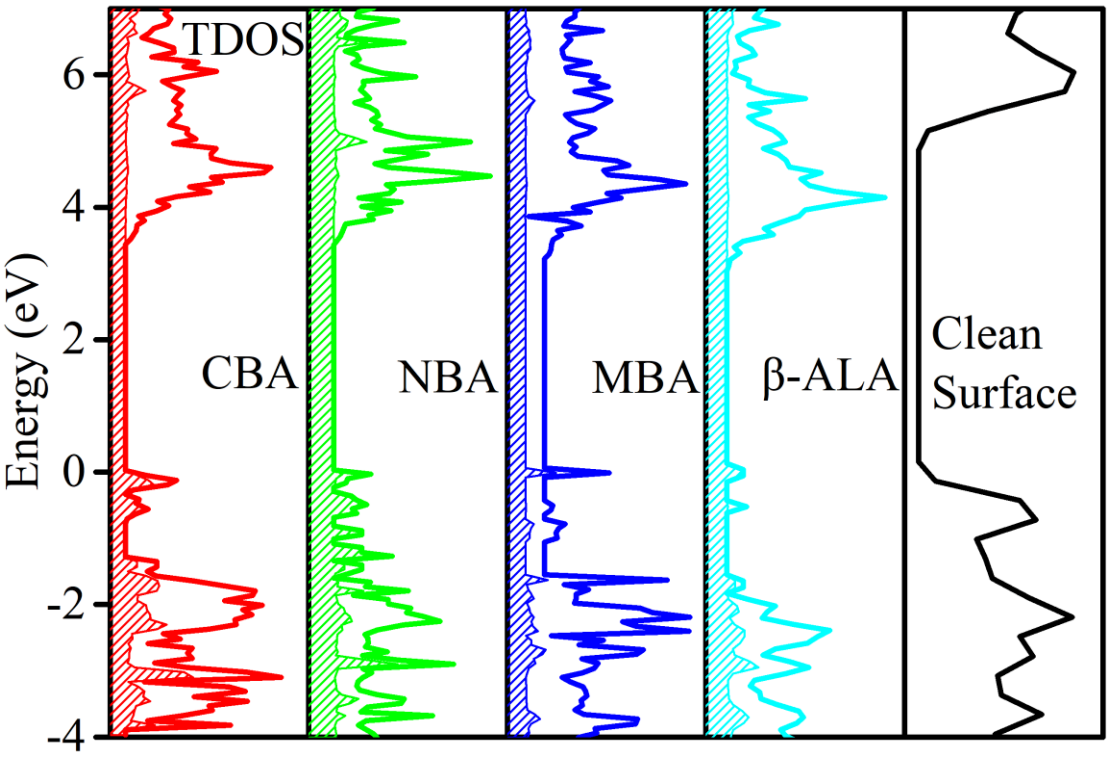

Figure 3.4.4: Comparison of total densities of states (TDOS) of clean TiO_2 surface and Ligand/TiO_2. The shadow is the corresponding ligand project density of states (PDOS).

Figure 3.4.4 presents a comparison between the total densities of states (TDOS)

of the clean TiO_2 surface and of the corresponding systems with the ligands adsorbed. For the adsorbed systems, the value of clean TiO_2 surface bandgap decreases. More precisely, the bandgap values of the clean TiO_2 surface and of the surface with the CBA, NBA, MBA and β-ALA adsorbates are of 5.05, 3.49, 3.43, 3.28 and 3.07 eV, respectively. This is mainly due to the contribution of the ligands to the top of the valence band. Thus, it is concluded that the ligands can modify the electronic structure of the TiO_2 surface, with a possible important role in the band alignment found at an interface.

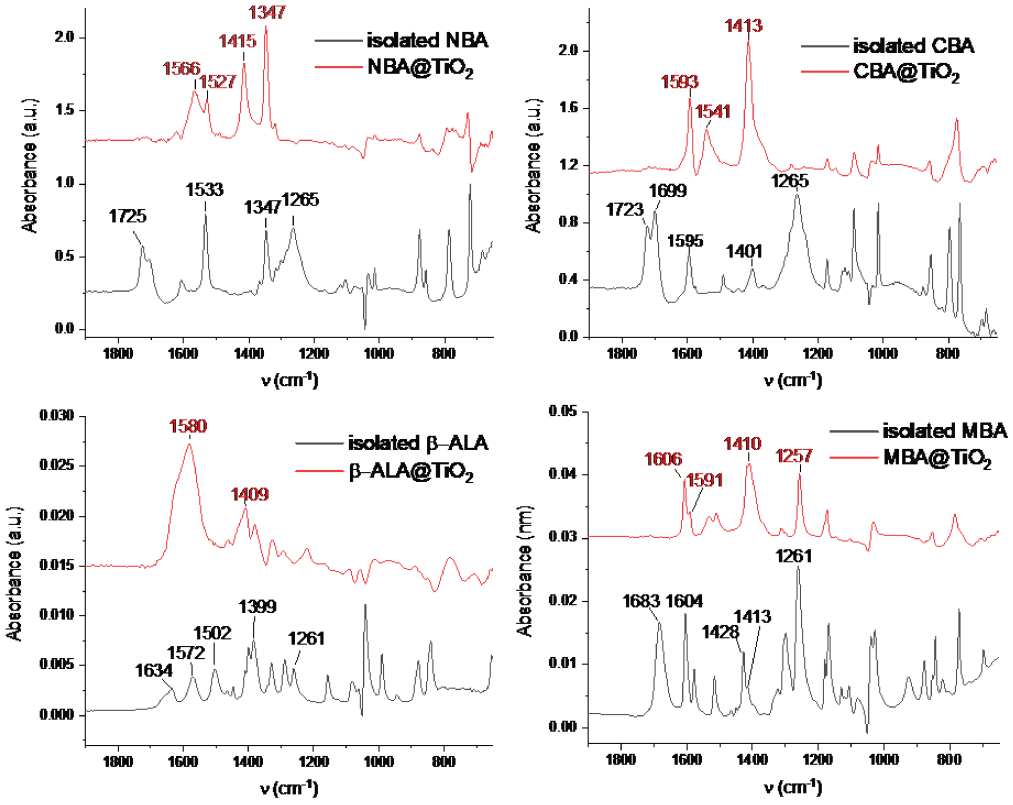

Figure 3.4.5: Experimental FTIR spectra of the modifiers dissolved in ethanol (black) and adsorbed on TiO_2 nanoparticles (red). (a) NBA, (b) CBA, (c) β-ALA and (d) MBA.

To further validate the adsorption models considered, the theoretical FTIR bands were calculated and compared with that from experimental results.[24] The calculated and measured -COO ν_{as} and ν_s wavenumbers are given in **Table 3.4.2**. The overall spectra are shown in **Figure 3.4.5**.

For the benzoic acid derivatives, a band at 1680-1723 cm^{-1} was observed (twinned in the case of NBA and CBA) which are assigned to a C=O stretching vibration.[25-30]

This mode is shifted in the case of β-ALA and found at 1633 cm^{-1}. These bands disappeared in all cases after the attachment onto the TiO_2 surface. The bands observed at 1533 cm^{-1} (NBA), 1595 cm^{-1} (CBA) and 1604/1595/1515 cm^{-1} (MBA) remain after the binding of the benzoic acid derivatives and are assigned to C=C stretching modes. For the β-ALA, bands are observed at 1572 cm^{-1} and 1502 cm^{-1} which correspond to antisymmetric and symmetric bending modes, respectively.[31] For all the isolated acids, a band is found at 1261-1265 cm^{-1} which is assigned to the COO symmetric stretching mode (ν_s), while the bands at 1347 cm^{-1} (NBA) /1401 cm^{-1} (CBA)/ 1428 cm^{-1} (MBA)/ 1399 cm^{-1} (β-ALA) are assigned to the antisymmetric stretching mode (ν_{as}) of -COO. After adsorption, these modes are significantly shifted at higher wavenumbers (frequency) and found at 1415 cm^{-1} (NBA)/ 1413 cm^{-1} (CBA)/ 1410 cm^{-1} (MBA)/ 1409 cm^{-1} (β-ALA) for ν_s and 1566 cm^{-1} (NBA)/ 1593 cm^{-1} (CBA)/ 1591 cm^{-1} (MBA)/ 1580 cm^{-1} (β-ALA) for ν_{as}. The comparison of the peaks' wavenumbers is given as below.

Table 3.4.2: Selected computed and experimental IR wavenumbers of isolated acids and acids on anatase surface. Δ_1 is the difference between the experimental and calculated data, and Δ_2 is the difference between the wavenumber of symmetric (ν_s) and antisymmetric (ν_{as}) stretching of -COO bonds. All data in cm^{-1}.

		Isolated			Adsorbed@TiO_2		
		Calc.	Exp.	Δ_1	Calc.	Exp.	Δ_1
CBA	ν_s	1215	1265	50	1472	1413	-59
	ν_{as}	1395	1401	6	1590	1593	3
	Δ_2	180	136		118	180	
NBA	ν_s	1215	1265	50	1473	1415	-58
	ν_{as}	1395	1347	-48	1598	1566	-32
	Δ_2	180	82		125	151	
MBA	ν_s	1219	1261	42	1467	1410	-57
	ν_{as}	1399	1428	29	1585	1591	6
	Δ_2	180	167		118	181	
β-ALA	ν_s	1218	1261	43	1497	1409	-88
	ν_{as}	1392	1399	7	1585	1580	-5
	Δ_2	174	138		88	171	

Δ_1 in **Table 3.4.2** is the wavenumber difference between the theoretical calculations and the experimental results. A generally good agreement is obtained between the computed and the experimental data. In particular, in most cases, Δ_1 is lower than 50 cm^{-1}, and a shift at higher wavenumbers is obtained after the molecule binding to the TiO_2 surface. The computed wavenumber difference between the antisymmetric and the symmetric stretching modes (Δ_2) is, as expected, the same for all the isolated benzoic acid derivatives (180 cm^{-1}) and slightly lower in the case of isolated β-ALA. On the other hand, for the adsorbed compounds Δ_2 varies as a function of the acid considered. When adsorption occurs, the environment of the COO^- moiety changes, its symmetric and antisymmetric stretchings are affected and the corresponding Δ_2 value decreases. This change may also indicate the dissociation process of carboxylic acid and confirms that a bridging bidentate binding mode is obtained for all ligands adsorbed on TiO_2.

Table 3.4.3: Charge transfer ($|e^-|$) and normal component of the dipole moment with respect to the TiO_2 surface of the acids adsorbed on TiO_2 ($\mu_\perp$). Corresponding calculated values for the isolated molecules are reported in parentheses.

	NBA	CBA	β-ALA	MBA
Charge transfer from molecule to TiO_2 ($\|e^-\|$)	0.26	0.26	0.21	0.26
$\mu_\perp$(D)	2.22 (3.72)	0.89 (1.55)	0.12 (2.79)	-0.5 (-2.57)

Due to the polarization of these molecules, their adsorption induces the presence of a dipole moment at the TiO_2 surface.[5] The dipole component normal to the surface ($\mu_\perp$) introduces a step in the local vacuum level due to the electric field across this layer. The work function and the band edge of the TiO_2 surface is changed by $q\Delta V$ where q is the elemental charge. ΔV is expressed by the Poisson's equation:

$$\Delta V = \frac{N_s \mu_\perp \cos\theta_a}{\varepsilon_r \varepsilon_0} \tag{3.4.2}$$

with N_s the surface dipole density, $\mu_\perp$ the normal dipole moment, θ_a the tilt angle of the dipole versus the surface normal, ε_r the dielectric constant and ε_0 the permittivity of free space.

The dipole moment values calculated by DFT for the various acids are gathered in **Table 3.4.3**. The order is NBA>CBA>β-ALA>MBA. We note that $\mu_\perp$ of MBA is negative (dipole moment pointing toward TiO_2 in the chemistry notation). In the same table, we also report the values calculated for the free molecules. After adsorption, the magnitude of all the dipole moments decreased due to two phenomena: the charges transfer to the TiO_2 surface combined to the tilting obtained on the surface. More precisely, while a charge transfer to the TiO_2 surface of about 0.26 $|e^-|$ is computed for CBA, NBA and MBA, β-ALA shows a lower charge transfer of about 0.21 |e-|, resulting in a lower generated photocurrent in the device.

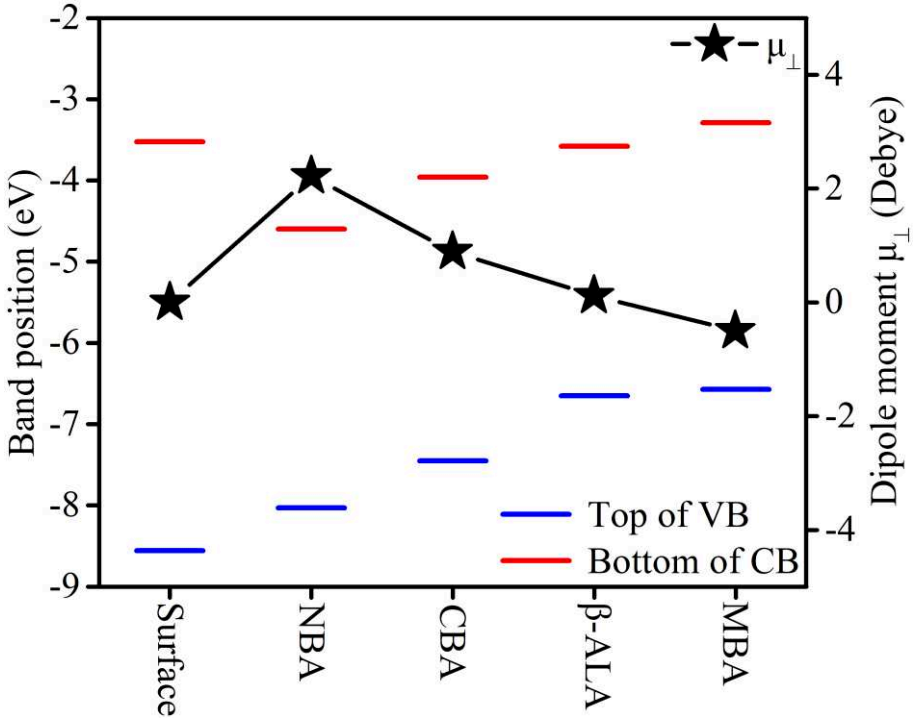

Figure 3.4.6: Positions of the bottom of the conduction band (CB) and the top of the valence band (VB). Dipole moment component along the normal to the TiO_2 surface is also reported.

Figure 3.4.6 shows the dipole moments and band edge positions. Compared to the clean surface, upon adsorption, the top of the valence band (VB) of all adsorbed systems as well as the bottom of the conduction band (CB) of MBA adsorbed system are shifted to higher energies, while the bottom of the CB of CBA, NBA and β-ALA adsorbed systems are shifted to lower energies. This indicates again that the adsorption of ligands does influence the band edge positions. In particular, from this plot, we can see that MBA seems to be not suitable for the targeted application. Furthermore, with a larger dipole moment, the band edges tend to be higher. This may be related to the vacuum level induced by the adsorbed molecules.

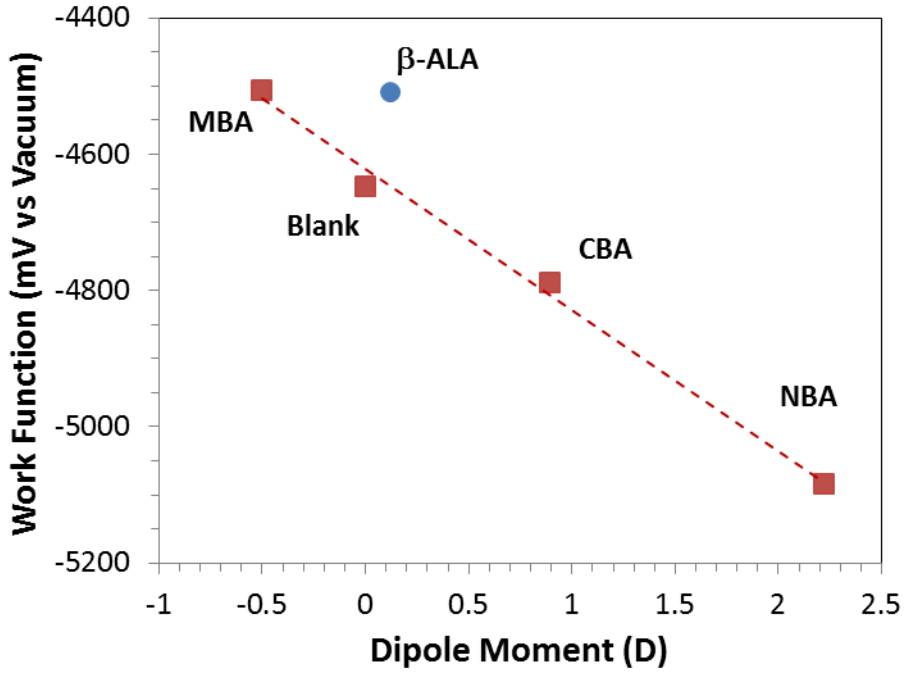

Figure 3.4.7: Work function versus the calculated dipole moment ($\mu_{\perp}$) of the molecules adsorbed onto TiO_2. The work function data is from experiments.[24]

The change in the local vacuum level can be quantified by measuring the work function of the bare TiO_2 layer and of the modified layers. The results are shown in **Figure 3.4.7**. For the blank and the benzoic acids, a linear relationship is found which is in agreement with Equation (3.4.2). A special behavior is found for β-ALA, the point being outside the of straight line. The experimental values suggest that its dipole moment should be negative and thus β-ALA can be excluded as a potential suitable candidate for PSC application.[24]

From the above results, the effects of molecule modifiers can be explained. The presence of the dipoles at the interface introduces an additional electric field. When the dipole field is pointing outward titania, the vacuum level is shifted upward and the work function is increased. When electron-hole pairs are photogenerated in the light absorbing layer, the electrons are drifted toward the TiO_2 layer, and the charge separation and transfer are facilitated. On the contrary, for the adsorbed molecules with a dipole moment pointing toward the oxide, the vacuum energy level is shifted downward, the work function is reduced. An interfacial electric field is present that reduces the electron charge transfer toward TiO_2 and induces a negative effect on electron transport. These phenomena are schematically presented in **Figure 3.4.8**. **Figure 3.4.8** also shows the effect of the modifier on the V_{OC}. The V_{OC} is limited by the $E_C(TiO_2)$-E_{HOMO}(light-absorbing-layer) gap. The presence of a dipole layer changes this gap: it is reduced for a dipole with a positive $\mu_\perp$ (**Figure 3.4.8(a)**) and increased for a dipole with a negative $\mu_\perp$ (**Figure3.4.8(c)**). Therefore, in the former case, the V_{OC} will be reduced while this parameter will be increased in the latter case.

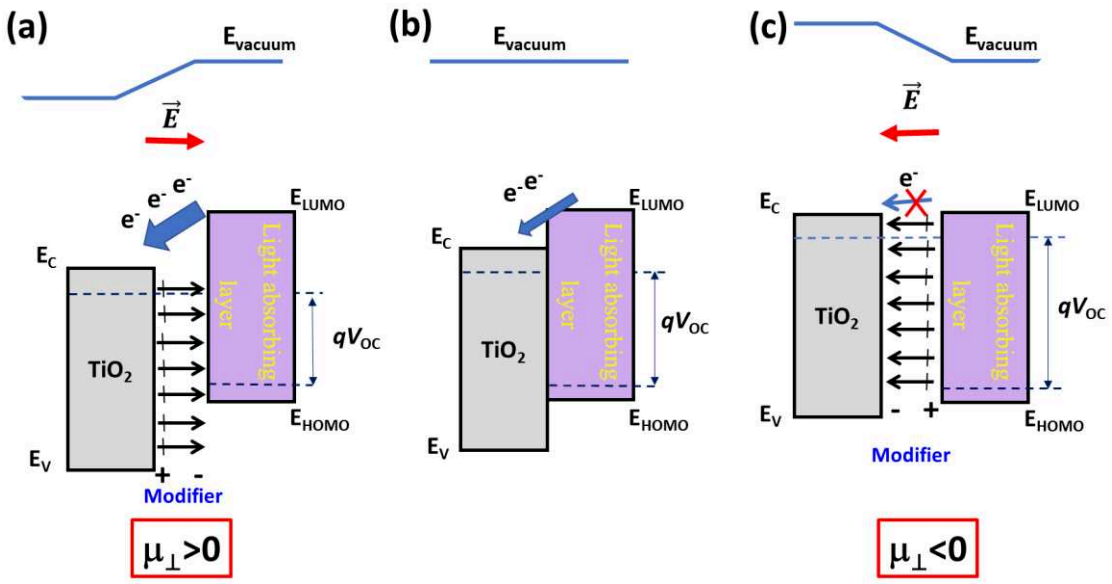

Figure 3.4.8: Effect of the interfacial dipole modifiers on the energetics of the TiO_2/light-absorbing-layer heterojunction. (a) Dipole inducing a $\mu_\perp > 0$ at the interface; (b) pristine interface and (c) dipole inducing a $\mu_\perp < 0$ at the interface.

From the data above, we find that all molecules can form stable adsorption following a bidentate binding mode on anatase (101) surface with methanol as solvent. Furthermore, all ligands can help improve the band alignment. These molecules can

induce a dipole moment to the system after adsorption, and this is the key criteria to select the most suitable candidate. From this investigation, CBA and NBA can thus be considered as suitable candidates as ligands for PSC application.

Section 5 Conclusion

In summary, we conducted DFT calculations on TiO_2 anatase bulk, (101) surface and adsorption of four small organic ligands on the latter. Although an overestimation of the bulk bandgap is obtained, the experimental lattice parameters of the bulk system are well reproduced. Based on the relaxed anatase (101) surface slab model, a supercell was created and the molecule adsorption models were built. The analysis of the absorption energies, lattice parameters as well as the vibrational frequencies supports a bidentate binding mode for all ligands on the TiO_2 surface, with a general good agreement with available experimental data. The DOS and band edge positions indicate that ligands can modify the band edge positions. A simple model based on computed dipole moments and measured work functions could explain how the chosen ligands may help to improve the charge transfer and confirm that CBA and NBA are better candidates than MBA and β-ALA for PSC application. Therefore, calculations are in good agreement with the experimental results, indicating that the modeling strategy considered can help to better understand the mechanisms involved and provide useful guidelines for choosing suitable ligand candidates at the experimental level.

References

1. Liu, Y.; Scully, S.R.; McGehee, M.D.; Liu, J.; Luscombe, C.K.; Fréchet, J.M.J.; Shaheen, S.E.; and Ginley, D.S. Dependence of Band Offset and Open-Circuit Voltage on the Interfacial Interaction between TiO_2 and Carboxylated Polythiophenes. *J. Phys. Chem. B* **2006**. *110*, 3257–3261.
2. Durrant, J.R.; Haque, S.A.; and Palomares, E. Towards optimisation of electron transfer processes in dye sensitised solar cells. *Coord. Chem. Rev.* **2004**. *248*, 1247 – 1257.

3. Cohen, R.; Kronik, L.; Shanzer, A.; Cahen, D.; Liu, A.; Rosenwaks, Y.; Lorenz, J.K.; and Ellis, A.B. Molecular Control over Semiconductor Surface Electronic Properties: Dicarboxylic Acids on CdTe, CdSe, GaAs, and InP. *J. Am. Chem. Soc.* **1999**. *121*, 10545–10553.
4. Moser, J.; Punchihewa, S.; Infelta, P.P.; and Graetzel, M. Surface complexation of colloidal semiconductors strongly enhances interfacial electron-transfer rates. *Langmuir* **1991**. *7*, 3012–3018.
5. Goh, C.; Scully, S.R.; and McGehee, M.D. Effects of molecular interface modification in hybrid organic-inorganic photovoltaic cells. *J. Appl. Phys.* **2007**. *101*, 114503.
6. Dovesi, R.; Erba, A.; Orlando, R.; Zicovich-Wilson, C.M.; Civalleri, B.; Maschio, L.; Rérat, M.; Casassa, S.; Baima, J.; Salustro, S.; and Kirtman, B. Quantum-mechanical condensed matter simulations with CRYSTAL. *WIREs Comput. Mol. Sci.* **2018**. *8*, e1360.
7. Dovesi, R.; Saunders, V.; Roetti, C.; Orlando, R.; Zicovich-Wilson, C.; Pascale, F.; Civalleri, B.; Doll, K.; Harrison, N.; Bush, I.; et al. Crystal06 **2006**.
8. Arrouvel, C.; Digne, M.; Breysse, M.; Toulhoat, H.; and Raybaud, P. Effects of morphology on surface hydroxyl concentration: a DFT comparison of anatase–TiO_2 and -alumina catalytic supports. *J. Catal.* **2004**. *222*, 152 – 166.
9. Barnard, A.S. and Zapol, P. Effects of particle morphology and surface hydrogenation on the phase stability of TiO_2. *Phys. Rev. B* **2004**. *70*, 235403.
10. Barnard, A.; Zapol, P.; and Curtiss, L. Anatase and rutile surfaces with adsorbates representative of acidic and basic conditions. *Surf. Sci.* **2005**. *582*, 173 – 188. ISSN 0039-6028.
11. Barthelat, J.; Durand, P.; and Serafini, A. Non-empirical pseudopotentials for molecular calculations. *Mol. Phys.* **1977**. *33*, 159–180.
12. Berthelat, J. and Durand, P. Recent progress of pseudopotential methods in quantum chemistry. *Gazzetta Chimica Italiana* **1978**. *108*, 225–236.
13. Adamo, C. and Barone, V. Toward reliable density functional methods without adjustable parameters: The PBE0 model. *J. Chem. Phys.* **1999**. *110*, 6158–6170.
14. Grimme, S. Semiempirical GGA-type density functional constructed with a long-range dispersion correction. *J. Comput. Chem.* **2006**. *27*, 1787–1799.

15. Grimme, S.; Antony, J.; Ehrlich, S.; and Krieg, H. A consistent and accurate ab initio parametrization of density functional dispersion correction (DFT-D) for the 94 elements H-Pu. *J. Chem. Phys.* **2010**. *132*, 154104.
16. Burdett, J.K.; Hughbanks, T.; Miller, G.J.; Richardson, J.W.; and Smith, J.V. Structural-electronic relationships in inorganic solids: powder neutron diffraction studies of the rutile and anatase polymorphs of titanium dioxide at 15 and 295 K. *J. Am. Chem. Soc.* **1987**. *109*, 3639–3646.
17. Zhang, Y.f.; Lin, W.; Li, Y.; Ding, K.n.; and Li, J.q. A Theoretical Study on the Electronic Structures of TiO_2: Effect of Hartree−Fock Exchange. *J. Phys. Chem. B* **2005**. *109*, 19270–19277.
18. Labat, F.; Baranek, P.; and Adamo, C. Structural and Electronic Properties of Selected Rutile and Anatase TiO_2 Surfaces: An ab Initio Investigation. *J. Chem. Theory Comput.* **2008**. *4*, 341–352.
19. Swamy, V.; Muscat, J.; Gale, J.D.; and Harrison, N.M. Simulation of low index rutile surfaces with a transferable variable-charge Ti–O interatomic potential and comparison with ab initio results. *Surf. Sci.* **2002**. *504*, 115 – 124.
20. McGill, P. and Idriss, H. DFT study of carboxylic acids modes of adsorption on rutile TiO_2(011) surfaces. *Surf. Sci.* **2008**. *602*, 3688 – 3695.
21. Krüger, J.; Bach, U.; and Grätzel, M. Modification of TiO_2 Heterojunctions with Benzoic Acid Derivatives in Hybrid Molecular Solid-State Devices. *Adv. Mater.* **2000**. *12*, 447–451.
22. Thomas, A.G.; Jackman, M.J.; Wagstaffe, M.; Radtke, H.; Syres, K.; Adell, J.; Lévy, A.; and Martsinovich, N. Adsorption Studies of p-Aminobenzoic Acid on the Anatase TiO_2(101) Surface. *Langmuir* **2014**. *30*, 12306–12314.
23. Labat, F. and Adamo, C. Bi-isonicotinic Acid on Anatase (101): Insights from Theory. *J. Phys. Chem. C* **2007**. *111*, 15034–15042.
24. Zhu, T.; Su, J.; Alvarez, J.; Lefèvre, G.; Labat, F.; Ciofini, I.; and Pauporté, T. Response Enhancement of Self-Powered Visible-Blind UV Photodetectors by Nanostructured Heterointerface Engineering. *Adv. Func. Mater.* **2019**. *29*, 1903981.
25. Badilescu, S.; Ashrit, P.V.; and Truong, V. Enhanced infrared attenuated-total-reflection spectra of p-nitrobenzoic acid with Ag films. *Appl. Phys. Lett.* **1988**. *52*, 1551–1553.
26. Palafox, M.A.; Gil, M.; and nez, J.L.N. Spectroscopy of p-Methoxybenzoic Acid: An AM1 and ab Initio Study. *Appl. Spectrosc.* **1994**. *48*, 27–36.

27. Soo, H.; Chang, H.; Kim, H.; and Kim, K. Diffuse Reflectance Infrared Spectra of 4Nitrobenzoic Acid and 4-Cyanobenzoic Acid Self-Assembled on Fine Silver Particles. *Appl. Spectrosc.* **1998**. *52*, 1047–1052.
28. Sundaraganesan, N.; Anand, B.; Meganathan, C.; and Joshua, B.D. FT-IR, FTRaman spectra and ab initio HF, DFT vibrational analysis of p-chlorobenzoic acid. *Spectrochimica Acta Part A: Molecular and Biomolecular Spectroscopy* **2008**. *69*, 871 – 879.
29. Shao, S.; Liu, F.; Fang, G.; Zhang, B.; Xie, Z.; and Wang, L. Enhanced performances of hybrid polymer solar cells with p-methoxybenzoic acid modified zinc oxide nanoparticles as an electron acceptor. *Org. Electron.* **2011**. *12*, 641 – 647.
30. Luo, X.; Shen, J.; Zhao, X.; Wang, Z.; Wu, B.; Li, L.; Jiang, S.; and Zhou, X. Synthesis, structure and fluorescence of Er(III) complexes with benzoic acid and 4chlorobenzoic acid. *Inorganica Chim. Acta* **2016**. *446*, 169 – 175.
31. Rosado, M.T.S.; Duarte, M.L.R.; and Fausto, R. Vibrational spectra (FT-IR, Raman and MI-IR) of - and -alanine. *J. Mol. Struct.* **1997**. *410-411*, 343 – 348. ISSN 0022-2860. Molecular Spectroscopy and Molecular Structure 1996.

Chapter IV

Section 1 Context

In Chapter III, we showed that the use of CBA and NBA may help to improve the PSC performances, by adsorption of these ligands onto the TiO_2 anatase surface by using periodic DFT calculations.[1] Furthermore, experimental results show that interfacial engineering with CBA enabled us to achieve a PCE of 21.3 % to be compared to 20.3% for the untreated cells (see below and also reference).[2] However, while interfaces are well-known to play a key role in such cells, their experimental characterization at the structural and electronic levels still remains difficult. Consequently, modeling of such interfaces with appropriate computational methods is relevant for a better understanding of the basic working principles of PSC, and thus for the design of novel systems. In this chapter, we present the results obtained on the cubic and tetragonal phases of bulk MAPI with different DFT models. Then, we tackle the modeling of the MAPI/CBA/TiO_2 heterostructure, using a model of the interface.

The calculations performed on MAPI aim to better understand the overall properties of this system. The interface calculations on the other hand allow to show that the linking of the perovskite and TiO_2 moieties is enhanced by using the bifunctional CBA ligand. A model of the MAPI/CBA/TiO_2 interface (**Figure 4.1.1**) has been built and its structural and electronic properties have been fully characterized at the periodic hybrid DFT level. The key electron injection process found at this interface has also been addressed. We show that ligand can be efficiently used for surface engineering of the heterointerface found in PSC between MAPI and TiO_2, due its bifunctional nature, acting both as a suitable spacer at the interface to improve its stability, but also imposing a favorable dipole moment to improve band alignment and thus electron injection in such systems.

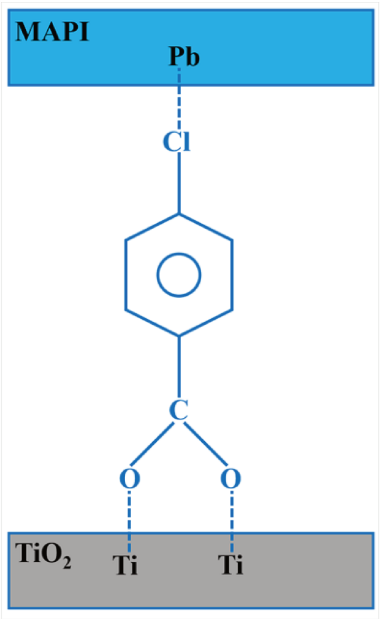

Figure 4.1.1: Schematic of the MAPI/CBA/TiO_2 interface.

Section 2 Computational Details

All calculations were carried out with the periodic Crystal17 code, which is based on a linear combination of atom-centered Gaussian orbitals and solves self-consistently both Hartree-Fock (HF) and Kohn-Sham equations.[3-4] When considering the MAPI bulk system, different functionals with and without dispersion were tested. For the heterointerface structure however, only the global hybrid PBE0 functional, containing 25% of HF exchange[5], has been considered. Previous studies have shown that this functional can indeed provide reliable geometric and electronic properties of both TiO_2[6] and MAPI[7], that are the two building blocks of the interface targeted. Additional dispersion effects were accounted for through the empirical D3 correction.[8] All-electron basis sets have been used for the CBA ligand and the methylammonium (MA^+) moieties. More precisely, for MA atoms, (31/1) contractions were used for H, while (631/31/1) contractions were employed for both C and N atoms. For CBA atoms, (511/1), (621/21/1), (7311/311/1), (8411/411/1) and (86311/6311) contractions were considered for H, C, N, O and Cl atoms, respectively. On the other hand, pseudopotentials were considered for all the other atoms. For Ti and O of TiO_2, Durand and Barthelat large-core pseudopotentials with associated (1/1/41) and (31/31) contractions corresponding to 4 and 6 explicit electrons, respectively, were chosen.[9-10] Finally, for Pb and I, small core fully relativistic pseudopotentials developed at the Stuttgart University were selected, with 22 explicit electrons described using a (8811/1188/611/1) contraction scheme for Pb, and 25 explicit electrons described using a (8811/661/61) contraction scheme for I.[11]

For cubic and tetragonal bulk MAPI, reciprocal space was sampled using a shrinking factor of 12 and three shrinking factors (9, 9, 6), respectively. For MAPI/CBA/TiO_2 heterostructure, reciprocal space was sampled using a shrinking factor of 2, corresponding to 4 **k** points in the irreducible Brillouin zone. Numerical DFT integration was performed considering 99 radial points and 1454 angular points, ensuring an error on the integrated electron density lower than 10^{-5} |e-| per unit cell. The Coulomb and exchange series were truncated with threshold values of 10^{-7}, 10^{-7}, 10^{-7}, 10^{-9}, and 10^{-27}.

Cell parameters of the lattice as well as atomic positions of a selected fragment of atoms (see below) were relaxed during geometry optimizations. Convergence was determined from the root-mean-square and absolute value of the largest component of the forces and displacements, considering default values.[12]

Interface formation was energetically characterized by considering two quantities:

- adhesion energy, which is the energy gained by forming the interface, computed as:

$$E_{ads} = E(\text{MAPI/CBA}) + E(TiO_2) - E(\text{MAPI/CBA/}TiO_2) \quad (4.2.1)$$

where E(MAPI/CBA) and $E(TiO_2)$ are the total energies of the optimized MAPI/CBA slab and TiO_2 supercell slab models, respectively, and E(MAPI/CBA/TiO_2) is the total energy of the MAPI/CBA/TiO_2 interface

- specific adhesion energy, which is the adhesion energy per unit surface area, calculated as:

$$\beta_{ads} = E_{ads}/S \quad (4.2.2)$$

where S is the surface area of the MAPI/CBA/TiO_2 interface model.[13]

The electron injection time was evaluated by considering a simplified orbital-based model derived from the original Newns-Anderson proposal for adsorbates on surfaces,[14] which was already successfully applied to dye-sensitized solar cells.[15-16] In this approach, the ability of the calculated energy broadenings to capture essential features of the electronic coupling, in the wide band limit of heterogeneous electron-transfer encountered here, is considered by using the calculated PDOS broadenings as an effective measure of an electronic coupling strength that can be converted to an electron-transfer time.[17] Thus, only the evaluation of the broadening (Δ, in meV) of the donor level of the perovskite sensitizer when it is adsorbed on the TiO_2 surface is required to compute the injection time (τ, in fs) according to:

$$\tau = 658/\Delta \quad (4.2.3)$$

Section 3 Bulk $MAPbI_3$

We first relaxed both cubic and tetragonal MAPI with different DFT functionals,

with or without additional dispersion corrections. As listed in **Table 4.3.1**, when considering dispersion, the lattice parameters shrink and the bandgap decreases for both phases. Compared to the experimental values, PBE with dispersion seems to be the best performing functional, but this is due to fortuitous error cancellations. While PBE is known to underestimate the bandgap of semiconductors,[18-19] the calculation was done without considering spin-orbit coupling (SOC), whose effect has already been quantified in such systems and leads to a decrease of the bandgap of about 1.1 eV.[7] Thus, PBE-D2 is not the most suitable choice once the SOC is considered. Here, we find that the bandgap value derived from PBE0-D2 is close to the experimental data when corrected by 1.1 eV. Although B3PW-D2 gives a very close description, the structure optimized at this level is not as good as the one obtained at the PBE-D2 level. We also note that the results derived from PBE0-D3 give only small differences compared with that from PBE0-D2. In the following, for the heterointerface modeling, the PBE0-D3 functional has been selected.

Table 4.3.1: Calculated lattice parameters (Å) and bandgaps (eV) of cubic and tetragonal MAPI with different DFT models.

MAPI	Cubic			Tetragonal			
Functional	*a*	Bandgap	Corrected Bandgap*1	*a*	*c*	Bandgap	Corrected Bandgap*1
PBE0	6.400	2.81	1.71	8.937	12.797	2.97	1.87
PBE0-D2	6.284	2.58	1.48	8.768	12.555	2.81	1.71
PBE0-D3	-	-		8.761	12.544	2.76	1.66
PBE	6.437	1.78	0.68	8.988	12.869	1.92	1.81
PBE-D2	6.287	1.55	0.45	8.772	12.559	1.76	0.66
B3PW	6.444	2.65	1.55	8.994	12.878	2.79	1.69
B3PW-D2	6.231	2.25	1.15	8.695	12.450	2.52	1.42
Exp*2	6.325	1.63	1.63	8.856	12.659	1.70	1.70

*1: A 1.1 eV correction is applied to the computed DFT band gap value to take into account the SOC effect.

*2: Experimental data: from Ref. [7, 21-22]

We then calculated the band structures of both cubic and tetragonal MAPI using PBE0-D2, as shown in **Figure 4.3.1**. The path in the Brillouin zone of tetragonal MAPI was chosen according to a previous work.[20] It can be seen that both phases have a direct band gap, which may be potential beneficial for PSC application.

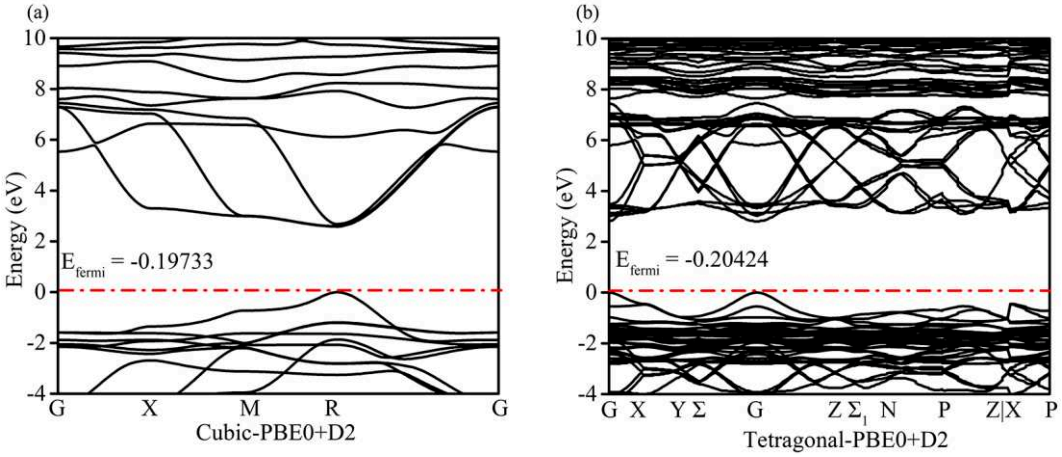

Figure 4.3.1: Bandstructure of (a) cubic and (b) tetragonal MAPI.

Section 4 Heterointerface

In this section, the results about the heterointerface between MAPI and TiO_2 with CBA playing the role of bridge ligand are given. In particular, MAPI is the tetragonal one as it is the common phase at room temperature.

The works devoted to the investigation of isolated MAPI are numerous. For example, Yoshitaka et al. recently investigated the structural stability and the electronic structures of a series of low-indices surfaces of tetragonal MAPI, highlighting that the (110) and (001) terminations are expected to be stable, with shallow surface states that can act as efficient intermediates for hole transport to HTL.[23-24] The tetragonal MAPI (001) surface was also recently investigated, comparing the two possible MAI and PbI_2 terminations, indicating that the MAI termination is relatively more favorable than the PbI_2 one in equilibrium growth.[25] As for the works devoted to the modeling of the full MAPI/TiO_2 interface,[26-31] De Angelis[28] et al. proposed the (110) surface of MAPI to preferentially grow on TiO_2 due to better lattice matching, with the chloride atoms concentrating at the TiO_2 interface.[29] Based on these reports, we chose (110) surface of MAPI with PbI_2 terminations as our building block. Furthermore, experimental data already proved that the use of CBA can help to improve the PCE of the cell device, as listed in **Table 4.4.1** and **4.4.2**.[2] Thus, our simulation focused on the CBA modified

MAPI/TiO_2 interface.

Table 4.4.1: Photovoltaic *J-V* parameters of our best perovskite solar cells, with and without an interfacial engineering by a CBA ligand.

Cell	Scan direction	V_{OC} / V	J_{SC} / mA.cm^{-2}	*FF* / %	*PCE* / %
CBA	Reverse	1.101	24.25	79.81	21.35
	Forward	1.086	24.26	70.59	18.60
Blank	Reverse	1.110	23.29	78.53	20.30
	Forward	1.105	23.27	73.81	18.97

Table 4.4.2: Averaged photovoltaic reverse scan *J-V* parameters and PCE with standard deviation of our perovskite solar cells, with and without an interfacial engineering by a CBA ligand.

Cell	V_{oc} /V	J_{sc} / mA.cm^{-2}	*FF* /%	*PCE* /%
CBA	1.094±0.016	24.00±0.29	79.26±0.65	20.57±0.88
Blank	1.083±0.027	23.09±0.24	79.07±1.47	19.34±0.96

The models

A MAPI/CBA/TiO_2 interface was built starting from converged surface models of its two building blocks: the TiO_2 oxide and the MAPI perovskite. A (2x2) supercell model of the anatase TiO_2-(101) surface with 8 layers, corresponding to 8 O-Ti-O trilayers with 96 atoms and lattice parameters a=14.981 Å, b=11.088 Å and γ=109.7° was selected for the oxide part. For MAPI, although both MAI- and PbI_2-terminated (110) surfaces can exist, the former is known to be stable[24] and is expected to more easily bind to the TiO_2 surface than the latter. A 3-PbI_2 layers (110) slab was therefore obtained from the tetragonal MAPI bulk system with space group I_4/mcm, resulting in a 2D lattice with lattice parameters a, b and γ of 12.343 Å, 12.555 Å and 90.0°, respectively. Consequently, a large mismatch between the lattice parameters of the 2D lattices of the TiO_2 and MAPI slabs was obtained. The bifunctional nature of the CBA ligand was exploited by considering its carboxylate part to bind to TiO_2 in a bridging bidentate mode, while its Cl atom was oriented towards the Pb atoms of MAPI close to the TiO_2 substrate. By substituting all I^- of the last layer of the MAPI surface with Cl atoms, Pb-Cl bonds were then created and the charge neutrality of the resulting unit cell

was ensured by removing all H^+ of the last layer of MA moieties of MAPI. The final interface model was obtained by modifying the MAPI slab lattice to the values of the TiO_2 supercell, resulting in an interface model with P1 symmetry, 328 atoms and 3876 atomic orbitals per unit cell. The lattice was then fully-relaxed, and all atoms but the lower 6 bottom layers of the TiO_2 substrate were allowed to relax. In addition, to more clearly highlight the role of the TiO_2 substrate in the MAPI/CBA/TiO_2 interface, and especially on its electronic properties, we also considered adsorption of CBA on a MAI-terminated MAPI (110) slab with 3-PbI_2 layers, considering a 1:1 substitution ratio between I^- and Cl atoms. We note here that the CH_3NH_2 layer formed in contact with the CBA ligands is relevant for PSC application, since the $CH_3NH_3^+$ ion in MAPI is well-known to readily deprotonate in the presence of water. In addition, chlorine atoms have already been shown to tend to concentrate at the TiO_2 interface.[30] **Figures 4.4.1(a)** and **4.4.1(b)** present resulting structures of both models after geometry optimization.

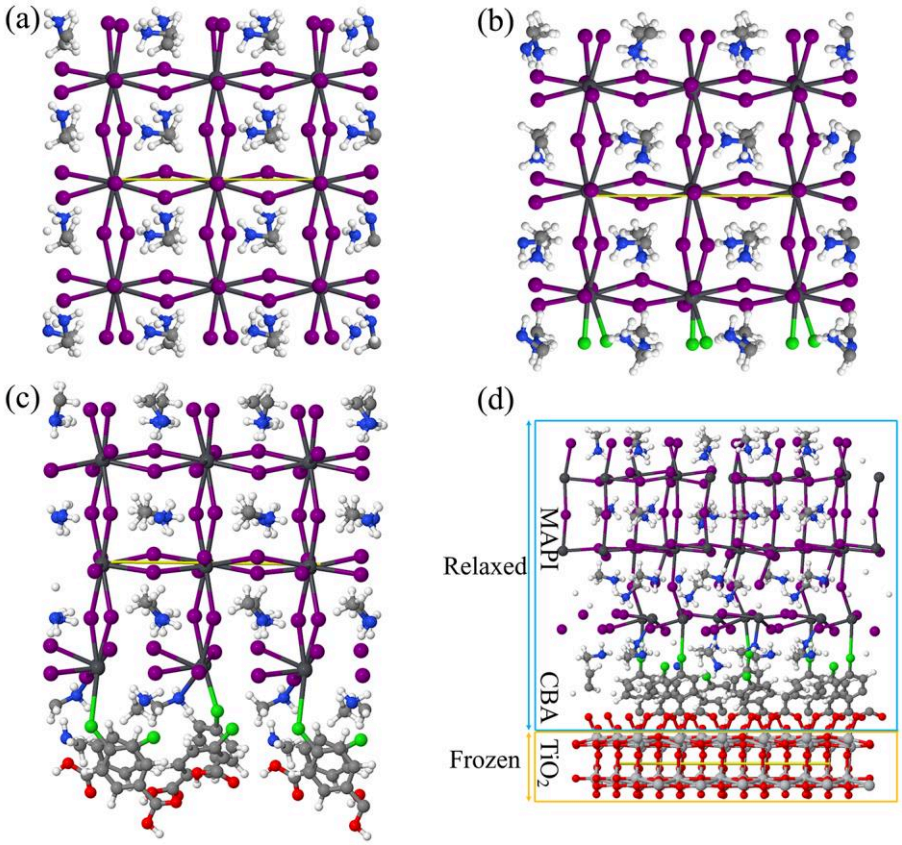

Figure 4.4.1: Ball and stick representation of the (a) MAPI(110) surface, (b) the MAPI-slab with all iodide atoms on one surface replaced by chloride atoms, (c) MAPI/CBA unit cell and (d) MAPI/CBA/TiO_2 interface unit cell. The solid yellow line represents the unit cell. Red, light grey, white, green, purple, dark grey, blue and grey spheres correspond to O, Ti, H, Cl, I, Pb, N and C atoms, respectively. The relaxed and frozen parts considered for the geometry optimization of the MAPI/CBA/TiO_2 interface are indicated in Figure 4.4.1(d).

Structural and energetic features

Table 4.4.3 summarizes the main structural features of the optimized lattices of the different building blocks and interface models considered, while **Table 4.4.4** reports selected resulting distances.

Table 4.4.3: Lattice parameters *a*, *b* (in Å) and *γ* (in degrees) as well as computed band gaps (E_g, in eV) for selected systems involved in the interface model construction. Adhesion energy (E_{adh}, in eV) and specific adhesion energy (β, in eV·Å^{-2}) of the MAPI/CBA/TiO_2 interface are also given.

	MAPI (110)	CBA/MAPI (110)	TiO_2 (101)	MAPI (110)/CBA/TiO_2 (101)
a	12.343	12.343	14.981	14.821
b	12.555	12.555	11.088	11.003
γ	90.00	90.00	109.74	108.03
E_g	2.97	3.39	5.03	2.16
E_{adh}	--	--	--	3.45
β	--	--	--	0.02

Table 4.4.4: Selected distances (in Å) between Pb, N and Cl atoms of the MAPI/CBA and MAPI/CBA/TiO_2 systems.

	$d_{N/Pb}$				$d_{Cl/Pb}$				$d_{Ti/O}$	
MAPI/CBA	3.358	3.710	4.032	5.472	2.627	2.632	4.749	5.566	-	-
MAPI/CBA/TiO_2	3.457	3.957	4.686	5.424	2.517	2.553	5.063	5.669	2.176	2.100

The optimized *a* and *b* cell parameters of the MAPI/CBA/TiO_2 interface model are close to those of the TiO_2 supercell considered, with values of 14.821 Å and 11.003 Å, together with a *γ* angle of 108.0°. Compared to the TiO_2 supercell lattice, a small shrinking of all lattice parameters is therefore obtained when going from the TiO_2 supercell to the MAPI/CBA/TiO_2 interface, with shrinking values of -1.07, -0.77 and -1.55 %, respectively for the *a*, *b* and *γ* parameters. From the data reported in **Table 4.4.4**, both Ti-O and Pb-Cl bonds can be evidenced, the CBA ligand acting with two

complementary features to ensure interface stability between the perovskite and the oxide. The first feature corresponds to its bifunctional linker nature: a bridging bidentate mode is involved between the CBA carboxylate moiety and TiO_2, while strongly distorted PbI_5Cl octohedra can be evidenced between MAPI and CBA. Here, we note that Pb atoms both interact with Cl atoms and the deprotonated $CH_3NH_3^+$ groups in the layer in contact with CBA. The same conclusion can be drawn in the MAPI/CBA case. The second feature is the ability of CBA ligands to lay on the TiO_2 substrate, with computed tilting angles with respect to the surface normal of 30.0, 38.6, 38.6 and 46.9° for the four CBA molecules of the MAPI/CBA/TiO_2 interface model unit cell for instance. In particular, favorable H^+/π interactions between the dissociated H^+ of the carboxylate groups of CBA adsorbed on the TiO_2 substrate and the benzene ring of the CBA ligands tend to further improve interface stability by building a favorably organized CBA-TiO_2 interface for the binding of MAPI. This can be related to the rigid nature of the CBA ligand. The computed adhesion energy of the MAPI/CBA/TiO_2 model further confirms these conclusions, with a computed value of 3.45 eV, corresponding to a specific adhesion energy of 0.02 eV/Å^2, indicating a stable interface formation. We note that this value is in line with the 0.04 eV/Å^2 value recently reported by Mosconi et al. for a similar interface based on the same surface orientations,[29] as well with those obtained with other orientations.[31]

Electronic properties

Figure 4.4.2 presents the computed band structures, as well as the total and projected density of states (TDOS and PDOS) of the MAPI/CBA/TiO_2 and MAPI/CBA interfaces.

For MAPI/CBA, band dispersion can be noticed at the top of the valence band (VB) and at the bottom of the conduction band (CB). This can be related to the interaction of the CBA ligand with MAPI through its Cl atoms. In addition, the top of the VB and the bottom of the CB are mainly composed by the MAPI perovskite in which I^- has been substituted with Cl in a 1:1 ratio. Compared to the clean MAPI (110) surface therefore, this leads to a band gap increase from 2.97 to 3.39 eV. When considering the MAPI/CBA/TiO_2 interface on the other hand, the band gap decreases to 2.16 eV mainly due to the TiO_2 contribution at the bottom of the CB. In fact, the band structure and DOS analysis of the MAPI/CBA/TiO_2 interface reveals that the top of the VB is mainly due to MAPI while the bottom of the CB is mainly due to TiO_2, suggesting

a possible electron transfer from the perovskite to the oxide from an energetic viewpoint, which is in line with the working principles of PSC mentioned above. Furthermore, it should be noted that the CBA ligand does not contribute to the valence or conduction bands close to the band gap region. Here, we note that no spin-orbit coupling effects have been taken into account in these calculations, but these have previously been quantified and shown to further reduce the above-mentioned band gap values of about 1.1 eV.[7]

Furthermore, both band structures present direct band gaps at Γ, highlighting a possible favorable and efficient photoexcitation of the heterointerface.

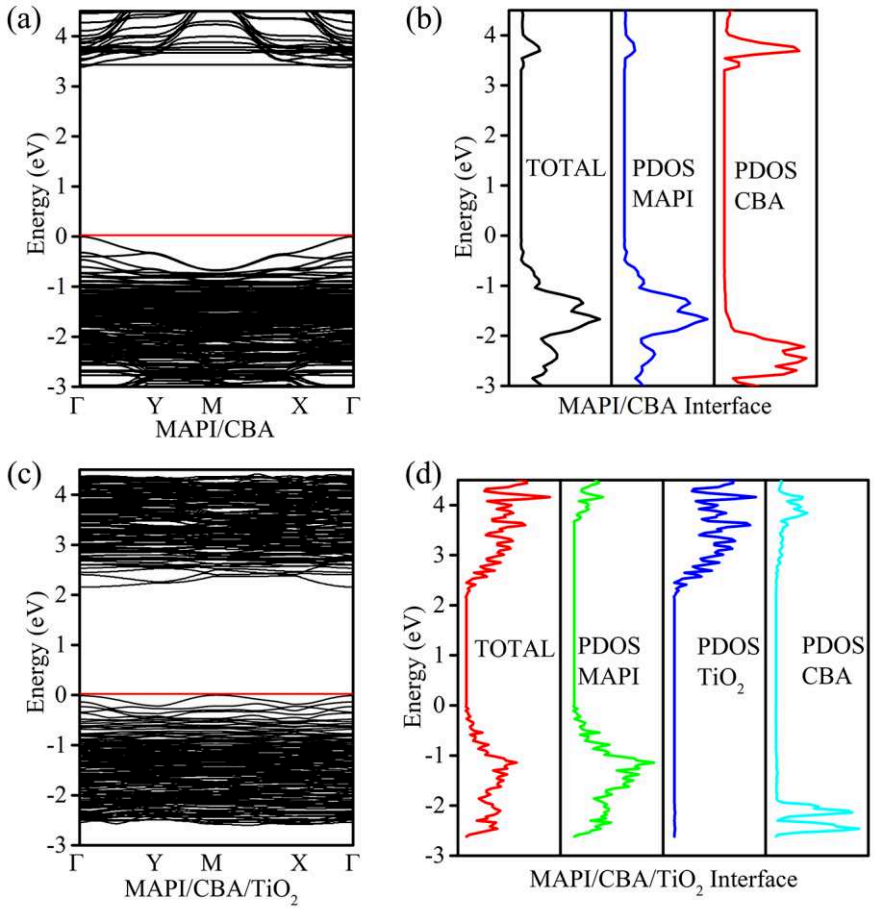

Figure 4.4.2: (left) Band structure and (right) total and projected density of states (TDOS and PDOS) of the (top) MAPI/CBA and (bottom) MAPI/CBA/TiO_2 interfaces. **k**-points used for the band structure are: Γ (0, 0, 0), Y (0, 1/2, 0), M (1/2, 1/2, 0) and X (1/2, 0, 0).

From the values reported in **Table 4.4.5**, for CBA/TiO_2, the positive value suggests a charge transfer to the TiO_2 surface.[1] As for MAPI/CBA, the value of the dipole moment pointing towards MAPI in the chemistry notation is negative, indicating that CBA may block electron reflow to MAPI. Furthermore, it can be noticed that a positive value is also obtained for MAPI/CBA/TiO_2, thus highlighting that CBA can potentially enhance the electron transfer from MAPI to TiO_2.

Table 4.4.5: Dipole moments components along the surface normals (μ_z, in Debye) of the CBA/TiO_2, MAPI/CBA and MAPI/CBA/TiO_2 systems.

Systems	μ_z
CBA/TiO_2	0.89
MAPI/CBA	-0.88
MAPI/CBA/TiO_2	0.61

To better clarify this point, electron injection from MAPI to TiO_2 has been analyzed using an approach that we have developed notably for dye-sensitized solar cells[32-33] and quantum-dot sensitized solar cells[34]. More precisely, the spin density of the reduced MAPI/CBA/TiO_2 system has been computed and the corresponding isodensity plot is shown in **Figure 4.4.3**. It is clear that the computed spin density is mainly delocalized over the TiO_2 part, with a 99.94% contribution of the added electron on the TiO_2 substrate. This value is a quantification of the injection efficiency of the photogenerated electrons and indicates an almost quantitative electron transfer from MAPI to TiO_2 through the CBA ligand.

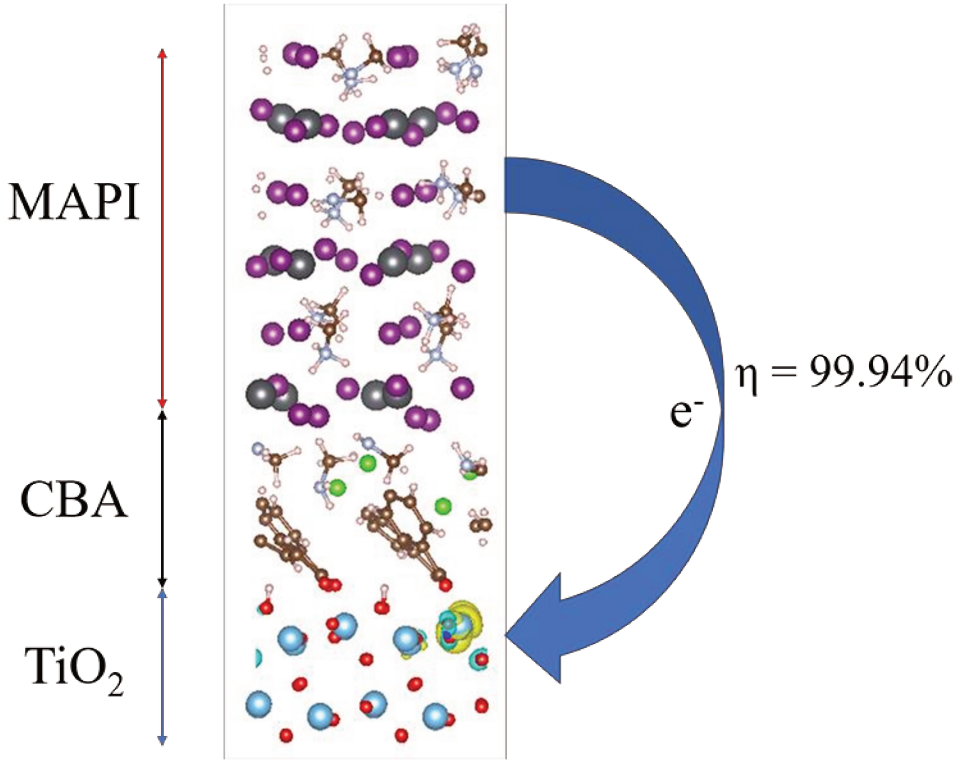

Figure 4.4.3: Spin density of the reduced MAPI/CBA/TiO_2 interface system (excess of alpha electron is indicated in yellow), isosurface contour value: |0.00271| a.u.

Finally, based on the Newns-Anderson model and the computed electronic structure of the MAPI/CBA/TiO_2 system, the electron injection time is estimated to be 24 fs, indicating an ultrafast electron injection. This result is in good agreement with a

previously-reported estimate based on a coupling matrix elements approach for the bare MAPI/TiO_2 interface[35] where an injection in the femtosecond time scale has been obtained. We note that controversial experimental results are available regarding the electron injection time with values reported both in the picosecond[36] or sub-picosecond[37-38] timescales, preventing a more rigorous comparison between experimental and computed data.

Section 5 Conclusion

In this chapter, a periodic hybrid density functional theory computational strategy has been presented to model the cubic and tetragonal phases of the MAPI perovskite, and the heterointerface between the MAPI perovskite and TiO_2, as found in PSC, in which the CBA ligand has been used to improve the stability and the band alignment at the interface.

The modeling of bulk MAPI revealed that different DFT models with additional dispersion effects can influence the results obtained. In particular, while PBE0 with dispersion and B3PW without dispersion can both reproduce the experimental bandgap, PBE0 with dispersion can also give an accurate simulation of lattice parameters. The computed band structures at the PBE0-D2 level indicates that both cubic and tetragonal MAPI are direct band semiconductors.

For the modeling of heterointerface, the CBA ligand has been selected to act as a bifunctional linker to efficiently link the perovskite and the oxide moieties, ensuring stability of the interface through Ti-O and Pb-Cl interactions. The computed density of states revealed that the perovskite contributes to the top of the valence band while the oxide contributes to the bottom of the conduction band with a direct bandgap of 2.16 eV, indicating a possible electron transfer from MAPI to TiO_2. Dipole moment analysis additionally revealed that the CBA ligand can induce a favorable effect to improve band alignment and thus electron transfer from MAPI to TiO_2. This latter has been quantified by calculation of the spin density of the reduced MAPI/CBA/TiO_2 system and indicated an almost quantitative electron transfer from MAPI to TiO_2 for the surface engineered system, together with an ultrafast injection time in the femtosecond timescale. Overall, the proposed DFT-based computational protocol therefore indicated that by surface engineering with a bifunctional linker such as CBA, a better stability, together with improved band alignment and electron injection, could be obtained for PSC systems. Work is in progress to design novel PSC systems with enhanced efficiency based on these guidelines.

References

1. Zhu, T.; Su, J.; Alvarez, J.; Lefèvre, G.; Labat, F.; Ciofini, I.; and Pauporté, T. Response Enhancement of Self-Powered Visible-Blind UV Photodetectors by Nanostructured Heterointerface Engineering. *Adv. Func. Mater.* **2019**. *29*, 1903981.
2. Zhu, T.; Su, J.; Labat, F.; Ciofini, I.; and Pauporté, T. Interfacial Engineering through Chloride-Functionalized Self-Assembled Monolayers for High-Performance Perovskite Solar Cells. *ACS Appl. Mater. Inter.* **2020**. *12*, 744–752.
3. Dovesi, R.; Erba, A.; Orlando, R.; Zicovich-Wilson, C.M.; Civalleri, B.; Maschio, L.; Rérat, M.; Casassa, S.; Baima, J.; Salustro, S.; and Kirtman, B. Quantum-mechanical condensed matter simulations with CRYSTAL. *WIREs Comput. Mol. Sci.* **2018**. *8*, e1360.
4. Dovesi, R.; Saunders, V.; Roetti, C.; Orlando, R.; Zicovich-Wilson, C.; Pascale, F.; Civalleri, B.; Doll, K.; Harrison, N.; Bush, I.; et al. Crystal06 **2006**.
5. Adamo, C. and Barone, V. Toward reliable density functional methods without adjustable parameters: The PBE0 model. *J. Chem. Phys.* **1999**. *110*, 6158–6170.
6. Labat, F.; Baranek, P.; Domain, C.; Minot, C.; and Adamo, C. Density functional theory analysis of the structural and electronic properties of TiO_2 rutile and anatase polytypes: Performances of different exchange-correlation functionals. *J. Chem. Phys.* **2007**. *126*, 154703.
7. Melissen, S.T.A.G.; Labat, F.; Sautet, P.; and Le Bahers, T. Electronic properties of $PbX_3CH_3NH_3$ (X = Cl, Br, I) compounds for photovoltaic and photocatalytic applications. *Phys. Chem. Chem. Phys.* **2015**. *17*, 2199–2209.
8. Grimme, S. Semiempirical GGA-type density functional constructed with a long-range dispersion correction. *J.Comput. Chem.* **2006**. *27*, 1787–1799.
9. Berthelat, J. and Durand, P. Recent progress of pseudopotential methods in quantum chemistry. *Gazzetta Chimica Italiana* **1978**. *108*, 225–236.
10. Barthelat, J.; Durand, P.; and Serafini, A. Non-empirical pseudopotentials for molecular calculations. *Mol. Phys.* **1977**. *33*, 159–180.

11. Metz, B.; Stoll, H.; and Dolg, M. Small-core multiconfiguration-Dirac–Hartree–Fockadjusted pseudopotentials for post-d main group elements: Application to PbH and PbO. *J. Chem. Phys.* **2000**. *113*, 2563–2569.
12. Erba, A.; Baima, J.; Bush, I.; Orlando, R.; and Dovesi, R. Large-Scale Condensed Matter DFT Simulations: Performance and Capabilities of the CRYSTAL Code. *J. Chem. Theory Comput.* **2017**. *13*, 5019–5027.
13. Ricca, C.; Ringuedé, A.; Cassir, M.; Adamo, C.; and Labat, F. On the Stability Issues of TiO_2-Based Composites in View of Fuel Cell Application: A Combined Experimental and Theoretical Investigation. *J. Phys. Chem. C* **2019**. *123*, 12573–12582.
14. NEWNS, D.M. Self-Consistent Model of Hydrogen Chemisorption. *Phys. Rev.* **1969**. *178*, 1123–1135.
15. Labat, F.; Le Bahers, T.; Ciofini, I.; and Adamo, C. First-Principles Modeling of Dye-Sensitized Solar Cells: Challenges and Perspectives. *Acc. Chem. Res.* **2012**. *45*, 1268–1277.
16. Labat, F.; Ciofini, I.; and Adamo, C. Revisiting the importance of dye binding mode in dye-sensitized solar cells: a periodic viewpoint. *J. Mater. Chem.* **2012**. *22*, 12205–12211.
17. Persson, P.; Lundqvist, M.J.; Ernstorfer, R.; Goddard, W.A.; and Willig, F. Quantum Chemical Calculations of the Influence of Anchor-Cum-Spacer Groups on Femtosecond Electron Transfer Times in Dye-Sensitized Semiconductor Nanocrystals. *J. Chem. Theory Comput.* **2006**. *2*, 441–451.
18. Le Bahers, T.; Rérat, M.; and Sautet, P. Semiconductors Used in Photovoltaic and Photocatalytic Devices: Assessing Fundamental Properties from DFT. *J. Phys. Chem. C* **2014**. *118*, 5997–6008.
19. Heyd, J. and Scuseria, G.E. Efficient hybrid density functional calculations in solids: Assessment of the Heyd–Scuseria–Ernzerhof screened Coulomb hybrid functional. *J. Chem. Phys.* **2004**. *121*, 1187–1192.
20. Setyawan, W. and Curtarolo, S. High-throughput electronic band structure calculations: Challenges and tools. *Comput. Mater. Sci.* **2010**. *49*, 299 – 312.

21. Poglitsch, A. and Weber, D. Dynamic disorder in methylammoniumtrihalogenoplumbates (II) observed by millimeter-wave spectroscopy. *J. Chem. Phys.* **1987**. *87*, 6373–6378.
22. Papavassiliou, G. and Koutselas, I. Structural, optical and related properties of some natural three- and lower-dimensional semiconductor systems. *Synth. Met.* **1995**. *71*, 1713 – 1714. ISSN 0379-6779. Proceedings of the International Conference on Science and Technology of Synthetic Metals (ICSM '94).
23. Haruyama, J.; Sodeyama, K.; Han, L.; and Tateyama, Y. Surface Properties of CH3NH3PbI3 for Perovskite Solar Cells. *Acc. Chem. Res.* **2016**. *49*, 554–561.
24. Haruyama, J.; Sodeyama, K.; Han, L.; and Tateyama, Y. Termination Dependence of Tetragonal $CH_3NH_3PbI_3$ Surfaces for Perovskite Solar Cells. *J. Phys. Chem. Lett.* **2014**. *5*, 2903–2909.
25. Teng, Q.; Shi, T.T.; Tian, R.Y.; Yang, X.B.; and Zhao, Y.J. Role of organic cations on hybrid halide perovskite $CH_3NH_3PbI_3$ surfaces. *J. Solid State Chem.* **2018**. *258*, 488 – 494.
26. Roiati, V.; Mosconi, E.; Listorti, A.; Colella, S.; Gigli, G.; and De Angelis, F. Stark Effect in Perovskite/TiO_2 Solar Cells: Evidence of Local Interfacial Order. *Nano Lett.* **2014**. *14*, 2168–2174.
27. De Angelis, F. Modeling Materials and Processes in Hybrid/Organic Photovoltaics: From Dye-Sensitized to Perovskite Solar Cells. *Acc. Chem. Res.* **2014**. *47*, 3349–3360.
28. Mosconi, E.; Grancini, G.; Roldán-Carmona, C.; Gratia, P.; Zimmermann, I.; Nazeeruddin, M.K.; and De Angelis, F. Enhanced TiO_2/$MAPbI_3$ Electronic Coupling by Interface Modification with PbI_2. *Chem. Mater.* **2016**. *28*, 3612–3615.
29. Mosconi, E.; Ronca, E.; and De Angelis, F. First-Principles Investigation of the TiO_2/Organohalide Perovskites Interface: The Role of Interfacial Chlorine. *J. Phys. Chem. Lett.* **2014**. *5*, 2619–2625.
30. Colella, S.; Mosconi, E.; Pellegrino, G.; Alberti, A.; Guerra, V.L.P.; Masi, S.; Listorti, A.; Rizzo, A.; Condorelli, G.G.; De Angelis, F.; and Gigli, G. Elusive

Presence of Chloride in Mixed Halide Perovskite Solar Cells. *J. Phys. Chem. Lett.* **2014**. *5*, 3532–3538.

31. Geng, W.; Tong, C.J.; Liu, J.; Zhu, W.; Lau, W.M.; and Liu, L.M. Structures and electronic properties of different $CH_3NH_3PbI_3/TiO_2$ interface: a first-principles study. *Sci. Rep.* **2016**. *6*, 20131.
32. Le Bahers, T.; Pauporté, T.; Lainé, P.P.; Labat, F.; Adamo, C.; and Ciofini, I. Modeling Dye-Sensitized Solar Cells: From Theory to Experiment. *J. Phys. Chem. Lett.* **2013**. *4*, 1044–1050.
33. Le Bahers, T.; Labat, F.; Pauporté, T.; Lainé, P.P.; and Ciofini, I. Theoretical Procedure for Optimizing Dye-Sensitized Solar Cells: From Electronic Structure to Photovoltaic Efficiency. J. Am. Chem. Soc. **2011**. *133*, 8005–8013.
34. Szemjonov, A.; Pauporté, T.; Ithurria, S.; Pedetti, S.; Lequeux, N.; Dubertret, B.; Ciofini, I.; and Labat, F. Towards the modeling of quantum-dot sensitized solar cells: from structural and vibrational features to electron injection through latticemismatched interfaces. *J. Mater. Chem. A* **2016**. *4*, 13081–13092.
35. Haruyama, J.; Sodeyama, K.; Hamada, I.; Han, L.; and Tateyama, Y. First-Principles Study of Electron Injection and Defects at the $TiO_2/CH_3NH_3PbI_3$ Interface of Perovskite Solar Cells. *J. Phys. Chem. Lett.* **2017**. *8*, 5840–5847.
36. Marchioro, A.; Brauer, J.C.; Teuscher, J.; Grätzel, M.; and Moser, J.E. Photoinduced processes in lead iodide perovskite solid-state solar cells. In N. Banerji and C. Silva, editors, *Physical Chemistry of Interfaces and Nanomaterials XII*, volume 8811. International Society for Optics and Photonics, SPIE, 20 – 25.
37. Ponseca, C.S.; Savenije, T.J.; Abdellah, M.; Zheng, K.; Yartsev, A.; Pascher, T.; Harlang, T.; Chabera, P.; Pullerits, T.; Stepanov, A.; Wolf, J.P.; and Sundström, V. Organometal Halide Perovskite Solar Cell Materials Rationalized: Ultrafast Charge Generation, High and Microsecond-Long Balanced Mobilities, and Slow Recombination. *J. Am. Chem. Soc.* **2014**. *136*, 5189–5192.
38. Ponseca Jr., C.S. and Sundström, V. Revealing the ultrafast charge carrier dynamics in organo metal halide perovskite solar cell materials using time resolved THz spectroscopy. *Nanoscale* **2016**. *8*, 6249–6257.

Chapter V

Section 1 Context

Despite the advantages discussed in the above chapters, MAPI, the perovskite material playing the role of light absorbing layer, still presents some major obstacles for practical application such as poor near infrared absorption[1] and easy decomposition under humidity[2]. Other perovskite candidates are therefore necessary to be considered. Among them, formamidinium lead iodide (FAPI) can potentially provide better optoelectronic performances due to its more suitable bandgap[3] and corresponding broad absorption of the solar spectrum[4]. Unfortunately, its α-phase which is suitable for the PV application[5] is also not stable in a humid ambient atmosphere[6]. To stabilize it, the commonly used strategy is the incorporation of cations such as K^+, Cs^+, and Rb^+.[7-8] Furthermore, the incorporation of other organic cations (for example MA^+) can achieve the same effects[9-10]. For example, a recent report on methylenediammonium (MDA) doped FAPI system by Sang Il Seok et. al. shows that with certified PCEs of 23.7%, more than 90% of the initial efficiency was maintained after 600 hours of operation with maximum power point tracking under full sunlight illumination in ambient conditions including ultraviolet light[11]. To better understand the mechanisms at play, one needs to shed light on the basic component materials of the PSC device. In this case, the properties of α-FAPI are crucial and DFT calculations can give insights on such systems.[12] Here, we present modeling of the pure α-phase bulk FAPI as well as of two of its most-stable surfaces. Although this is a preliminary investigation carried out on the pure system, it can give some insights on the structure/properties relationship of α-FAPI and serve as a reference to better understand the stabilizing mechanisms involved when cation incorporation will be considered in future works.

This chapter is organized as follows: after a description of the computational details, the calculations on pure α-phase bulk FAPI are first given. Then, the results on stoichiometric and nonstoichiometric α-FAPI surfaces are shown. Finally, conclusions are given.

Section 2 Computational Details

All calculations were carried out with the periodic Crystal17 code. When considering FAPI bulk system, different functionals with and without dispersion were

tested. For the modeling of FAPI surfaces, exchange and correlation energies were described using the global hybrid PBE0 functional, containing 25% of HF exchange[13]. Additional dispersion effects were accounted for through the empirical D3 correction[14]. All-electron basis sets have been used for the formamidinium FA^+ $(NH_2CHNH_2)^+$ moieties. More precisely, for FA^+ atoms, (31/1) contractions were used for H, while (631/31/1) contractions were employed for both C and N atoms. On the other hand, pseudopotentials were considered for Pb and I atoms by choosing small core fully relativistic pseudopotentials developed at the Stuttgart University, with 22 explicit electrons described using a (8811/1188/611/1) contraction scheme for Pb, and 25 explicit electrons described using a (8811/661/61) contraction scheme for I[15]. Reciprocal space was sampled using a shrinking factor of 10. Numerical DFT integration was performed considering 75 radial points and 974 angular points, ensuring an error on the integrated electron density lower than 10^{-5} $|e^-|$ per unit cell. The Coulomb and exchange series were truncated with threshold values of 10^{-7}, 10^{-7}, 10^{-7}, 10^{-9}, and 10^{-27}. Cell parameters of the lattice as well as atomic positions were relaxed during geometry optimizations for bulk system, while for surface slabs only the atomic positions were allowed to relax. Convergence was determined from the root-mean-square and absolute value of the largest component of the forces and displacements, considering default values[16].

The surface energies were calculated by two different ways. For surface slabs with stoichiometric composition, the energy per unit area required to form the *n*-layer slab surface (E_{ns}) from the bulk crystal is given by:

$$E_{ns} = \frac{E(n) - n \cdot E_{bulk}}{2 \cdot A} \tag{5.2.1}$$

where A is the area of the primitive surface unit cell and E_{bulk} is the energy of a single layer worth of bulk material. On the other hand, for surface slabs with nonstoichiometric composition, the grand potential Ω approach,[17] which will be introduced in details in Section 5, was considered.

Section 3 Bulk FAPI

The structure of α-FAPI at 298 K has been reported from high resolution neutron powder diffraction data by Mark T. Weller et. al. and found to adopt a cubic perovskite

unit cell[18]. As shown in **Figure 5.3.1(a)** and **(b)**, the trigonal planar FA^+ cations lie in the cages formed by [PbI_6] octahedra. The initial structure was relaxed by using different functionals with or without dispersion and the results are gathered in **Table 5.3.1**. It can be seen that the best results are obtained when considering dispersion effects, with hybrid functionals performing generally better than GGA for structural features. The same conclusion holds for the band gap value, B3LYP-D3 and PBE0-D3 giving the best agreement with the experimental data.

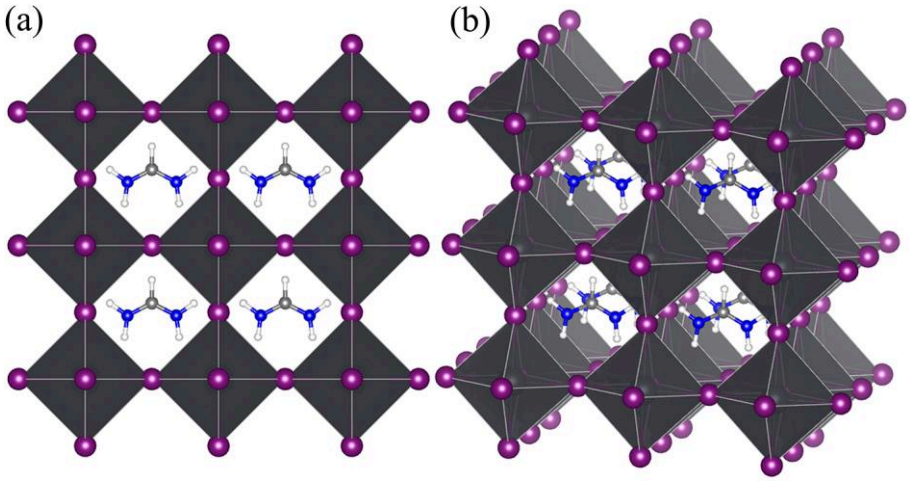

Figure 5.3.1: Ball and stick representation of the α-FAPI unit cell. The C, N, H, Pb and I atoms are represented by Grey, blue, white, dark and purple balls, respectively. The PbI_6 octahedra are shown.

Table 5.3.1: Computed lattice parameter and band gap of α-FAPI with various DFT functionals, with or without D3 dispersion.

Functional	Bandgap (eV)	SOC-corrected bandgap* (eV)	Lattice Parameter (Å)
Experiment[19]	1.48	1.48	6.361
B3LYP	2.86	1.76	6.591
B3LYP-D3	2.52	1.42	6.366
B3PW	2.74	1.64	6.503
BLYP	2.00	0.90	6.647
BLYP-D3	1.69	0.59	6.373
PBE	1.85	0.75	6.495
PBE-D3	1.67	0.57	6.371
PBE0	2.91	1.81	6.462
PBE0-D3	2.66	1.56	6.336

*: A 1.1 eV correction is applied to the computed DFT band gap value to take into

account the SOC effect. The value was obtained from calculations performed on MAPI (see Chapter 4, Section 3, Table 4.3.1 on page 76).

The structure before and after geometry optimization with PBE0-D3 are shown in **Figure 5.3.2**. The lattice has a small shrink (from 6.361 to 6.336 Å), and the FA^+ molecule rotates, leading to a tilting trigonal planar FA^+ cations relative to the crystal plane. The orientation of the FA^+ molecule has already been reported to a key parameter for the properties of FAPI[12, 20].

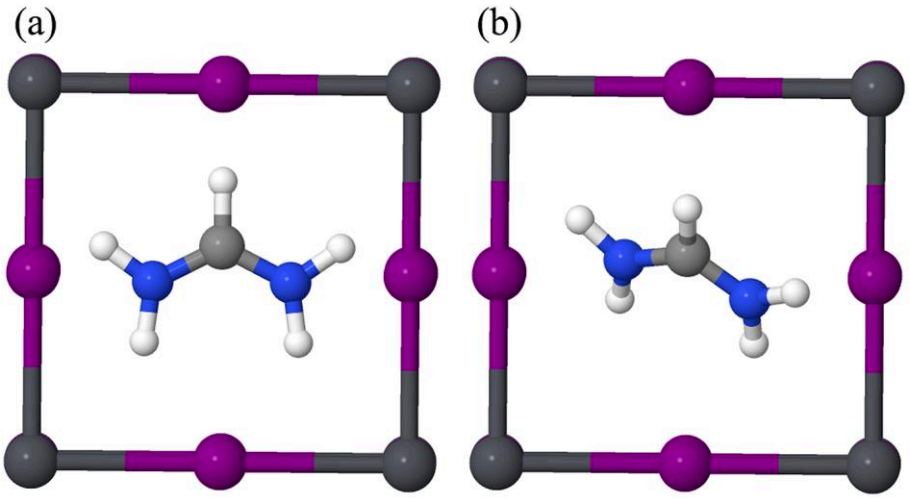

Figure 5.3.2: Top view of the α-FAPI unit cell: (a) before and (b) after geometry optimization. The C, N, H, Pb and I atoms are represented by Grey, blue, white, dark and purple balls, respectively.

Section 4 Stoichiometric surfaces

We then considered different surfaces of FAPI as it is close to the experimental scenario where a perovskite film is deposited to fabricate a PSC device[21-22]. We first investigated the (100) and (001) surfaces with stoichiometric compositions. The red and blue planes in **Figure 5.4.1** depicts (100) and (001) surfaces respectively. The only difference of these two surface models is the orientation of the FA^+ molecule. While for the (100) surface (**Figure 5.4.1(b)**), FA^+ is perpendicular to the surface plane, for (001) (**Figure 5.4.1(c)**) FA^+ is parallel to it.

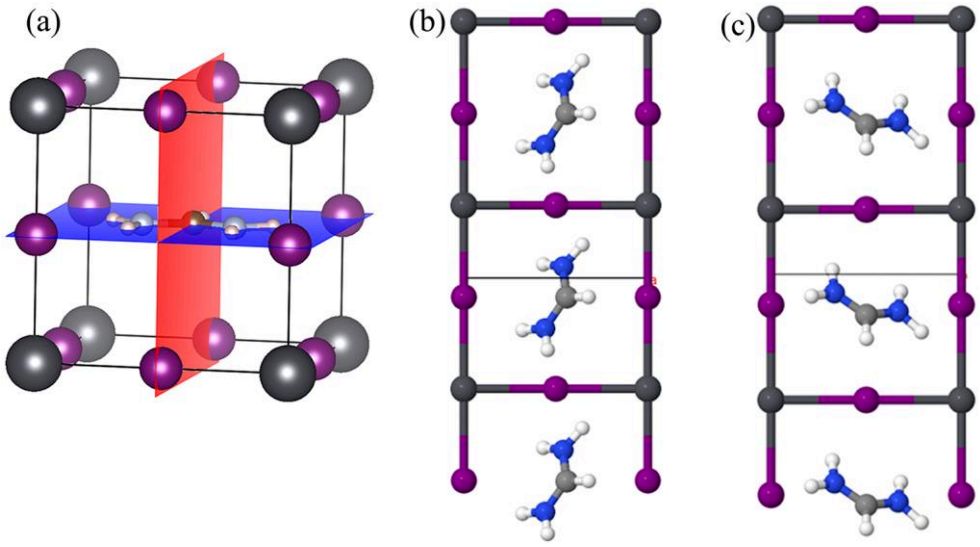

Figure 5.4.1: Construction of different surfaces from the FAPI bulk unit cell. The red plane indicates the (100) surface while the blue one indicates the (001) surface. Ball and stick representation of the 3 layers model of (100) and (001) surfaces are shown in (b) and (c), respectively. The C, N, H, Pb and I atoms are represented by Grey, blue, white, dark and purple balls, respectively.

After full atomic relaxation, the obtained bandgaps and surface energies versus number of layers are given in **Figure 5.4.2(a)** and **(b)**. Both bandgap values and surface energies are decreasing with the increasing number of layers in the slabs. The surface energies obtained are around 0.1 $J \cdot m^{-2}$ which is in line with previously-reported data[23]. Due to the high symmetry of the α-FAPI system and of the FA^+ molecule, the structures after relaxation for two surfaces share almost the same configuration with a tilting of FA^+ molecule as well as a tilting of the Pb-I framework along the z-axis, as shown in **Figure 5.4.3**. Thus, the differences obtained between the two surfaces for the bandgap and surface energies are small. However, we note that the convergence of both surface energies and band gaps as a function of the number of layers in the slab models is not satisfactory here. This might be related to the tilting of the Pb-I framework mentioned above. A similar effect is obtained for non-stoichiometric surfaces, as detailed in the next section.

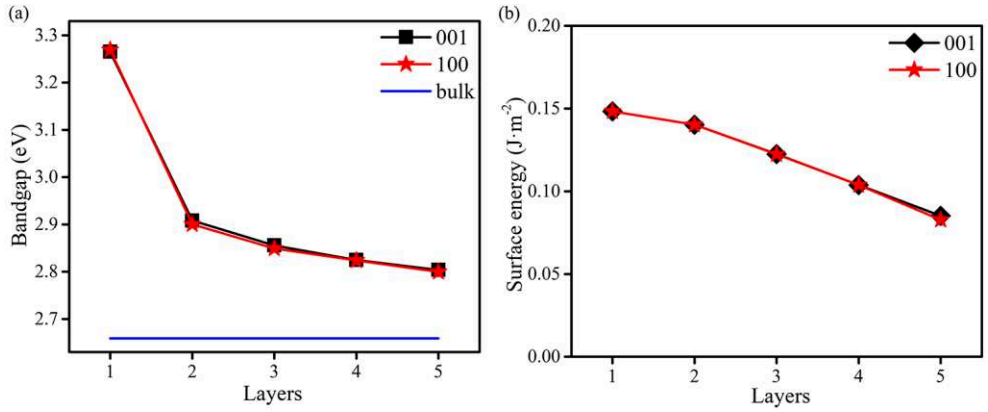

Figure 5.4.2: Calculated (a) bandgap values and (b) surface energies versus number of layers for the (100) and (001) stoichiometric surfaces of α-FAPI.

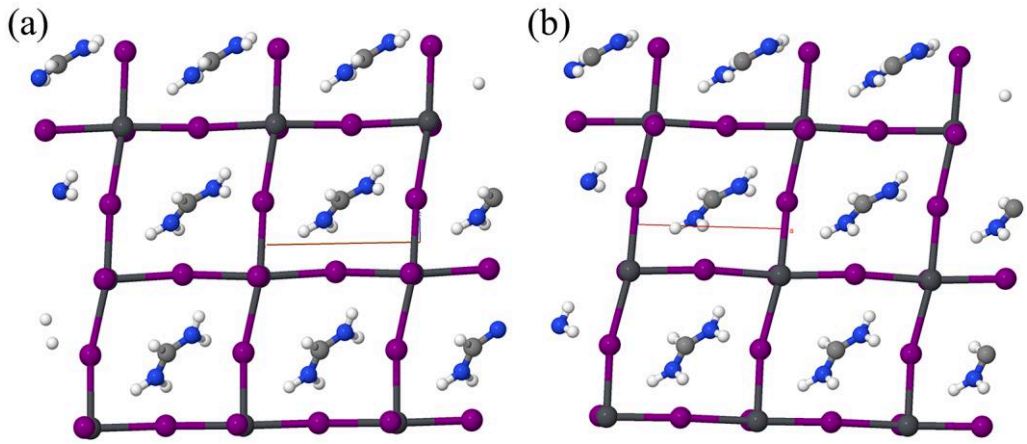

Figure 5.4.3: Ball and stick representation of the (a) (100) and (b) (001) stoichiometric surfaces after geometry optimization. The C, N, H, Pb and I atoms are represented by Grey, blue, white, dark and purple balls, respectively.

Section 5 Nonstoichiometric surfaces

In this section, the surface slabs with nonstoichiometric compositions were constructed and computed. The nonstoichiometric surfaces have the same terminations on both free surfaces created when building the slab models. However, here, both FAI-terminated and PbI_2-terminated models can be constructed. In the following, we will refer to these terminations as -FAI and -PbI_2, respectively. Examples of the resulting (100) and (001) surfaces with FAI and PbI_2 terminations and 3 layers are given in **Figure 5.5.1**.

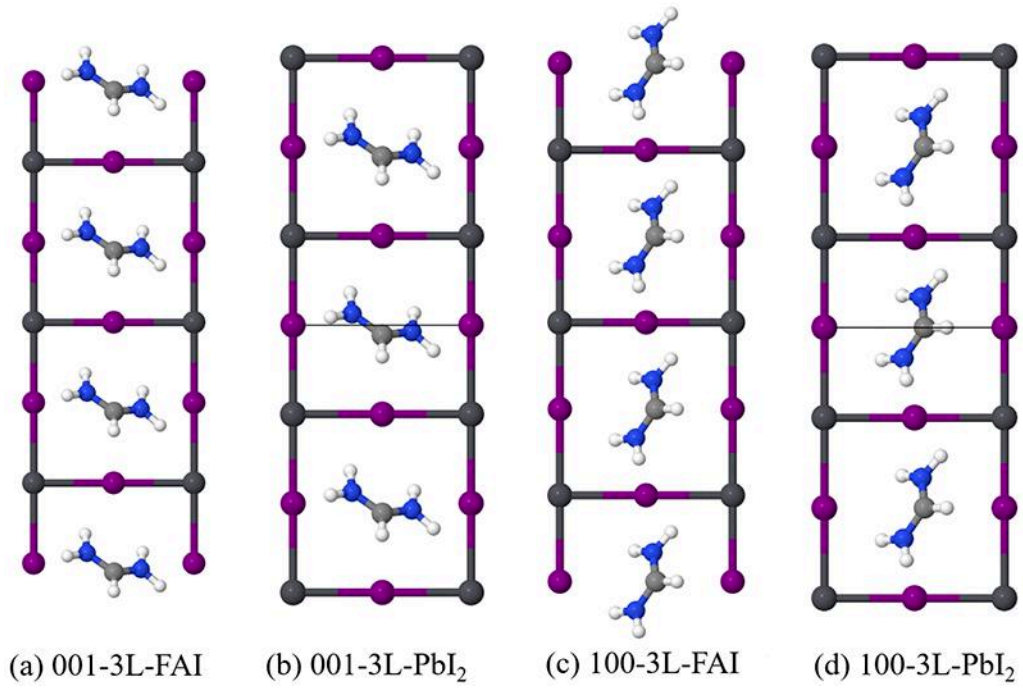

Figure 5.5.1: Ball and stick representation of the 3 layers model of: (a) (001)-FAI; (b) (001)-PbI_2; (c) (100)-FAI; (d) (100)-PbI_2. The C, N, H, Pb and I atoms are represented by Grey, blue, white, dark and purple balls, respectively.

When considering the surface energies of such nonstoichiometric surfaces, **Equation 5.2.1** is not applicable since the surface slab model must have a multiple stoichiometry of the bulk system, with n having thus an integer value. We therefore considered here the grand potential Ω approach[17]. In detail, the surface energies of PbI_2-T and FAI-T slabs are calculated by **Equations 5.5.1** and **5.5.2**, respectively:

$$\Omega(\Delta\mu_{Pb},\Delta\mu_{I},\Delta\mu_{FAPI}) \approx$$
$$E_{tot}[Pb_{\alpha}I_{\beta}(FAPI)_{\gamma}] - \alpha\mu_{Pb}^{bulk} - \frac{\beta}{2}\mu_{I_2}^{gas} - \gamma\mu_{FAPI}^{bulk} - \alpha\Delta\mu_{Pb} - \beta\Delta\mu_{I} - \gamma\Delta\mu_{FAPI} \qquad (5.5.1)$$

$$\Omega(\Delta\mu_{FA},\Delta\mu_{I},\Delta\mu_{FAPI}) \approx$$
$$E_{tot}[FA_{\delta}I_{\beta}(FAPI)_{\gamma}] - \delta\mu_{FA}^{bulk} - \frac{\beta}{2}\mu_{I_2}^{gas} - \gamma\mu_{FAPI}^{bulk} - \delta\Delta\mu_{bulk} - \beta\Delta\mu_{I} - \gamma\Delta\mu_{FAPI} \qquad (5.5.2)$$

where $E_{tot}[Pb_{\alpha}I_{\beta}(FAPI)_{\gamma}]$ is the DFT total energy of the surface slab containing α Pb atoms, β I atoms, and γ FAPI moieties, $E_{tot}[FA_{\delta}I_{\beta}(FAPI)_{\gamma}]$ is the DFT total energy of the surface slab containing δ FA, β I atoms, and γ FAPI moieties, μ_{FA}, μ_{Pb}, μ_{I}, and μ_{FAPI} are the chemical potentials of FA, Pb, I, and FAPI, which are the total chemical potential associated with both "external" force fields (electric potential energy differences, gravitational potential energy differences, etc.) and the "internal" factors (density,

temperature, etc.),[24] and μ_{FA}^{bulk}, μ_{Pb}^{bulk}, μ_{I2}^{gas}, and μ_{FAPI}^{bulk} are the chemical potentials of FA bulk, Pb bulk, μ_{I2} gas, and FAPI bulk, respectively, which are the internal chemical potentials and can be obtained from the DFT total energy per unit cell. $\Delta\mu$ is the chemical potential variations from those references, representing the growth conditions:

$$\Delta\mu_{Pb} = \mu_{Pb} - \mu_{Pb}^{bulk}$$
$$\Delta\mu_{I} = \mu_{I} - \frac{1}{2}\mu_{I_2}^{gas}$$
$$\Delta\mu_{FAPI} = \mu_{FAPI} - \mu_{FAPI}^{bulk} \quad (5.5.3)$$

Assuming that $\Delta\mu_{FAPI} = 0$ and the system is under equilibrium for Pb, I_2, FAI, and PbI_2 phases, the thermodynamic stable range of variation of $\Delta\mu_{FA}$, $\Delta\mu_{Pb}$ and $\Delta\mu_{I}$ for equilibrium growth of FAPI corresponds to the following conditions:

$$\Delta\mu_{FA} + \Delta\mu_{Pb} + 3\Delta\mu_{I} = \Delta H(FAPI)$$
$$\Delta\mu_{FA} + \Delta\mu_{I} < \Delta H(FAI)$$
$$\Delta\mu_{Pb} + 2\Delta\mu_{I} < \Delta H(PbI_2) \quad (5.5.4)$$

We then have the following domain of variation:

$$\Delta H(FAPI) - \Delta H(FAI) < \Delta\mu_{Pb} + 2\Delta\mu_{I} < \Delta H(PbI_2) \quad (5.5.5)$$

where ΔH is the heat of formation. We summarize E_{tot} and ΔH of the solid and gas phases in **Table 5.5.1**:

Table 5.5.1: Total energies E_{tot} and heat of formations ΔH for various systems.

System	E_{tot} (a.u.)	System	ΔH (eV)
FAPI (cubic phase)	-1230.771011	FAPI	-7.607
FAI (solid phase[25])	-1785.059071	FAI	-4.566
PbI_2 (CdI2 structure, 2H type[26])	-784.505972	PbI_2	-3.303
I_2 (molecule)	-591.446471		
H_2 (molecule)	-1.16711728		
N_2 (molecule)	-109.398267		
C (graphite, AB stack[27])	-152.230613		
Pb (metal, fcc lattice[28])	-192.948037		

According to the obtained results, we can obtain a stability diagram as shown in **Figure 5.5.2**. The choice of chemical potentials can reflect the experimental growth conditions. For example, the $\Delta\mu_{Pb}$ =0 case corresponds to the case where the I atoms are in excess and no isolated Pb atom can be seen in the environment, corresponding to a I-rich environment. The stability diagram obtained by our calculation has a very narrow stability region indicating that α-FAPI is not stable, in line with the fact that α-FAPI has a very fast transition into δ-FAPI under ambient conditions.[19]

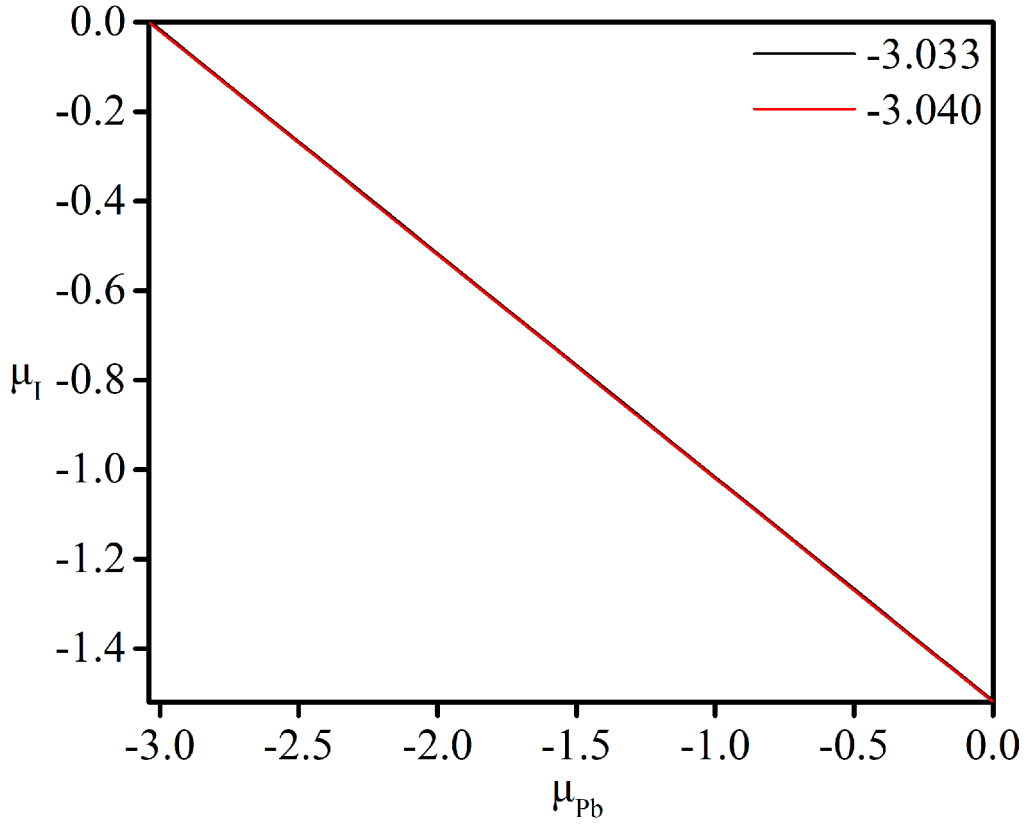

Figure 5.5.2: Stability diagram of α-FAPI as a function of the range of variation of the Pb and I chemical potentials, with two values considered for $\Delta H(PbI_2)$. The -3.033 eV value corresponds to $\Delta H(PbI_2)$, while the -3.040 eV value corresponds to the value of [ΔH(FAPI) - ΔH(FAI)]. The red region is the thermodynamic stable range for equilibrium growth of α-FAPI.

We then selected three different groups of chemical potentials reflecting different growth conditions. More precisely, the following conditions gave been chosen: i) Pb-rich environment with $\Delta\mu_{Pb}$=-3.037 eV, $\Delta\mu_{I}$=0 eV, $\Delta\mu_{FA}$=-4.564 eV; ii) I-rich environment with $\Delta\mu_{Pb}$=0 eV, $\Delta\mu_{I}$=-1.518 eV, $\Delta\mu_{FA}$=-3.046 eV; iii) meditate environment with $\Delta\mu_{Pb}$=-1.537 eV, $\Delta\mu_{I}$=-0.75 eV, $\Delta\mu_{FA}$=-3.813 eV. The calculated surface energies are gathered in **Table 5.5.2**. Due to the symmetry of α-FAPI, the energy difference between two different surfaces with the same termination is small.

Furthermore, no obvious difference is seen when varying the chemical potentials in the results, indicating that the surface terminations of α-FAPI is independent of the growth conditions. This conclusion is different from the case of MAPI where the surface terminations are largely dependent on the growth conditions[29].

Table 5.5.2: Surface energies and bandgap values of α-FAPI surfaces with nonstoichiometric compositions under different chemical potentials.

Surface	Surface Energy ($J \cdot m^{-2}$)			
Number of layers	$\Delta\mu_{Pb}$=-3.037, $\Delta\mu_I$=0, $\Delta\mu_{FA}$=-4.564	$\Delta\mu_{Pb}$=0, $\Delta\mu_I$=-1.518, $\Delta\mu_{FA}$=-3.046	$\Delta\mu_{Pb}$=-1.537, $\Delta\mu_I$=-0.75, $\Delta\mu_{FA}$=-3.813	Bandgap (eV)
(001)-PbI_2				
1	0.251	0.251	0.251	3.15
2	0.216	0.216	0.216	2.99
3	0.195	0.195	0.195	2.90
4	0.176	0.176	0.176	2.85
5	0.151	0.151	0.151	2.70
(001)-FAI				
1	0.120	0.121	0.120	3.29
2	0.093	0.093	0.093	3.12
3	0.073	0.074	0.073	2.97
4	0.055	0.055	0.055	2.90
5	0.036	0.036	0.036	2.84
(100)-PbI_2				
1	0.253	0.253	0.253	3.00
2	0.216	0.216	0.216	2.99
3	0.195	0.195	0.195	2.89
4	0.224	0.224	0.224	2.57
5	0.156	0.156	0.156	2.84
(100)-FAI				
1	0.119	0.120	0.119	3.28
2	0.092	0.093	0.092	3.13
3	0.072	0.073	0.073	2.99
4	0.048	0.049	0.048	2.93
5	0.035	0.035	0.035	2.85

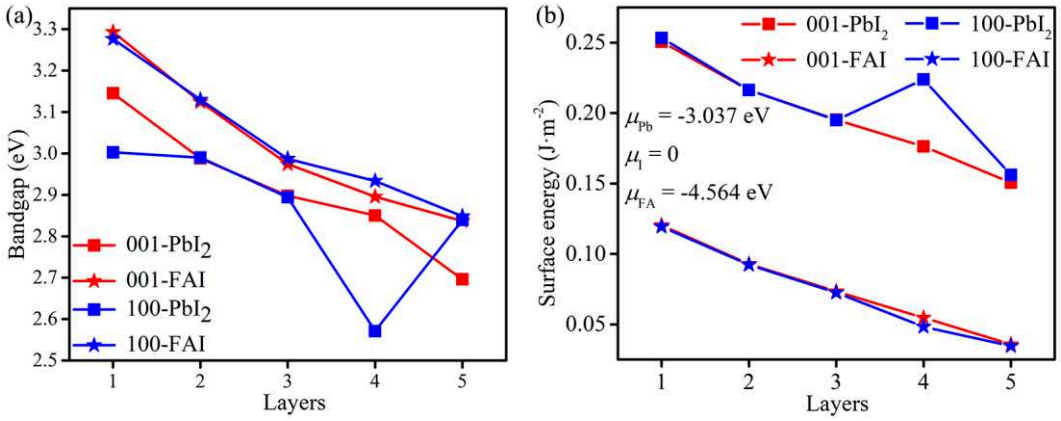

Figure 5.5.3: (a) Bandgap and (b) surface energies of α-FAPI surfaces as a function of the number of layers. The surface energies are calculated with chemical potentials μ_{Pb}=-3.037, μ_I=0, μ_{FA}=-4.5637 eV.

Figures 5.5.3 (a) and **(b)** show the obtained bandgap and surface energies as a function of the number of layers, with the surface energies being calculated under Pb-rich conditions. The bandgap of the -PbI_2 surfaces is smaller than the one obtained with -MAI terminations, the formers being closer to the bulk bandgap, indicating that -PbI_2 surfaces might be then more suitable for PV application. However, the surface energies of -PbI_2 terminated surfaces are larger than those of the -FAI terminated ones, indicating that -FAI surfaces are more stable. We note that in the (100)-PbI_2 surface energies reported, the slab with 4 layers is peculiar. This may be explained from the structure shown in **Figure 5.5.4**. After relaxation, the orientation of the FA molecules in the (100)-PbI_2 model are mostly disordered from one layer to the other, while in the 4-layer (4L) case all FA moieties are ordered with the same orientation. A comparison with the 4L structure before relaxation (see **Figure 5.5.4 (e)**) reveals that the geometry optimization mostly affects the Pb-I framework in this case. It might be then concluded here that the FA molecules orientation in the slab plays an important role in the stability and the electronic properties of FAPI surfaces.

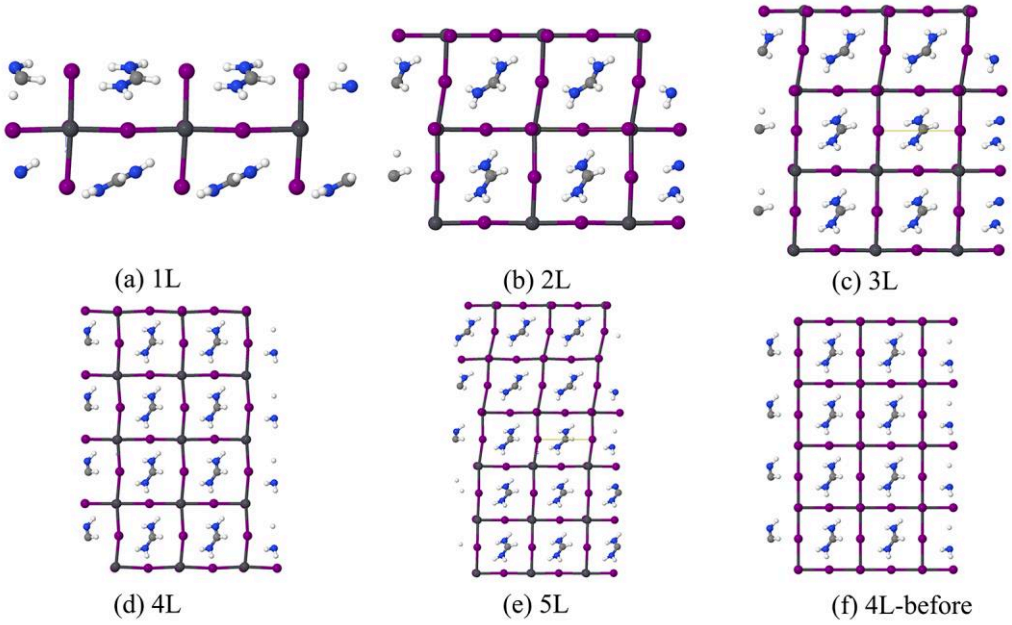

Figure 5.5.4: Ball and stick representation of the α-FAPI (100)-PbI_2 relaxed surfaces with: (a) 1-layer; (b) 2-layer; (c) 3-layer; (d) 4-layer; (e) 5-layer. The structure of the 4-layer model before atomic relaxation is shown in (f) for comparison. The C, N, H, Pb and I atoms are represented by Grey, blue, white, dark and purple balls, respectively.

We also note that the surface energy convergence as a function of the number of layers is again not satisfactory. From **Figure 5.5.4**, it is clear that a shear stress appears during the atomic relaxation, with the Pb-I framework being more and more distorted as a function of the number of layers in the model. To better investigate this point, a geometry optimization under constraints imposed on the Pb-I framework has been performed, so that all "symmetry-equivalent" Pb and I atoms have a "symmetry-equivalent" displacement during the relaxation. Only the α-FAPI (001)-FAI case has been considered as an example. The obtained structures are shown in **Figure 5.5.5** and the comparison of the surface energies, along with the energy differences between slab of increasing thickness are gathered in **Table 5.5.3**. Although higher surface energies than in the unconstrained case are obtained, it is clear that a much better convergence is obtained. The corresponding bandgap values don't follow this conclusion, as listed in **Table 5.5.4**, which may be due to the lack of data points and we need to calculate more models which has more layers. However, it is predicted that the increase of layers can lead to a situation that the bandgap of the slab is close to that of the bulk system. From this perspective, layers under symmetry-constrained relaxation can give a faster convergence on bandgap layers.

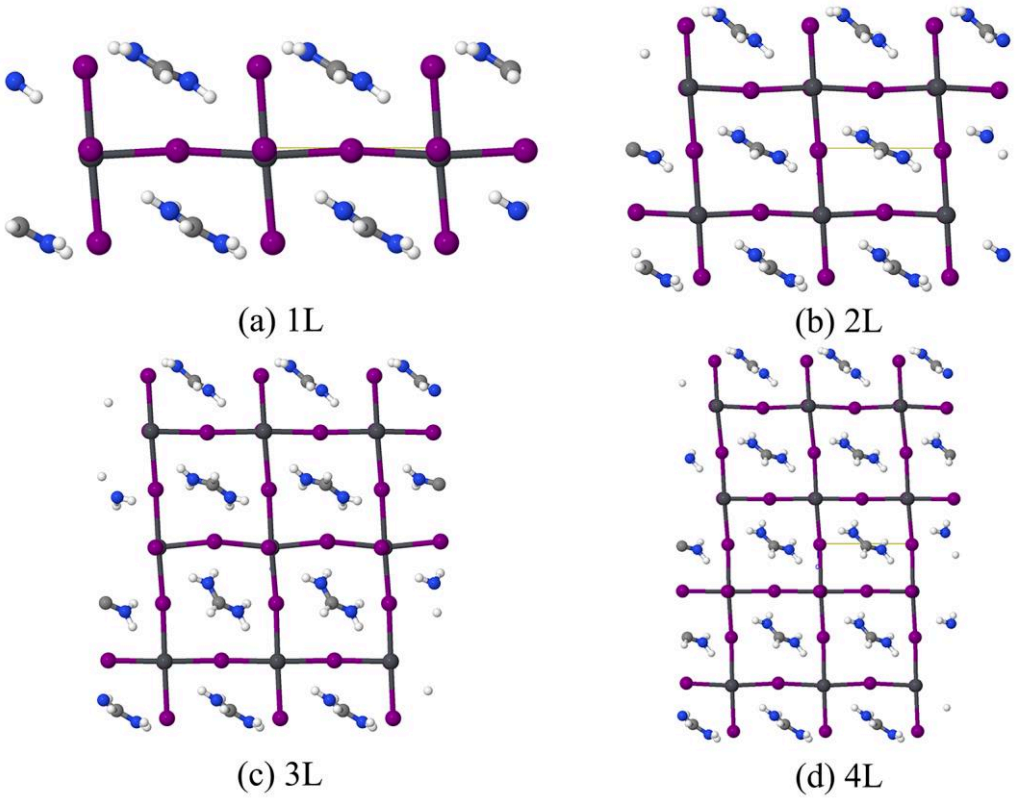

Figure 5.5.5: Ball and stick representation of the α-FAPI (001)-FAI surfaces after symmetry-constrained relaxation of the Pb-I framework, with: (a) 1-layer; (b) 2-layer; (c) 3-layer; (d) 4-layer slab models. The C, N, H, Pb and I atoms are represented by Grey, blue, white, dark and purple balls, respectively.

Table 5.5.3: Surface energies ($J \cdot m^{-2}$) of α-FAPI (001)-FAI surfaces, obtained with and without symmetry-constrained relaxation.

Number of layers	Surface Energy without constraint	Surface Energy Difference	Surface Energy with constraint	Surface Energy Difference
out1L	0.120		0.130	
2L	0.093	-0.027	0.112	-0.018
3L	0.073	-0.020	0.095	-0.017
4L	0.055	-0.018	0.090	-0.005

Table 5.5.4: Bandgap values (eV) of α-FAPI (001)-FAI surfaces, obtained without and with symmetry-constrained relaxation.

Number of layers	Bandgap without constraint	Bandgap Difference	Bandgap with constraint	Bandgap Difference
1L	3.29		3.35	
2L	3.12	-0.17	3.06	-0.29
3L	2.97	-0.15	2.94	-0.12
4L	2.90	-0.07	2.79	-0.15

Conclusions

In summary, we reported in this chapter preliminary calculations performed both on bulk *α*-FAPI as well as on two of its low-index surfaces, considering different terminations with both stoichiometric and non-stoichiometric models.

For the bulk system, among the different DFT functionals tested, PBE0 and B3LYP were found to be the best performing DFT models both for structural and electronic properties. Better results are generally obtained when including dispersion effects.

For all surfaces considered, a tilting of the Pb-I framework was observed during the unconstrained atomic relaxation performed, leading to a poor convergence of both surface energies and band gaps as a function of the number of layers in the slab models considered. By performing a symmetry-constrained relaxation, a much better convergence could be achieved for the (001)-MAI non-stoichiometric case which was chosen as a test case. In addition, -PbI_2 surfaces might have a more suitable bandgap for PV application, while -MAI surfaces are more stable. We also noted that surface energies are independent from the growth conditions. Finally, the orientation of FA molecule might affect the properties of *α*-FAPI surfaces.

Overall, this preliminary investigation performed on different *α*-FAPI systems can help to better understand its overall properties. In particular, the different surface models considered could be used to build interface models with TiO_2, to be the compared with the MAPI/CBA/TiO_2 case presented in the previous chapter.

References

1. Stranks, S.D.; Eperon, G.E.; Grancini, G.; Menelaou, C.; Alcocer, M.J.P.; Leijtens, T.; Herz, L.M.; Petrozza, A.; and Snaith, H.J. Electron-Hole Diffusion Lengths Exceeding 1 Micrometer in an Organometal Trihalide Perovskite Absorber. *Science* **2013**. *342*, 341–344.
2. Mosconi, E.; Azpiroz, J.M.; and De Angelis, F. Ab Initio Molecular Dynamics Simulations of Methylammonium Lead Iodide Perovskite Degradation by Water. *Chem. Mater.* **2015**. *27*, 4885–4892.
3. Koh, T.M.; Fu, K.; Fang, Y.; Chen, S.; Sum, T.C.; Mathews, N.; Mhaisalkar, S.G.; Boix, P.P.; and Baikie, T. Formamidinium-Containing Metal-Halide: An Alternative Material for Near-IR Absorption Perovskite Solar Cells. *J. Phys. Chem. C* **2014**. *118*, 16458–16462.
4. Qiu, Z.; Li, N.; Huang, Z.; Chen, Q.; and Zhou, H. Recent Advances in Improving Phase Stability of Perovskite Solar Cells. *Small Methods* **2020**. *4*, 1900877.
5. Zheng, X.; Wu, C.; Jha, S.K.; Li, Z.; Zhu, K.; and Priya, S. Improved Phase Stability of Formamidinium Lead Triiodide Perovskite by Strain Relaxation. *ACS Energy Lett.* **2016**. *1*, 1014–1020.
6. He, X.; Guo, P.; Wu, J.; Tu, Y.; Lan, Z.; Lin, J.; and Huang, M. Hybrid perovskite by mixing formamidinium and methylammonium lead iodides for high-performance planar solar cells with efficiency of 19.41 *Solar Energy* **2017**. *157*, 853 – 859.
7. Gao, X.X.; Luo, W.; Zhang, Y.; Hu, R.; Zhang, B.; Züttel, A.; Feng, Y.; and Nazeeruddin, M.K. Stable and High-Efficiency Methylammonium-Free Perovskite Solar Cells. *Adv. Mater.* **2020**. *32*, 1905502.
8. Lee, J.W.; Kim, D.H.; Kim, H.S.; Seo, S.W.; Cho, S.M.; and Park, N.G. Formamidinium and Cesium Hybridization for Photo- and Moisture-Stable Perovskite Solar Cell. *Adv. Energy Mater.* **2015**. *5*, 1501310.

9. Xie, F.; Chen, C.C.; Wu, Y.; Li, X.; Cai, M.; Liu, X.; Yang, X.; and Han, L. Vertical recrystallization for highly efficient and stable formamidinium-based invertedstructure perovskite solar cells. *Energy Environ. Sci.* **2017**. *10*, 1942–1949.
10. Charles, B.; Dillon, J.; Weber, O.J.; Islam, M.S.; and Weller, M.T. Understanding the stability of mixed A-cation lead iodide perovskites. *J. Mater. Chem. A* **2017**. *5*, 22495–22499.
11. Min, H.; Kim, M.; Lee, S.U.; Kim, H.; Kim, G.; Choi, K.; Lee, J.H.; and Seok, S.I. Efficient, stable solar cells by using inherent bandgap of -phase formamidinium lead iodide. *Science* **2019**. *366*, 749–753.
12. Amat, A.; Mosconi, E.; Ronca, E.; Quarti, C.; Umari, P.; Nazeeruddin, M.K.; Grätzel, M.; and De Angelis, F. Cation-Induced Band-Gap Tuning in Organohalide Perovskites: Interplay of Spin–Orbit Coupling and Octahedra Tilting. *Nano Lett.* **2014**. *14*, 3608–3616.
13. Adamo, C. and Barone, V. Toward reliable density functional methods without adjustable parameters: The PBE0 model. *J. Chem. Phys.* **1999**. *110*, 6158–6170.
14. Grimme, S. Semiempirical GGA-type density functional constructed with a long-range dispersion correction. *Journal of Computational Chemistry* **2006**. *27*, 1787–1799.
15. Metz, B.; Stoll, H.; and Dolg, M. Small-core multiconfiguration-Dirac–Hartree–Fockadjusted pseudopotentials for post-d main group elements: Application to PbH and PbO. *J. Chem. Phys.* **2000**. *113*, 2563–2569.
16. Erba, A.; Baima, J.; Bush, I.; Orlando, R.; and Dovesi, R. Large-Scale Condensed Matter DFT Simulations: Performance and Capabilities of the CRYSTAL Code. *J. Chem. Theory Comput.* **2017**. *13*, 5019–5027.
17. Haruyama, J.; Sodeyama, K.; Han, L.; and Tateyama, Y. Termination Dependence of Tetragonal $CH_3NH_3PbI_3$ Surfaces for Perovskite Solar Cells. *J. Phys. Chem. Lett.* **2014**. *5*, 2903–2909.
18. Weller, M.T.; Weber, O.J.; Frost, J.M.; and Walsh, A. Cubic Perovskite Structure of Black Formamidinium Lead Iodide, -$[HC(NH_2)_2]PbI_3$, at 298 K. *J. Phys. Chem. Lett.* **2015**. *6*, 3209–3212.

19. Han, Q.; Bae, S.H.; Sun, P.; Hsieh, Y.T.; Yang, Y.M.; Rim, Y.S.; Zhao, H.; Chen, Q.; Shi, W.; Li, G.; and Yang, Y. Single Crystal Formamidinium Lead Iodide ($FAPbI_3$): Insight into the Structural, Optical, and Electrical Properties. *Adv. Mater.* **2016**. *28*, 2253–2258.
20. Karthick, S.; Ríos-Ramírez, J.J.; and Velumani, S. 12 Possible Orientations of organic Formamidinium cation and its structural analysis by First Principles calculations using Van der Waals-Density functional Theory. *15th International Conference on Electrical Engineering, Computing Science and Automatic Control (CCE)* **2018**, 1–5.
21. Li, Z.; Klein, T.R.; Kim, D.H.; Yang, M.; Berry, J.J.; van Hest, M.F.; and Zhu, K. Scalable fabrication of perovskite solar cells. *Nat. Rev. Mater.* **2018**. *3*, 1–20.
22. Yang, M.; Kim, D.H.; Klein, T.R.; Li, Z.; Reese, M.O.; Tremolet de Villers, B.J.; Berry, J.J.; van Hest, M.F.A.M.; and Zhu, K. Highly Efficient Perovskite Solar Modules by Scalable Fabrication and Interconnection Optimization. *ACS Energy Lett.* **2018**. *3*, 322–328.
23. Guo, Y.; Li, C.; Li, X.; Niu, Y.; Hou, S.; and Wang, F. Effects of Rb Incorporation and Water Degradation on the Stability of the Cubic Formamidinium Lead Iodide Perovskite Surface: A First-Principles Study. *J. Phys. Chem. C* **2017**. *121*, 12711–12717.
24. Kittel, C.; Charles Kittel, H.; Charles, K.; Kroemer, H.; and Herbert, K. *Thermal Physics*. W. H. Freeman, **1980**.
25. Petrov, A.A.; Goodilin, E.A.; Tarasov, A.B.; Lazarenko, V.A.; Dorovatovskii, P.V.; and Khrustalev, V.N. Formamidinium iodide: crystal structure and phase transitions. *Acta Crystallographica Section E: Crystallographic Communications* **2017**. *73*, 569–572.
26. Sears, W.M.; Klein, M.; and Morrison, J. Polytypism and the vibrational properties of PbI_2. *Phys. Rev. B* **1979**. *19*, 2305.
27. Zhao, Y.X. and Spain, I.L. X-ray diffraction data for graphite to 20 GPa. *Phys. Rev. B* **1989**. *40*, 993.

28. Tang, Y.C. and Pauling, L. The structure of alloys of lead and thallium. *Acta Crystallographica* **1952**. *5*, 39–44.
29. Haruyama, J.; Sodeyama, K.; Han, L.; and Tateyama, Y. Surface Properties of $CH_3NH_3PbI_3$ for Perovskite Solar Cells. *Acc. Chem. Res.* **2016**. *49*, 554–561.

Conclusions

In this thesis, we aimed to contribute to a better understanding of the surfaces and interfaces involving perovskite compounds and governing the performances of PSCs, by using DFT-based computational protocols, with a comparison with experimental data, when available.

After introducing the main computational tools and approaches considered in this thesis in Chapter II, we first performed DFT calculations on TiO_2 anatase bulk and its (101) surface, and on the adsorption of four small organic ligands on the latter, aiming to select the best candidate for surface engineering of PSC in Chapter III. The benchmark calculations performed with different DFT models on bulk anatase indicated that hybrid functionals can both well reproduce the experimental lattice parameters with a small overestimation of the bandgap. For the adsorption calculations, a bidentate binding mode was found to be preferred for all ligands, in line with the vibrational frequencies investigation carried out which showed a general good agreement with available experimental data. From the properties computed, including DOS, dipole moments, and the work function obtained by experiments, it is derived that CBA and NBA are suitable candidates to improve the performance of PSC.

In Chapter IV, we then simulated the heterointerface between the MAPI perovskite and TiO_2, in which the CBA ligand has been used to act as a bifunctional linker. Our calculations indicated that CBA can efficiently link the perovskite and the oxide moieties, ensuring stability of the interface through Ti-O and Pb-Cl interactions. Furthermore, CBA ligand can induce a favorable effect to improve band alignment and thus electron transfer from MAPI to TiO_2, with an ultrafast electron injection time in the femtosecond timescale. Overall, the proposed DFT-based computational protocol therefore indicated that by surface engineering with a bifunctional linker such as CBA, a better stability, together with improved band alignment and electron injection, could be obtained for PSC systems.

In chapter V, we reported preliminary DFT calculations performed both on bulk α-FAPI as well as on two of its low-index surfaces, considering different terminations with both stoichiometric and non-stoichiometric models. Among the different DFT models considered for bulk calculation, hybrid functionals coupled to empirical dispersion corrections were found to be the best performing functionals. For all surfaces considered, a tilting of the Pb-I framework was observed during the unconstrained

atomic relaxation performed, leading to a poor convergence of both surface energies and band gaps as a function of the number of layers in the slab models considered. By performing a symmetry-constrained relaxation, a better convergence could be achieved for surface energies of the (001)-MAI non-stoichiometric case, chosen as a test case. In addition, -PbI_2 surfaces might have a more suitable bandgap for PV application, while -MAI surfaces are more stable. We also noted that surface energies are independent from the growth conditions. Finally, we noted that the orientation of FA molecules in the unit cell might affect the properties of α-FAPI surfaces.

Overall, the DFT data obtained both on the TiO_{2-} and MAPI-based systems investigated in this thesis were in good agreement with the available experimental results, indicating that the modeling strategy considered here can help to better understand the mechanisms involved in PSC and provide useful guidelines for choosing suitable ligand candidates at the experimental level. As for the model α-FAPI systems considered, the preliminary results obtained could serve to propose interface models of stabilized α-FAPI with oxides, together with suitable bifunctional linkers like in the MAPI/CBA/TiO_2 case. In particular, the proposed DFT-based computational strategy detailed in this manuscript could in principle also be considered to screen different ligand candidates for PSC application or for cases in which interfaces play a key role for solar cell applications.

Publications

Title	Journal	Authors	Statues	Year	Doi	Note
Improving the heterointerface in hybrid organic–inorganic perovskite solar cells by surface engineering: Insights from periodic hybrid density functional theory calculations.	J. Comput. Chem.	**Jun Su**, Tao Zhu, Thierry Pauporté, Ilaria Ciofini, and Frédéric Labat.	Published	2020	10.1002/jcc.26215	Related to Chapter 4
Response Enhancement of Self-Powered Visible-Blind UV Photodetectors by Nanostructured Heterointerface Engineering.	Adv. Funct. Mater.	Tao Zhu, **Jun Su**, José Alvarez, Grégory Lefèvre, Frédéric Labat, Ilaria Ciofini, and Thierry Pauporté.	Published	2019	10.1002/adfm.201903981	Related to Chapter 4
Interfacial Engineering through Chloride-Functionalized Self-Assembled Monolayer for High Efficiency Perovskite Solar Cells.	ACS Appl. Mater. & Inter.	Tao Zhu, **Jun Su**, Frédéric Labat, Ilaria Ciofini, and Thierry Pauporté.	Published	2019	10.1021/acsami.9b18034	Related to Chapter 3
Low-Temperature Solution Synthesis of Au-Modified ZnO Nanowires for Highly Efficient Hydrogen Nanosensors.	ACS Appl. Mater. & Inter.	Oleg Lupan, Vasile Postica, Niklas Wolff, **Jun Su**, Frédéric Labat, Ilaria Ciofini, Heather Cavers, Rainer Adelung, Oleksandr Polonskyi, Franz Faupel, Lorenz Kienle, Bruno Viana, and Thierry Pauporté.	Published	2019	ACS Appl. Mater. & Inter.	

Presentations at scientific events

1. **Jun Su**, Tao Zhu, Thierry Pauporté, Frédéric Labat, and Ilaria Ciofini. *18th International Conference on Density-Functional Theory and its Applications*. Alicante, Spain (Jul. 22-26, 2019). **Contributed Talk**.
2. **Jun Su**, Tao Zhu, Thierry Pauporté, Frédéric Labat, and Ilaria Ciofini. *2nd Quantum International Frontiers*. ShangHai, China (Nov. 18-22, 2019). **Poster**. (Best Poster 2nd Award)
3. **Jun Su**, Tao Zhu, Thierry Pauporté, Frédéric Labat, and Ilaria Ciofini. *9ème édition des Journées Nationales du PhotoVoltaïque (9th National Photovoltaic Day)*. Dourdan, France (Dec. 2-6, 2019). **Poster**.

List of figures

List of tables

Résumé Thèse

Chapitre 1 : Introduction

Le solaire PV est une technologie permettant de directement convertir l'énergie solaire en électricité, en utilisant une jonction PN. Cette dernière est constituée de semi-conducteurs de type p et de type n, qui peuvent être obtenus en dopant avec des accepteurs et des donneurs d'électrons. Par exemple, un semi-conducteur de type n peut être produit par dopage avec un élément chimique contenant plus d'électrons de valence que l'élément hôte. Dans ce cas, le potentiel chimique électronique augmente, tout comme le niveau de fermi qui devient proche de la bande de conduction. Comme représenté en **Figure 1**, les électrons se rassemblent dans la région n, tandis que les trous se réunissent dans la région p. Quand les deux régions sont mises en contact, les électrons diffusent du côté de type n vers le côté de type p, et les trous sont transférés dans le sens inverse. Le déplacement des porteurs de charge conduit à une polarisation des deux zones et à la création d'un champ électrique intégré qui bloque la recombinaison des porteurs. Lorsque la jonction PN est connectée à l'électrode externe, les porteurs quittent alors le dispositif et génèrent ainsi un courant externe.

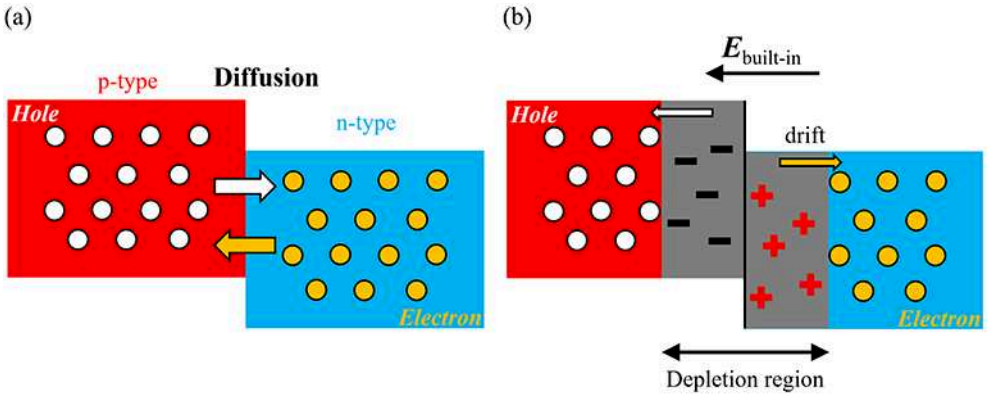

Figure 1 : (a) Diffusion de porteurs de charge libres entre un matériau de type p et un matériau de type n ; (b) Formation d'une région d'appauvrissement avec un champ électrique intégré dans une jonction pn.

Jusqu'à aujourd'hui, la technologie solaire photovoltaïque se divise en trois générations et la classification de l'énergie solaire photovoltaïque dépend principalement du rapport entre l'efficacité de conversion d'énergie et le coût de production global. Une technologie photovoltaïque mature est la cellule solaire au silicium, qui constiteue la première génération de cellule solaire. Ce type de cellule se heurte désormais à certains problèmes : son rendement est limité, sa procédure de production est complexe et elle manque de

flexibilité. Les technologies PV de deuxième génération coûtent moins cher à fabriquer car elles sont produites par une méthode chimique et non à haute température, mais leurs performances restent limitées. Ainsi, les dispositifs appartenant à la troisième génération de cellules solaires attirent beaucoup d'attention. Bien qu'il en existe plusieurs types, les cellules solaires pérovskites (PSC) représente un cas d'étude intéressant car elles ont une efficacité de photoconversion (PCE) comparable à celui d'une cellule solaire au silicium de première génération. Il s'agit d'une technologie récente, qui a été proposée pour la première fois en 2009 avec une PCE de seulement 3.8% mais qui a vu un développement très rapide. Un autre avantage majeur de la pérovskite est qu'elle peut être traitée en solution et peut donc être utilisée pour construire des modules flexibles. Les composés pérovskites présentent cependant certains inconvénients, comme des problèmes de stabilité ou encore une certaine toxicité à cause de l'élément chimique principal qu'elles contiennent.

Le mécanisme de fonctionnement de base d'une PSC est le suivant: lorsqu'elle est irradiée, la structure pérovskite fonctionne comme couche absorbant la lumière, et les porteurs de charge sont générés. Ensuite, les électrons et les trous sont transférés le long de leurs couches de transfert jusqu'aux électrodes. L'ETL (couche de transport d'électrons) et la HTL (couche de transport de trous) jouent un rôle important dans ce processus car elles contrôlent le transport des porteurs. Bien qu'il s'agisse ainsi d'un dispositif présentant de nombreuses interfaces, l'interface entre la pérovskite et l'ETL est extrêmement importante pour le transport d'électrons.

La structure type d'une structure de type pérovskite est présentée en **Figure 1. 2**. Il s'agit d'un composé de formule ABX_3, avec un site A occupé par des cations, un site B principalement occupé par Pb et un site X occupé par des atomes d'halogène. La bande interdite idéale d'un tel matériau doit être d'environ 1.5 eV, ce qui idéal pour l'absorption de la lumière du soleil. Dans nos recherches, nous nous sommes principalement intéressés à l'iodure de plomb de méthylammonium MAPI et l'iodure de plomb formamidinium FAPI. En tant qu'ETL, le matériau le plus couramment utilisé est TiO_2. Il est fondamental de comprendre comment connecter l'ETL à la pérovskite de la manière la plus efficace possible. Une première possibilité consiste à les connecter directement, mais cela peut conduire à une certaine perte d'efficacité de transfert d'électrons, car il existe un décalage de structures et de bandes électroniques entre ces deux types de composés. Une stratégie possible consiste alors à intercaler des molécules organiques afin de les lier. Ceux-ci peuvent en effet jouer le rôle de ligands pour lier la pérovskite au TiO_2 et aider à améliorer l'alignement des bandes. D'un point de vue chimique, un groupe carboxylique est normalement utilisé pour ancrer le ligand à au semi-conducteur et la conjugaison électronique est assurée en utilisant des systèmes π conjugués courts. Afin de mieux comprendre comment optimiser l'interaction pérovskite-ligand, c'est ce à quoi nous nous sommes principalement intéressés dans ce travail en utilisant des outils de modélisation basés sur la théorie de la fonctionnelle de la densité (DFT) avec

conditions périodiques aux limites. Dans les prochaines sections, différents ligands sont tout d'abord testés afin d'optimiser l'interface MAPI/TiO_2, puis la modélisation d'un système modèle représentatif de l'interface complète MAPI/ligand/TiO_2 est envisagée. La dernière partie porte sur un travail préliminaire de modélisation du bulk et des surfaces de la pérovskite FAPI.

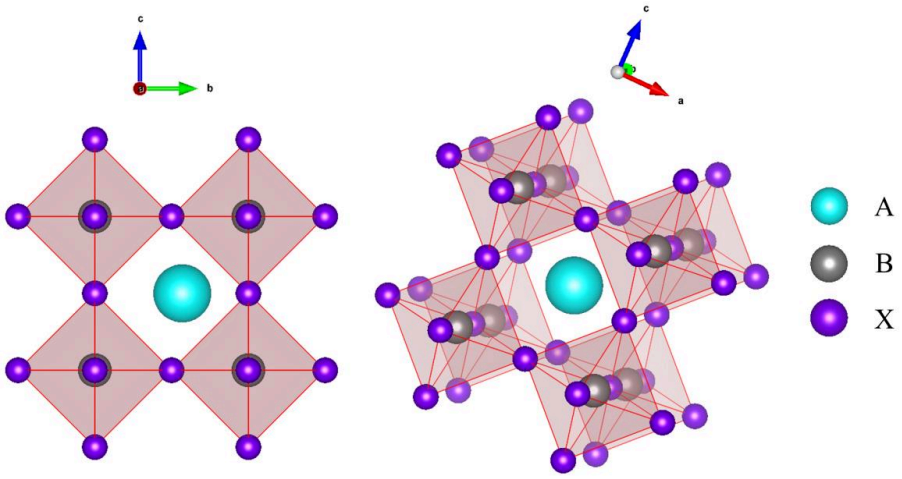

Figure 2 : Structure d'une pérovskite hybride organique-inorganique.

Chapitre 2 : Description des méthodes

Le travail de modélisation présenté ici a été réalisé en lien avec le travail de caractérisation expérimentale effectuée au sein du groupe du Dr Thierry Pauporté. Mon travail a consisté à concevoir des modèles d'interfaces complexes, et à effectuer des calculs théoriques afin d'obtenir des informations sur leurs propriétés électroniques, structurales, vibrationnelles et énergétiques.

Tous les calculs ont été effectués en utilisant une approche DFT périodique en utilisant le programme CRYSTAL17, qui utilise des fonctions de base de type Gaussiennes. Pour tous les calculs, la fonctionnelle hybride globale PBE0 a été utilisée avec une correction D3 pour les interactions de dispersion.

Chapitre 3 : Interface MAPI/TiO_2

Une stratégie possible pour améliorer les performances de la PSC est l'utilisation d'un ligand bifonctionnel permettant de relier efficacement la pérovskite MAPI et TiO_2. Quatre ligands ont ici été considérés: 4- chlorobenzoate (CBA); 4- nitrobenzoate (NBA); 4-méthoxybenzoate (MBA) et la β-alanine (β-ALA) . Leur adsorption sur la surface (101) de TiO_2 anatase a été étudiée.

Expérimentalement, il est facile de synthétiser des nanoparticules de pérovskite. En outre, l'anatase a une surface (101) qui est stable et qui peut être exposée lorsqu'un film de pérovskite est fabriqué. Cette surface présente des atomes sous-coordonnés, en particulier des atomes de Ti pentacoordonnés et des atomes d'O bicoordonnées qui constituent des sites d'adsorption pour les ligands.

La **Figure 3** présente la structure optimisée des molécules de CBA adsorbées sur la surface de l'anatase (101) suivant un mode d'adsorption dissociatif de type bidentate. Sans l'introduction du solvant méthanol dans le modèle, on peut constater que CBA a tendance à se coucher sur la surface. Cela est dû à l'interaction qui se produit entre le cycle benzoïque et les protons de surface obtenus après dissociation du groupement acide carboxylique. Puisque les données expérimentales disponibles ont été obtenues en solvant, nous avons également ajouté une molécule de méthanol par maille au modèle. L'interaction entre le méthanol et la surface de l'anatase est réalisée par la liaison H. L'angle d'inclinaison de CBA sans solvant est de 42 degrés, alors qu'il est réduit à 30 degrés lorsqu'une molécule de solvant est ajoutée au modèle.

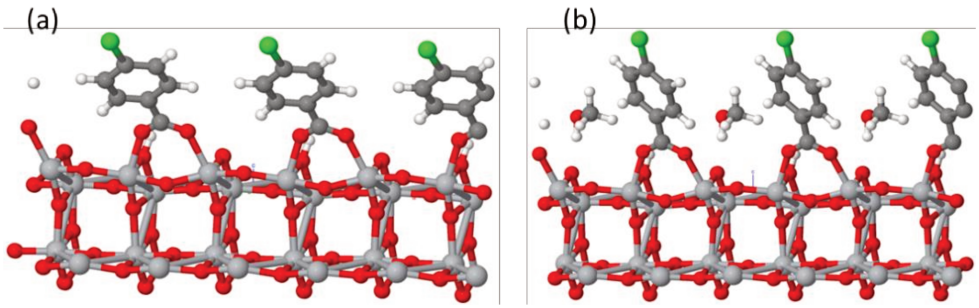

Figure 3 : Structure optimisée de CBA adsorbée sur une surface d'anatase TiO_2(101) sans (a) et avec (b) méthanol. Les atomes de carbone, de titane, d'oxygène, de chlore et d'azote sont représentés respectivement par des boules grises, argentées, blanches, rouges, vertes et bleues.

La **Figure 4** présente les structures obtenues pour les quatre ligands adsorbés sur la surface de TiO_2, avec du méthanol comme solvant. Tous les ligands sont liés à la surface par le groupe carboxylique dissocié, avec le même mode d'adsorption. Les énergies d'adsorption calculées sont respectivement de -20.73, -11.33, -30.62 et -20.20 kcal/mol pour CBA, NBA, MBA et β-ALA. Les valeurs obtenues démontrent que tous les ligands peuvent être fortement chimisorbés sur la surface de TiO_2.

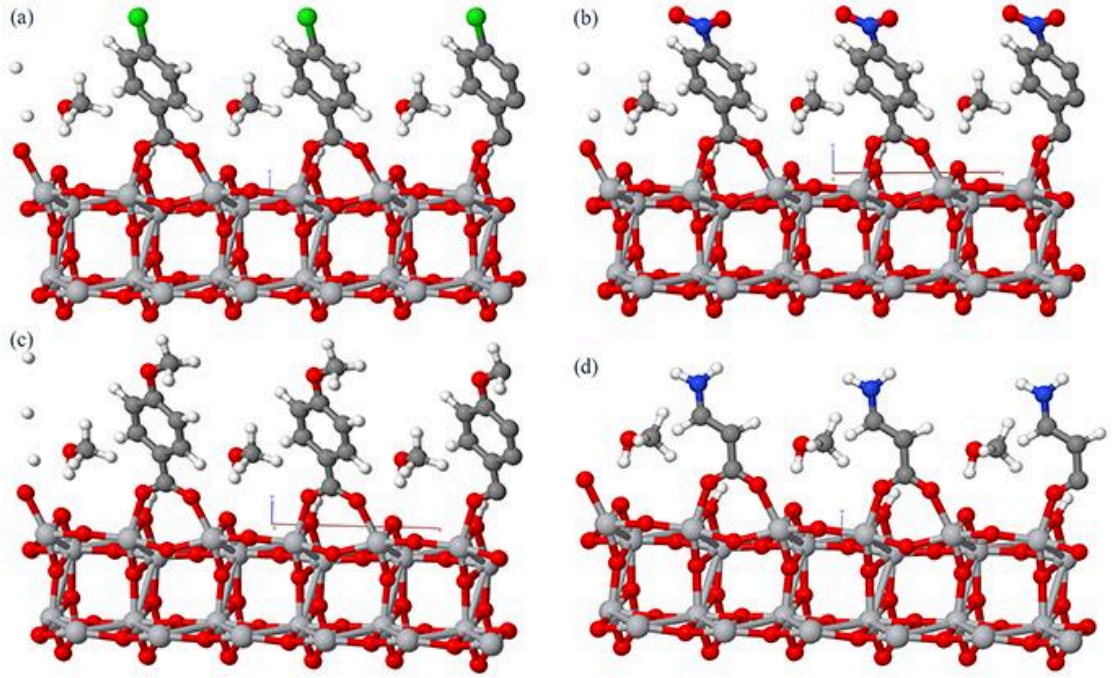

Figure 4 : Structure optimisée des 4 acides adsorbés sur la surface d'anatase (101). Les atomes de carbone, de titane, d'oxygène, de chlore et d'azote sont représentés respectivement par des boules grises, argentées, blanches, rouges, vertes et bleues. (a) CBA, (b) NBA, (c) MBA et (d) β-ALA.

Le modèle d'adsorption obtenu a été confirmé par analyse des fréquences de vibration des ligands adsorbés sur TiO_2, qui ont été obtenues à la fois expérimentalement et théoriquement. Le bon accord obtenu entre données expérimentales et théoriques confirme le mode d'adsorption obtenu.

Le ligand peut aussi induire un moment dipolaire de surface aux systèmes étudiés. L'effet du moment dipolaire de surface sur le transfert de charge est explicité en **Figure 5**. La composante du moment dipolaire suivant la normale à la surface est de 2.22, 0.89, 0.12 et -0.50 Debye pour NBA, CBA, β-ALA et MBA, respectivement. La valeur obtenue pour β-ALA semble douteuse, en raison des mesures expérimentales de la fonction de travail qui ne suit pas la tendance des trois autres ligands. Néanmoins, pour les ligands présentant un moment dipolaire positif, cela conduirait à l'augmentation de la valeur absolue de la fonction de travail, alors que pour ceux présentant un moment dipolaire négatif, cela conduirait à l'effet opposé. Ainsi, un moment dipolaire positif introduirait un champ électrique avec un centre positif situé au niveau du dispositif, ce qui favoriserait le transfert d'électrons; au contraire, un moment dipolaire négatif introduirait un champ électrique avec un centre négatif localisé au niveau du dispositif, ce qui réduirait le transfert d'électrons. Ainsi, il serait donc préférable de considérer des ligands ayant un moment dipolaire de surface positif après adsorption, indiquant ainsi que CBA et NBA sont a priori de bons candidats pour jouer le rôle de ligand pour application PSC.

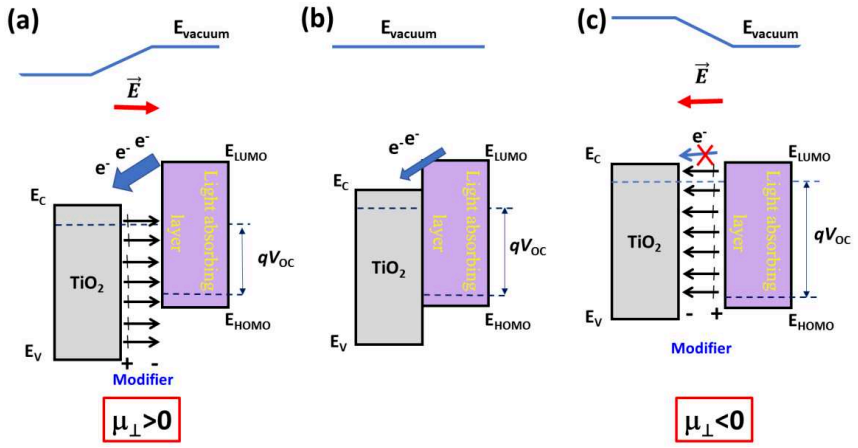

Figure 5 : Effet des dipôles interfaciaux sur l'énergétique de l'hétérojonction TiO_2/ couche absorbant la lumière. (a) Dipôle conduisant à $\mu_\perp > 0$ à l'interface; (b) une interface vierge et (c) un dipôle conduisant à $\mu_\perp < 0$ à l'interface .

Dans ce chapitre, nous avons étudié l'adsorption de CBA, NBA, MBA et β-Alanine sur la surface TiO_2 anatase (101), en comparant les données expérimentales disponibles aux données calculées. Un bon accord général entre expérience et théorie a pu être mis en évidence. A partir du calcul des énergies de surface, on constate que tous les ligands peuvent être chimisorbés. Le mode d'adsorption bidenté pontant est confirmé par l'analyse des fréquences de vibrations et des modes normaux correspondants. Les propriétés électroniques indiquent que les ligands améliorent l'alignement des bandes. De plus, nous pouvons conclure que le solvant n'a aucun effet sur la bande interdite des systèmes étudiés. L'étude des moments dipolaires de surfaces nous a permis de conclure que CBA et NBA sont de potentiels bons candidats pour améliorer les dispositif PSC.

Chapitre 4: Interface MAPI/Ligand/TiO_2

Comme démontré précédemment, le ligand s'adsorbe de manière stable sur la surface de l'anatase et son adsorption améliore l'alignement des bandes et induit un moment dipolaire qui peut encore améliorer le transfert de charge. Ici, nous nous concentrerons sur le ligand CBA pour simuler l'interface complète entre la pérovskite et la couche de transport d'électrons. Bien que l'étude de l'interface complète MAPI/CBA/TiO2 soit très coûteuse en temps machine car la cellule unitaire de cette interface est très grande, ce travail peut aider à mieux comprendre le mécanisme de fonctionnement des PSC, en particulier d'un point de vue électronique.

Pour simuler cette interface, la première chose que nous avons fait est de construire un modèle raisonnable de cette interface. La construction de ce modèle s'est faite en plusieurs étapes. Tout d'abord, une supercellule de la surface (101) de l'anatase a été construite. Dans le même temps, la surface de MAPI (110) avec terminaison MAI a été sélectionnée, car il est plus facile de former une interface avec TiO_2 avec cette dernière qu'avec une terminaison de type PbI_2. Le ligand CBA a été adsorbé sur la surface de TiO_2 et connecté à MAPI en éliminant des Cl afin d'assurer la neutralité de la maille de l'interface. Afin de faire correspondre les deux mailles, les paramètres de maille de la partie MAPI ont été ajustés à ceux de TiO_2. Lors de l'optimisation de la géométrie, seule la partie inférieure de l'interface ainsi considérée a été figée, tous les autres atomes étant autorisés à relaxer. La **Figure 6** montre le modèle obtenu après relaxation. Le **Tableau 1** répertorie les principales caractéristiques structurelles et énergétiques du système obtenu.

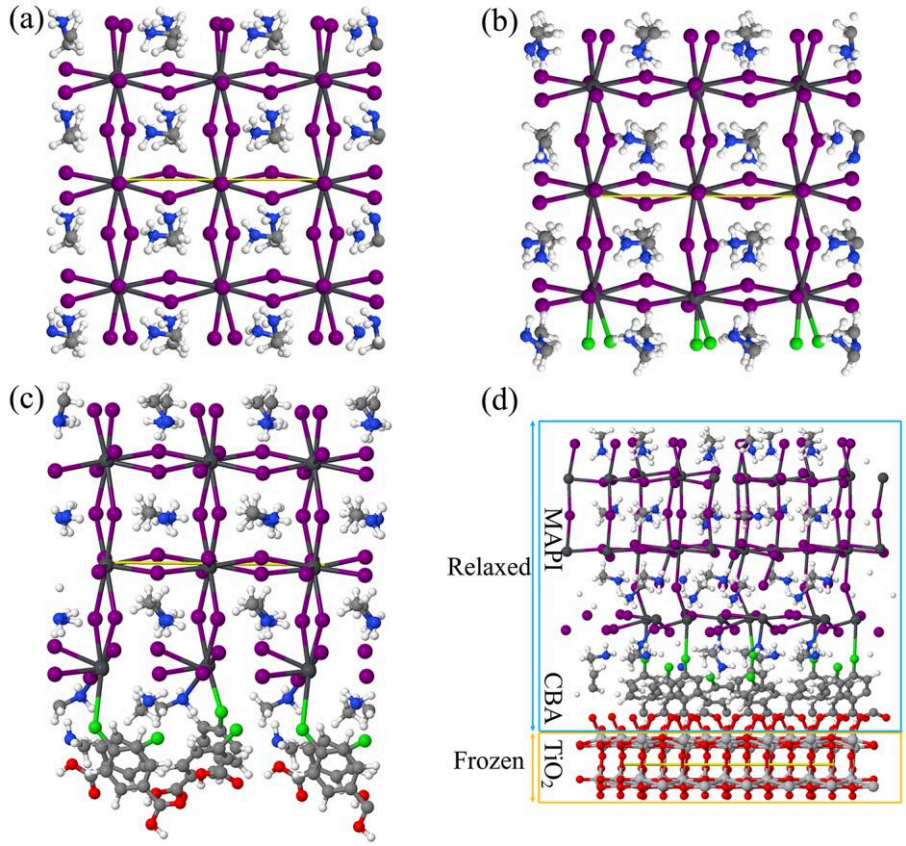

Figure 6 : Représentations de (a) la surface MAPI (110), (b) la surface de MAPI où tous les atomes d'iodure d'une surface ont été remplacés par des atomes de chlore, (c) interface MAPI/CBA et (d) interface MAPI/CBA/TiO_2. La ligne jaune continue représente la cellule unitaire. Les sphères rouges, gris clair, blanches, vertes, violettes, gris foncé, bleues et grises correspondent respectivement aux atomes O, Ti, H, Cl, I, Pb, N et C. Les parties relaxées et figées considérées pour l'optimisation de la géométrie de l'interface MAPI/CBA/TiO_2 sont indiquées sur la Figure 6 (d).

Tableau 1 : Paramètres de maille a, b (en Å) et γ (en degrés), ainsi que largeurs de bande calculées (E_g, en eV) pour les systèmes sélectionnés impliqués dans la construction du modèle d'interface. L'énergie d'adhésion (E_{adh}, en eV) et l'énergie d'adhésion spécifique (β, en eV·Å^{-2}) de l'interface MAPI/CBA/TiO_2 sont également données.

	MAPI (110)	CBA/MAPI (110)	TiO_2 (101)	MAPI(110)/CBA/TiO_2 (101)
a	12.343	12.343	14.981	14.821
b	12.555	12.555	11.088	11.003
γ	90.00	90.00	109.74	108.03
E_g	2.97	3.39	5.03	2.16
E_{adh}	--	--	--	3.45
β	--	--	--	0.02

Les paramètres optimisés du modèle d'interface complète sont proches de ceux de la supercellule TiO_2 considérée, mais avec une légère compression. L'énergie positive d'adhésion calculée pour l'interface complète confirme la stabilité du système.

Le tableau 2 rapporte les moments dipolaires calculés. Pour TiO_2/CBA et pour l'interface complète, leurs valeurs sont positives. Cependant, pour le système MAPI/CBA, il est négatif. Ainsi, on peut conclure que CBA peut bloquer le transfert d'électrons vers MAPI dans le système MAPI/CBA, tandis que CBA peut potentiellement améliorer le transfert d'électrons de MAPI vers TiO_2 dans le système MAPI/CBA/TiO_2.

Tableau 2 : Composantes normales des moments dipolaires (μ_z, dans Debye) pour CBA/TiO_2, MAPI/CBA et MAPI/CBA/ TiO_2.

Systèmes	μ_z
CBA/TiO_2	0.89
M API/CBA	-0.88
MAPI/CBA/TiO_2	0.61

Afin de clarifier le transfert d'électrons de MAPI à TiO_2, nous avons analysé la densité de spin du système complet réduit, comme le montre la **Figure 7**. Un taux d'injection de 99.94% est obtenu. Cette valeur étant une estimation de l'efficacité d'injection des électrons

photogénérés, elle indique donc un transfert d'électrons presque quantitatif de MAPI à TiO_2 à travers le ligand CBA. Enfin, le temps d'injection d'électrons calculé est estimé à 24 fs, indiquant une injection d'électrons ultra-rapide dans le domaine de la femtoseconde.

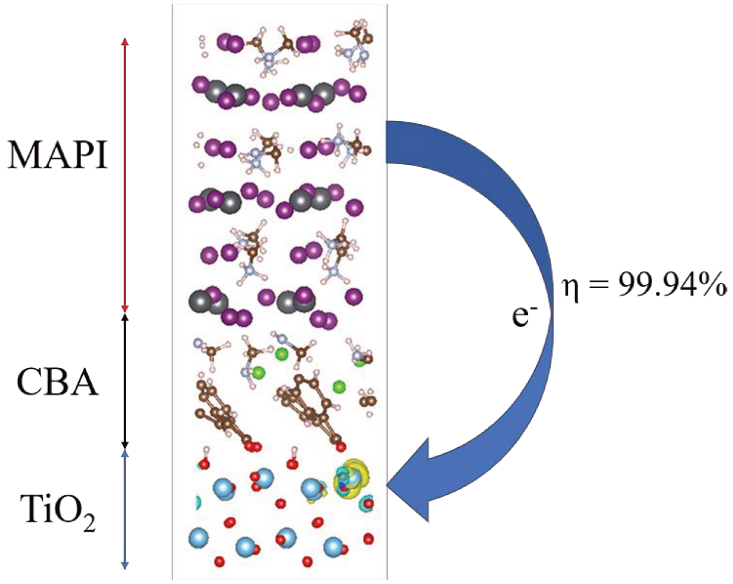

Figure 7 : Densité de spin du système MAPI/CBA/TiO_2 réduit (l'excès d'électrons alpha est indiqué en jaune), valeur du contour isosurface : |0,00271| au.

Dans ce chapitre, un modèle d'interface MAPI/CBA/TiO_2 a été construit et étudié. Nos données de calcul sont en accord avec les données expérimentales disponibles. D'après les résultats structurels, une interface stable a été trouvée en raison de la liaison favorable de CBA avec MAPI et TiO_2. Du point de vue des propriétés électroniques, l'injection d'électrons du MAPI au TiO_2 semble favorable. Nos recherches montrent ainsi que l'optimisation du ligand peut être envisagée et devrait conduire à un meilleur alignement des bandes et à une meilleure injection d'électrons dans de tels systèmes. En outre, bien que MAPI soit considéré comme la pérovskite la plus efficace utilisée pour applications PSC, il reste soumis à des inconvénients majeurs, tels que sa facilité à se décomposer en milieu humide ou encore une mauvaise absorption dans le proche infrarouge. Afin de résoudre ces problèmes, des pérovskites alternatives à MAPI telles que FAPI peuvent être envisagées.

Chapitre 5: FAPI

Comme déjà mentionné, la pérovskite pour application PSC est composée d'ions A, B et X. Utiliser le formamidinium pour occuper le site A est considéré comme un plan alternatif idéal. Il s'agit en effet d'une molécule de haute symétrie, et son utilisation en tant que cation dans ces pérovskites a conduit à des rendements de photoconversion élevés. Le FAPI synthétisé

a généralement deux types de structures. Le α-FAPI est noir et il a une bande interdite directe d'environ 1.45 eV, ce qui est très approprié pour les applications PV. Cependant, à température ambiante, il se transforme facilement en δ-FAPI, le FAPI jaune, qui a une bande interdite indirecte d'environ 2.5 eV. Cette structure hexagonale ne peut pas être utilisée en PV. En raison de cette transition rapide, dans les expériences, le FA est toujours incorporé avec d'autres cations. Cependant, du point de vue théorique, nous pouvons étudier l'α-FAPI afin de comprendre ses propriétés et sa faible stabilité. Dans ce chapitre, nous avons étudié l'α-FAPI en bulk ainsi que deux de ses surfaces de faibles indices. Cette étude préliminaire nous a aidé à comprendre les propriétés globales du système FAPI, en lien avec les données expérimentales disponibles en littérature. La grande stabilité des différents modèles de surface considérés indique que des modèles d'interface complexes pourraient être construits avec TiO_2, à comparer avec le cas MAPI/CBA/TiO_2 présenté dans le chapitre précédent.

Conclusions finales

En résumé, le travail de modélisation DFT effectué s'est globalement divisé en trois grandes parties. La première concerne l'adsorption de ligands sur la surface de TiO_2 anatase (101). La seconde concerne la simulation de modèles d'interface de pérovskite/Ligand/TiO_2. Enfin, la dernière partie s'est focalisée sur une étude préliminaire des propriétés du bulk et de surface des composés de pérovskite.

À partir de nos résultats, nous avons pu mettre en évidence que la DFT s'est avérée être une méthode appropriée pour étudier des interfaces complexes, les caractéristiques structurales et électroniques étant en bon accord avec les données expérimentales disponibles pour les différents systèmes envisagés.

Notre recherche a pu en particulier mettre en évidence l'importance du couplage entre pérovskite et TiO_2 et le rôle d'un ligand bifonctionnel dans l'amélioration des performances et de la stabilité des interfaces que l'on trouve dans les dispositifs pour application PSC.

RÉSUMÉ

Dans cette thèse, nous avons cherché à contribuer à une meilleure compréhension des surfaces et des interfaces impliquant des composés pérovskites et à la gouvernance des performances des PSC, en utilisant des protocoles de calcul basés sur la théorie fonctionnelle de la densité (DFT), avec une comparaison avec des données expérimentales, lorsque disponibles. Nous avons principalement considéré trois types de modèles: TiO_2 avec adsorption de ligands, interface complète pérovskites/ligand/TiO_2 et α-CH $(NH_2)_2PbI_3$ (α-FAPI) en vrac ainsi que ses surfaces. La relation entre la structure et les propriétés de la pérovskite pourrait être établie sur la base de la modélisation effectuée. L'approche proposée ici pourrait être étendue à d'autres hétérostructures semi-conductrices dans une grande variété d'applications optoélectroniques, où elle pourrait contribuer à une meilleure compréhension des principes de fonctionnement de ces dispositifs pour améliorer leurs performances.

MOTS CLÉS

DFT, Pérovskites, TiO_2, surface, interface

ABSTRACT

In this thesis, we aimed to contribute to a better understanding of the surfaces and interfaces involving perovskite compounds and governing the performances of PSCs, by using density-functional theory (DFT)-based computational protocols, with a comparison with experimental data, when available. We mainly considered three kinds of models: TiO_2 with ligands adsorption, perovskites/ligand/TiO_2 full interface, and α-$CH(NH_2)_2PbI_3$ (α-FAPI) bulk as well as its surfaces. The relationship between structure and perovskite properties could be established based on the modeling carried out. The approach proposed here could be extended to other semiconductor heterostructures in a wide variety of optoelectronic applications, where it could contribute to a better understanding of the working principles of these devices to improve their performances.

KEYWORDS

DFT, Perovskites, TiO_2, Surface, Interface